Technische Universität München
TUM School of Engineering and Design

Adjoint-Based Analysis of Low-Order Thermoacoustic Networks

Felicitas Engelhardt

Vollständiger Abdruck der von der TUM School of Engineering and Design der Technischen Universität München zur Erlangung des akademischen Grades einer

Doktorin der Ingenieurwissenschaften

genehmigten Dissertation.

Vorsitz:
Prof. Dr.-Ing. Hans-Jakob Kaltenbach
Prüfer*innen der Dissertation:
1. Prof. Wolfgang Polifke, Ph.D.
2. Prof. Dr.-Ing. Jonas Moeck

Die Dissertation wurde am 14.06.2023 bei der Technischen Universität München eingereicht und durch die TUM School of Engineering and Design am 20.09.2023 angenommen.

To my family.

Abstract

This thesis aims to improve the understanding of thermoacoustic system behavior by employing and extending network model analysis. The proposed methods and implementation approaches enable (i) the introduction of an elaborate model for longitudinal wave propagation, (ii) the determination of the adjoint system for a given network model, and (iii) the identification of exceptional points, with minimum resources.

A wave-based numerical solution for a duct with varying cross-section and mean temperature distribution is presented. With this approach, existing network libraries can be extended with minor implementation effort, enabling more accurate modeling of thermoacoustic combustors as both complex geometries and heat loss effects along the combustor can be taken into account.

Furthermore, the thesis introduces a novel approach to calculate the adjoint of a thermoacoustic network model. This "Hybrid Adjoint" (HA) approach is based on the continuous adjoint (CA) equations but is applied to the discretized system, similar to the discrete adjoint (DA) approach. As such, hybrid adjoints combine the advantages and eliminate some of the disadvantages of the CA and DA approaches: While it requires minimum implementation effort and applies to any system that can be built using the original network model framework, it is also capable of accurately displaying the adjoint eigenmodes regardless of the discretization of the direct equations. In an exemplary study, the HA approach is successfully applied to an annular combustor to find the optimal parameters of two Helmholtz resonators.

An alternative, DA based approach to combine adjoint design with network model tools is introduced and used to identify exceptional points in thermoacoustic systems. The identification algorithm is based on an adjoint-enhanced optimization routine, which determines the parameters of an eigenvalue problem for a given eigenvalue. By exploiting the topology of the state-space network model, adjoint eigenvalue sensitivities may be calculated based on modifications to the system matrix, thus eliminating the need to rebuild the network model after changing the model parameters. With the proposed algorithm, the existence of an unstable exceptional point for a physical parameter setting and a realistic flame model could be demonstrated for the first time in the context of thermoacoustic combustion instabilities. Subsequent studies examine the exceptional points in more detail. Among others, they are found to significantly impair the quality of surrogate models and the reliability of stability predictions.

Kurzfassung

Diese Arbeit zielt darauf ab, das Verständnis thermoakustischen Systemverhaltens durch die Erweiterung und Anwendung von Netzmodellanalyse zu verbessern. Die hier beschriebenen Methoden und Implementierungsansätze ermöglichen (i) die Einführung eines erweiterten Modells für die Ausbreitung longitudinaler akkustischer Wellen, (ii) die Bestimmung des adjungierten Systems für ein gegebenes Netzwerkmodell und (iii) die Identifizierung von "Exceptional Points" mittels minimaler Ressourcen.

Für die Einführung des erweiterten Rohrleitung-Elements wird eine wellenbasierte numerische Lösung vorgestellt, die Änderungen in Rohrquerschnitt und mittlerer Temperaturverteilung berücksichtigt. Mit dem Ansatz können bestehende Netzwerkbibliotheken mit geringem Implementierungsaufwand erweitert werden. Das Element ermöglicht eine genauere Modellierung von thermoakustischen Brennkammern, da sowohl komplexe Geometrien als auch Wärmeverlusteffekte entlang der Brennkammer dargestellt werden können.

Darüber hinaus stellt die Dissertation einen neuartigen Ansatz zur Berechnung der Adjungierten eines thermoakustischen Netzwerkmodells vorgestellt. Der so genannte Hybride Adjungierte Ansatz (HA) basiert auf den kontinuierlichen adjungierten Gleichungen (CA), wird aber auf Basis des diskretisierten Systems berechnet, ähnlich wie der diskrete adjungierte Ansatz (DA). Die hybride Adjunktion vereint somit viele der Vorteile und eliminiert einige Nachteile der CA- bzw. DA-Ansätze: Die Methode erfordert einen minimalen Implementierungsaufwand und ist auf jedes System anwendbar ist, das mit dem ursprünglichen Netzwerkmodell dargestellt werden kann. Darüber hinaus werden die adjungierten Eigenmoden unabhängig von der Diskretisierung der direkten Gleichungen korrekt dargestellt. In einer beispielhaften Studie wird der HA-Ansatz erfolgreich auf eine ringförmige Brennkammer angewandt, um die optimalen Parameter für zwei Helmholtz-Resonatoren zu finden.

Eine alternative, vom DA Ansatz abgeleitete Mehtode zur Kombination von adjungiertem Design mit Netzwerkmodellen wird zur Identifizierung von *Defekten Eigenwerten* in thermoakustischen Systemen vorgestellt und angewendet. Der Algorithmus basiert auf einer adjungierten Optimierungsroutine, die die Parameter eines thermoakustischen Modells bestimmt, für die ein vordefinierter Eigenwert resultiert. Durch die Ausnutzung der Topologie des Zustandsraum-Netzwerkmodells können adjungierte Eigenwert-Sensitivitäten aus der modifizierten Systemmatrix berechnet werden, wodurch die Notwendigkeit entfällt, das Netzwerkmodell nach einer Änderung der Modellparameter neu aufzubauen. Mit dem beschriebenen Algorithmus konnte erstmals die Existenz eines instabilen Exceptional Points in einem thermoakustischen System mit realistischem Flammenmodell nachgewiesen werden, dessen Parametereinstellung physikalisch realisierbar sind.

Darauf aufbauende Studien widmen sich der näheren Analyse von Exceptional Points. Unter anderem ergeben diese, dass die Qualität von Ersatzmodellen und die Zuverlässigkeit von Stabilitätsvorhersagen erheblich durch die Präsenz von Exceptional Points beeinträchtigt wird.

Contents

1 Introduction

The energy sector accounts for approximately 33 percent of the total German carbon dioxide emissions [30]. In times where the repercussions of climate change have not only been predicted for years, but have already manifested themselves in local droughts, wildfires, and floods, the need for a quick transition to renewable energies becomes more and more urgent. However, this transition is, among others, associated with one major challenge: The energy grid has to account for strong fluctuations in the supply of renewable energy, as wind or solar power plants are subject to local weather conditions. To counterbalance these fluctuations, gas turbines offer the best compromise of operational flexibility and ecological compatibility. They enable fast start-ups and shut-downs, and on-demand load changes, thus offering a quick response to the unsteady power supply. At the same time, thanks to lean-premixed combustion technology, gas turbines nowadays emit low levels of pollutants while being highly efficient. However, engines operating under lean-premixed conditions become more susceptible to thermoacoustic combustion instabilities.

Thermoacoustic instabilities result from a constructive coupling of pressure and heat release fluctuations at the flame. They manifest themselves in amplified pressure oscillations, which impair engine performance and emissions, decrease its lifetime or even cause structural damage [66]. Late-stage adaptions in engine design to eliminate unexpected instabilities are prohibitively expensive: Adaptions made to achieve linear stability over the entire operating regime may involve extensive testing, curtailments in flexibility by avoiding specific operating conditions, or the retrofitting of passive dampers such as Helmholtz resonators. It is, therefore, paramount to predict and eliminate thermoacoustic instabilities during the early phases of the engine design process.

There exist a range of modeling techniques for the prediction of unstable operating points, which differ in their degree of abstraction. On the lower end, there are high-fidelity simulations that depend on few assumptions and deliver the most accurate results. However, they are associated with increased computational cost and more elaborate model design processes, *e.g.* geometry and mesh generation. The highest level of abstraction is employed by so-called low-order models. These are highly flexible and cost-efficient but commonly consider the propagation of acoustic waves along only one dimension, usually the axial or azimuthal direction.

Nevertheless, low-order models constitute a good trade-off between cost and prediction accuracy in early-stage engine design. In particular, low-order network models have proven to be a valuable instrument for primary engine analyses. Moreover, they have been successfully applied to gain a fundamental understanding of the underlying physics that govern thermoacoustic systems.
Thanks to their modular architecture, even complex geometry models can be built in a matter of minutes, *e.g.* to assess the stability behavior for different parameter configurations.
Network tools calculate the system eigenvalues, which are composed of the eigenfrequency and

associated growth rate. Physically, a positive growth rate signifies that oscillations at the corresponding frequency grow over time, rendering the system linearly unstable. Having identified an unstable mode, the system parameters need to be adapted in order to stabilize the system.

However, thermoacoustic systems are highly sensitive to a large number of parameters, whose effect may change for different eigenvalues and parameter configurations. Consequently, adjusting a parameter to stabilize one eigenvalue may, for instance, have a destabilizing effect on a different eigenvalue. Therefore, finding a stable parameter setting via trial-and-error is both time-consuming and expensive in terms of computational cost [39, 49].

In addition, the high eigenvalue sensitivity may cause an originally stable eigenvalue to become unstable for minor variations of the system parameters. This is particularly problematic, as parameters are always subject to uncertainties. More specifically, stochastic fluctuations causing the operating conditions to deviate from the nominal condition may result in instability even though the nominal system was predicted to be stable. The propagation of uncertainties must, therefore, be included in the process of stability analysis.

Parameter sensitivities and the associated arising challenges may be enhanced by the presence of so-called exceptional points (XPs). XPs are marked by the coalescence of multiple eigenvalues and their associated eigenfunctions. At the XP, the eigenvalue is infinitely sensitive to parameter changes [33]. This leads to particular system behaviors in the vicinity of the XP, including strong veering of the eigenvalue trajectories [64]. Along these trajectories, the effect of individual parameters on the stability of the eigenvalue may be subject to sudden changes: A parameter that originally stabilizes the eigenvalue, may ultimately have a de-stabilizing effect. On the one hand, this poses an additional challenge for the control of thermoacoustic instability and needs to be taken into account accordingly. On the other hand, provided that the parameter setting at the XP is known, the unusual physical behavior may even be exploited to stabilize the system.

When dealing with increased eigenvalue sensitivity and a large number of system parameters, adjoint design offers a valuable solution to accelerate system analysis. Instead of finding the effect a parameter has on the eigenvalue by applying a small change to it and subsequently rerunning the calculation, adjoint design delivers eigenvalue sensitivities w.r.t. all parameters in just one calculation [49, 51]. The runtime needed to calculate the adjoint sensitivity is comparable to the original system runtime. In contrast, approximating the sensitivity with a finite difference approach would require at least one additional computation for each system parameter. Thus, for the calculation of the adjoint eigenvalue sensitivity w.r.t. N parameters, the number of computational runs reduces by $N-1$. Through these benefits, adjoint analysis has proven to be highly efficient and accurate for the analysis and optimization of thermoacoustic systems.

The application of adjoint methods in thermoacoustics ranges from classical sensitivity analysis, over efficient optimization routines, to the quantification of prediction uncertainties. There are two ways of calculating the adjoint sensitivities. The first, called the continuous adjoint (CA), is based on a set of adjoint equations, which need to be derived analytically from the direct system. The resulting model is subsequently discretized and solved, equivalently to the original, direct system. In order to implement the CA approach in an existing network framework the respective adjoint equations need to be derived for each element or system which involves the implementation of a completely new set of adjoint elements. The so-called discrete adjoint (DA), on the other hand, is derived from the discretized form of the direct system. For this

second approach, calculating the adjoint system merely requires the evaluation of the complex conjugate system matrix, and does not involve any elaborate derivations. As such, the DA is easier to implement and less error-prone than the CA. However, the analysis of the DA system may be aggravated as the resulting adjoint eigenmodes often exhibit spurious oscillations at the boundary and jump conditions [38]. The adjoint system obtained via the CA approach does not suffer from this shortcoming. In addition, the system analysis via the CA approach offers physical insight into the original system, since adjoint equations can be interpreted directly.

This publication-based thesis proposes new methods of extending thermoacoustic network models for efficient stability analysis. In a first study, a new element is added to the network library, which incorporates temperature and geometry variations along a duct element. Based on a second extension of the same network tool, the thesis introduces a third way to perform adjoint analysis using thermoacoustic network models: hybrid adjoints (HA). This novel approach combines the advantages of the CA and DA. More specifically, the HA is straightforward to implement and does not require the derivation of the adjoint equations for each model element. At the same time, the HA does not exhibit the spurious oscillations observed for the DA, thus allowing for direct interpretation of the adjoint eigenmodes.

An alternative way of performing adjoint analysis is proposed in a study that aims to identify and analyze exceptional points. The proposed algorithm to locate XPs reveals for the first time the existence of physically viable, unstable XPs in the thermoacoustic spectrum. In subsequent studies, XPs are identified as a source of unreliable model predictions and surrogate model failure.

2 Thermoacoustic Network Modeling

The simulation of thermoacoustic models using standard tools of computational fluid dynamics (CFD) may get excessively expensive. On the one hand, acoustic waves extend over a large domain in space and propagate with high velocities, which requires a high resolution in time over a large domain. On the other hand, diffusive species and heat transport processes at the flame happen on the smallest spatial dimensions, thus setting high demands on the mesh.

To reduce the computational cost, many models exploit the linear nature of the system acoustics by applying a *divide et impera* approach. Here, the unsteady heat release at the flame is modeled separately from the acoustics. The flame response to acoustic perturbations is then included via a flame transfer function (FTF) for linear analysis, or a flame describing function (FDF) for non-linear analysis.

In network models, the acoustics are additionally divided into various homogeneous "elements". For each of these elements, the acoustic problem is reduced to a minimum and can be solved analytically [20, 81].
Building the aggregated thermoacoustic model merely requires the interconnection of the corresponding elements, making low-order network models a powerful tool for the efficient simulation of thermoacoustic systems. The resulting model constitutes a series of "duct elements" that are connected by a set of elements modeling geometrical and physical jump conditions with reflection coefficients at the upstream and downstream end of the system, respectively [16, 21, 36].

In this chapter, the basic concepts of thermoacoustic networks are explained. In particular, the open-source tool *taX* is introduced, which was developed at TU Munich and is used throughout the thesis.

2.1 The Acoustic Wave Equations

Low-order network models apply eigenvalue analysis to determine whether a system is linearly stable or not. The equations of each element follow from the one-dimensional continuity, momentum, and energy equations for a perfect, inviscid gas:

$$\frac{\partial \rho}{\partial t} + \frac{\partial \rho u}{\partial x} = 0, \tag{2.1a}$$

$$\rho \frac{\partial u}{\partial t} + \rho u \frac{\partial u}{\partial x} + \frac{\partial p}{\partial x} = 0, \tag{2.1b}$$

$$\frac{\partial s}{\partial t} + u \frac{\partial s}{\partial x} = \frac{R_g \dot{q}}{p}, \tag{2.1c}$$

where ρ is the density, u the axial velocity, p the pressure, T the temperature, s the entropy, $\dot{q}$ the heat flux, R_g the universal gas constant, t the time and x the axial coordinate.

All properties of the flow are assumed to be constant over the element cross-section. In order to linearize the system, the flow is decomposed into a steady, time-averaged part (denoted $\bar{}$) and a small perturbation part (denoted $'$). The linearized conservation equations are given by:

$$\frac{\partial \rho'}{\partial t} + \bar{u}\frac{\partial \rho'}{\partial x} + u'\frac{\partial \bar{\rho}}{\partial x} + \bar{\rho}\frac{\partial u'}{\partial x} + \rho'\frac{\partial \bar{u}}{\partial x} = 0, \tag{2.2a}$$

$$\bar{\rho}\frac{\partial u'}{\partial t} + \rho'\bar{u}\frac{\partial \bar{u}}{\partial x} + \bar{\rho}u'\frac{\partial \bar{u}}{\partial x} + \bar{\rho}\bar{u}\frac{\partial u'}{\partial x} + \frac{\partial p'}{\partial x} = 0, \tag{2.2b}$$

$$\frac{\partial s'}{\partial t} + \bar{u}\frac{\partial s'}{\partial x} = -\frac{\bar{\dot{q}}R_g}{\bar{p}}\left(\frac{u'}{\bar{u}} + \frac{p'}{\bar{p}}\right). \tag{2.2c}$$

Following the approach laid out in Ref. [43] Eqs. (2.2) can be transformed into three coupled differential equations in u', p', and s'.

Commonly, the "duct" element is the only element with a significant axial extent while all other elements are considered acoustically compact, *i.e.* the axial length of the element is small in comparison to the acoustic wave length, resulting in a small Helmholtz number $He = l_e/\lambda << 1$. A compact element can be interpreted as a set of jump conditions from the previous element to the next. By contrast, the acoustic waves propagate within the duct element, making the duct a central element of every thermoacoustic model. At the same time, both the duct and the flame element introduce a non-linearity to the eigenvalue problem. Consequently, their mathematical description in thermoacoustic networks merits detailed analysis, which will be laid out hereafter.

For the straight duct with a constant cross-sectional area and homogeneous mean flow quantities along the longitudinal axis, the system of equations Eqs. (2.2) reduces to:

$$\frac{\partial p'}{\partial t} + \bar{u}\frac{\partial p'}{\partial x} + \gamma\bar{p}\frac{\partial u'}{\partial x} = 0, \tag{2.3a}$$

$$\bar{\rho}\frac{\partial u'}{\partial t} + \bar{\rho}\bar{u}\frac{\partial u'}{\partial x} + \frac{\partial p'}{\partial x} = 0, \tag{2.3b}$$

$$\frac{\partial \sigma'}{\partial t} + \bar{u}\frac{\partial \sigma'}{\partial x} = 0, \tag{2.3c}$$

where $\varsigma' = \sigma'/c_p$ and c_p is the heat capacity at constant pressure. The equations can be decoupled by introducing the characteristic wave amplitudes f, g, and ς:

$$\frac{\partial}{\partial t}\begin{bmatrix} f \\ g \\ \varsigma \end{bmatrix} = \begin{bmatrix} -(\bar{c}+\bar{u}) & 0 & 0 \\ 0 & (\bar{c}-\bar{u}) & 0 \\ 0 & 0 & -\bar{u} \end{bmatrix} \frac{\partial}{\partial x}\begin{bmatrix} f \\ g \\ \varsigma \end{bmatrix}. \tag{2.4}$$

Equation (2.4) describes two plane waves f and g propagating in down- and upstream direction with the velocities $(\bar{c}+\bar{u})$ and $(\bar{c}-\bar{u})$, respectively. In addition, an entropy wave ς propagates downstream with mean flow velocity $\bar{u}$. Consequently, the causality of the system is implicitly given by the traveling direction of the incident waves f_u, g_d, and ς_u, which leave the duct with a time delay corresponding to the duct length and the respective propagating velocity.

Compact elements representing a discontinuity, such as "area" or "temperature jumps", are fully described via their respective scattering matrix, which relates the upstream and downstream characteristic wave amplitudes to each other:

$$\begin{bmatrix} g_u \\ f_d \\ \varsigma_d \end{bmatrix} = \begin{bmatrix} S_{11} & S_{12} & S_{13} \\ S_{21} & S_{22} & S_{23} \\ S_{31} & S_{32} & S_{33} \end{bmatrix} \begin{bmatrix} f_u \\ g_d \\ \varsigma_u \end{bmatrix}. \tag{2.5}$$

Transforming the duct equations (Eq. (2.4)) into the Laplace domain leads to an equivalent representation of the duct element:

$$\begin{bmatrix} g_u \\ f_d \\ \varsigma_d \end{bmatrix} = \underbrace{\begin{bmatrix} 0 & e^{-s\tau_g} & 0 \\ e^{-s\tau_f} & 0 & 0 \\ 0 & 0 & e^{-s\tau_\varsigma} \end{bmatrix}}_{S} \begin{bmatrix} f_u \\ g_d \\ \varsigma_u \end{bmatrix}. \tag{2.6}$$

However, looking at the entries of the scattering matrix, it becomes clear that the presence of a time delay leads to a non-linear terms in s in the system of equations.

A similar issue can be observed when introducing a flame into the model. A commonly used model to represent the impact of the flame is the n-τ-model [11]. It assumes that the flame response to a velocity perturbation at the root of the flame can be represented as a delayed fluctuation in the heat release:

$$\dot{Q}' = nu'(t-\tau). \tag{2.7}$$

Eq. (2.7) can be solved analytically in the Laplace domain, yielding

$$\dot{Q}' = ne^{-s\tau}u'(s). \tag{2.8}$$

Again, the scattering matrix relating the characteristic wave amplitudes before and after the flame can be found analytically, but including the resulting scattering matrix into the model inevitably introduces non-linear terms in s.

Solving the non-linear eigenvalue problem requires iterative procedures which may not converge to the correct solution and become costly for larger models. Furthermore, non-linear eigenvalue solvers typically only find one eigenvalue at a time and, if the basin of attraction is very small, individual eigenvalues may not be captured at all [60].

It is, therefore, useful to transform the non-linear eigenvalue problem into a linear one.

2.2 The Network Model taX

The network model *taX*, which was employed for thermoacoustic analysis throughout this thesis, is an open-source network model that was developed at the Technical University Munich [16, 21, 36]. Unlike most other implementations of thermoacoustic network models, the taX framework is based on a representation of the thermoacoustic system in the time domain as a

state-space system. This means the system equations for each element in the network model relate the input u and the output y in terms of the element matrices A_e, B_e, C_e, and D_e, as

$$\dot{x_e} = A_e x + B_e u, \tag{2.9a}$$
$$y = C_e x + D_e u. \tag{2.9b}$$

By interconnecting these matrices [18], the global system matrices are obtained:

$$\dot{x} = Ax + Bu, \tag{2.10a}$$
$$y = Cx + Du. \tag{2.10b}$$

The linear eigenvalue problem is obtained by transforming (2.10b) into the frequency domain:

$$(A - sI)q = 0, \tag{2.11}$$

where the Laplace variable s represents the system eigenvalue and q is the associated eigenfunction. The eigenvalue can be decomposed into a real and an imaginary part $s = 2\pi i f + \sigma$, where f is the frequency and σ is the growth rate. A system is linearly unstable, if it features eigenvalues with positive growth rate $\sigma > 0$. The linearity of the eigenvalue problem in Eq. (2.11) offers a compelling advantage to frequency domain considerations. On the other hand, unlike frequency domain models, the taX framework is not able to directly incorporate non-linear analytical expressions. This problem appears in particular for the duct element (*c.f.* Eq. (2.6)) and the flame element.

For the duct element, a solution is readily found by spatially discretizing Eq. (2.4), which leads to a system of the form

$$\dot{x} = Ax + Bu, \tag{2.12}$$

where x is a vector containing the discretized wave amplitudes f_i, g_i and ς_i.

For the n-τ flame element, a state-space representation can be retrieved by introducing the auxiliary state $\tilde{x}$, which is transported along the artificial θ-coordinate at speed 1. The boundaries of $\tilde{x}$ determine the time delay of the flame response [15]:

$$\frac{\partial \tilde{x}}{\partial t} + \frac{\partial \tilde{x}}{\partial \theta} = 0, \tag{2.13a}$$
$$\tilde{x}(t)|_{\theta=0} = u'(t), \tag{2.13b}$$
$$\tilde{x}(t)|_{\theta=\tau} = u'(t-\tau). \tag{2.13c}$$

Subsequent spatial discretization of this artificial advection equation casts the flame model into a state-space model. By increasing the resolution, the accuracy may be improved. This represents a significant advantage to approximation schemes like a rational polynomial approximation of the exponential function and, in contrast to other state-space approaches (*c.f.* [73]) preserves the linearity of the model in the presence of a flame.

The same approach may be applied to other, more complex time-delay transfer functions, including FTFs that are based on the finite impulse response $\mathscr{F} = \sum_k h_k e^{-ik\Delta t}$ (*c.f.* [67]).

2.3 Thermoacoustic Network Models - A Literature Review

Since they are highly adaptive and efficient to use, low-order network models have been applied in a large number of studies, be it to analyze the stability behavior of a specific model or to shed light on observations that had thus far remained unexplained. The present literature review introduces the most well-known, publicly available software frameworks. However, there are numerous network model tools beyond those introduced herein (*c.f.*[3, 42]).

One of the first established network model frameworks is the Rolls-Royce/Cambridge LOTAN tool, introduced by Dowling and Stow [14]. Similarly to taX, LOTAN is based on a plane wave approach where the acoustic equations are expressed in terms of the characteristic wave amplitudes, also referred to as Riemann invariants. However, the equations are solved in the frequency domain as a non-linear eigenvalue problem, entailing the disadvantages mentioned above. Among others, LOTAN has been used to obtain bifurcation diagrams of horizontal Rijke tube [8] and to predict and analyze the modes of a full annular combustor while making use of measured flame transfer functions [47].

A more recent but very similar model, called Oscilos [45], was developed at Imperial College, London. It has, for instance, been used for the analysis of thermoacoustic limit cycles [44] or to study the non-linear coupling of thermoacoustic modes in annular combustors [85].

In comparison to these two models, taX offers a range of benefits. As described in the previous section, taX does not suffer from the shortcomings of a non-linear solver, but is able to capture all eigenvalues of the system by solving the linear eigenvalue problem. Moreover, since it is based on the discretization of the linearized conservation equations, taX can also incorporate more elaborate physics, for example, mean flow effects or acoustic–vortex interactions. However, these advantages come at a price: the discretization introduces multiple non-physical eigenvalues and increases the numerical error, both of which need to be taken into account for the analysis of the results. In addition, multiple degrees of freedom are added to the model. As a result, the taX system matrices are comparatively large, especially for complex geometries like annular combustors, whose modeling requires multiple duct and flame elements. A solution for this last issue was proposed by Haeringer *et al.* [29], who derived Bloch wave boundary conditions in time domain and used them to reduce the number of degrees of freedom of the taX system.

In conclusion, while the LOTAN and Oscilos network model frameworks have played significant roles in analyzing thermoacoustic systems, the taX framework presents a very favorable compromise of achievable model accuracy and complexity of the resulting numerical problem, thus offering a promising framework for future research.

3 Adjoint Design

The analysis of a thermoacoustic system by means of a thermoacoustic network model yields the system eigenvalues, some of which may be found unstable, *i.e.* their growth rate is larger than zero. In order to stabilize the system, the parameters have to be modified such that all eigenvalues become stable. One way of doing this is using a step-by-step *Finite Difference* approach, where, to determine the influence of a single parameter, all eigenvalues are re-calculated after applying a small change to the parameter. Hence, determining the most influential parameters requires a rerun of the eigenvalue calculation of each parameter. This trial-and-error approach is evidently costly in terms of time and computational resources when there is a large number of parameters, thus calling for an alternative method.

With the adjoint method, the sensitivity of an eigenvalue with respect to *all* input parameters can be simultaneously calculated in just one additional calculation, with a runtime of the same order as the original simulation. For a large number of parameters (input quantities) and a small number of unstable eigenvalues (output quantities), which is commonly the case for thermoacoustic problems, adjoint design is much more efficient than the finite difference approach.

This chapter presents the fundamental mathematical concept of adjoint equations. Furthermore, the chapter summarizes and describes known applications of adjoint design in the field of thermoacoustics.

3.1 The adjoint formalism

The thermoacoustic network model introduced in the previous section is based on a state-space formalism, which results in a linear eigenvalue problem. However, other network models and Helmholtz solvers typically solve a non-linear eigenvalue problem. The following derivation of adjoint methods is, therefore, based on the more general non-linear case given as

$$L\{s, p\}q = 0. \tag{3.1}$$

The variable p represents the system parameters, s is the complex eigenvalue, and q is the associated eigenfunction.

The adjoint function is defined by a bilinear form that states

$$\langle q^\dagger, Lq\rangle - \langle L^\dagger q^\dagger, q\rangle = const, \tag{3.2}$$

where $q^\dagger$ is the adjoint eigenfunction and $L^\dagger$ the adjoint operator. In this thesis, the inner product between two functions $f(x)$ and $g(x)$ is defined as

$$\langle f|g\rangle = \int f^*(x)g(x)dx. \tag{3.3}$$

Equivalently, the discrete bilinear form is given by the Hermitian inner product of two vectors v_1 and v_2

$$\langle v_1 | v_2 \rangle = v_1^H v_2, \tag{3.4}$$

where v_1^H denotes the complex transpose of v_1.

The adjoint system corresponding to Eq. (3.1) reads:

$$L^\dagger\{s^*, p\} q^\dagger = 0. \tag{3.5}$$

The adjoint operator $L^\dagger\{s^*, p\}$ can be derived in two ways:

1. $L^\dagger$ is analytically derived from the continuous direct equations and Eq. (3.5) is numerically solved afterward (CA, Continuous Adjoints).
2. The adjoint equations are derived from the discretized form of the direct equations (3.1) (DA, Discrete Adjoint). In this case, $L^\dagger$ is not an operator, but a matrix.

In order to derive the CA equations, Eq. (3.2) is integrated by parts. The adjoint boundary conditions are obtained by setting the boundary terms arising in the integration by parts to zero.

The derivation of the CA is cumbersome, error-prone, and needs to be carried out anew for each new set of equations modeling a thermoacoustic system. However, the interpretation of the continuous adjoint equations may offer additional insight into the system dynamics and help improve understanding of the underlying physics.

In contrast, there is a general adjoint formulation for the DA. Pre-multiplying Eq. (3.1) by a test function $q^\dagger$ and using the corresponding definition of the inner product as defined in Eq. (3.4) yields:

$$\langle q^\dagger | L\{s, p\} q \rangle \tag{3.6a}$$
$$= q^{\dagger H} \left(L\{s, p\} q \right) \tag{3.6b}$$
$$= q^H L^H \{s, p\} q^\dagger \tag{3.6c}$$
$$\langle q | L^H \{s, p\} q^\dagger \rangle. \tag{3.6d}$$

If Eq. (3.6a) is satisfied for arbitrary vectors q, $q^\dagger$ is called the left, or adjoint, eigenvector [38]. The direct and adjoint eigenvector form a bi-orthogonal basis [28, 46]:

$$\langle q_i^\dagger | q_j \rangle = 0, \qquad \text{for } i \neq j. \tag{3.7}$$

From Eq. (3.6d), the definition of the adjoint operator matrix $L^\dagger$ follows as:

$$L^\dagger\{s, p\} = L^H\{s, p\}. \tag{3.8}$$

Since $L^\dagger$ is explicitly given in terms of the direct operator matrix L, implementing the DA approach is much more straightforward than the CA. However, the eigenfunctions calculated via the DA approach may feature spurious oscillations at the boundaries (*c.f.* [38] Sec.IV B for a detailed explanation). These non-physical oscillations are numerical artifacts that may severely aggravate interpreting the results. An exemplary illustration is given in chapter Sec. 5.2.4.

3.1.1 Calculation of the adjoint sensitivities

A compelling strength of adjoint methods is the efficient calculation of system sensitivities. There are two types of sensitivities:

- The *base state sensitivity*, which describes the eigenvalue shift of the base system due to small changes in the system parameters p_i. By analyzing the base state sensitivity for the most unstable eigenvalue, one can identify influential parameters and how to change them in order to stabilize the system.
- The *feedback sensitivity*, where the system is perturbed by adding an external feedback mechanism to the model equations, *e.g.* to model the impact of passive damping devices. By analyzing the feedback sensitivity, the optimal configuration of the feedback mechanism may be determined, yielding the most stabilizing effect.

For both the CA and the DA approach, the base state sensitivity can be derived by perturbing the operator (or, in case of the DA, the operator matrix) $L\{s,p\}$, which results in a shift of the eigenvalue s and the associated eigenfunction q

$$L\{s,p\} \rightarrow L\{s,p\} + \epsilon\delta L\{s,p\}, \tag{3.9a}$$

$$s \rightarrow s + \epsilon\delta s, \tag{3.9b}$$

$$q \rightarrow q + \epsilon\delta q. \tag{3.9c}$$

For non-degenerate eigenvalues, this modifies the general eigenvalue problem to

$$\left(L\{s,p\} + \epsilon\delta s\frac{dL\{s,p\}}{ds} + \epsilon\delta L\{s,p\}\right)\left(q + \epsilon\delta q\right) + \mathcal{O}\left(\epsilon^2\right) = 0. \tag{3.10}$$

Considering only terms of order ϵ reduces Eq. (3.10) to

$$L\{s,p\}\delta q + \delta s\frac{dL\{s,p\}}{ds}q + \delta L\{s,p\}q = 0. \tag{3.11}$$

For the DA framework, a general expression for the eigenvalue shift is obtained by using the inner product (Eq. (3.4)) and pre-multiplying the equation by the adjoint eigenfunction $q^\dagger$ (for which $\langle q^\dagger, La\rangle = 0$ for any vector a):

$$\delta s = -\frac{\langle q^\dagger, \delta L\{s,p\}q\rangle}{\langle q^\dagger, \frac{dL\{s,p\}}{ds}q\rangle}. \tag{3.12}$$

If p is a vector containing multiple system parameters, the sensitivity of the i^{th} eigenvalue s_i with respect to changes in the parameter p_j can be determined by

$$\frac{\delta s_i}{\delta p_j} = -\frac{\langle q_i^\dagger | \frac{\partial L}{\partial p_j} q_i\rangle}{\langle q_i^\dagger | \frac{\partial L}{\partial s_i} q_i\rangle}. \tag{3.13}$$

Calculating the base state sensitivity via the DA, hence, only requires the calculation of the left eigenvector and the evaluation of Eq. (3.13), provided that the shift of the operator matrix

due to changes in p_j is known. Note, however, that this is typically not the case in a network model, as the software interconnects the element matrices to a system matrix, whose parameter dependencies are not known explicitly.

To derive the feedback sensitivities, the governing equations are disturbed by injecting small feedback terms in the state variables. In the case of the Linear Euler Equations, a feedback mechanism is introduced by adding a mass term per unit volume per unit time $\epsilon\delta\dot{m}$, a force term per unit volume $\epsilon\delta f$, and a heat release rate term per unit volume per unit time $\epsilon\delta\dot{q}$ [38]:

$$\frac{\partial\rho'}{\partial t} + \bar{u}\frac{\partial\rho'}{\partial x} + \bar{\rho}\frac{\partial u'}{\partial x} = \epsilon\delta m, \tag{3.14a}$$

$$\bar{\rho}\frac{\partial u'}{\partial t} + \bar{\rho}\bar{u}\frac{\partial u'}{\partial x} + \frac{\partial p'}{\partial x} = \epsilon\delta f, \tag{3.14b}$$

$$\frac{\partial p'}{\partial t} + \bar{u}\frac{\partial p'}{\partial x} + \gamma\bar{p}\frac{\partial u'}{\partial x} = \epsilon\delta\dot{q}. \tag{3.14c}$$

Again, the perturbation causes a shift in the operator (matrix) $L\{s, p\}$, the eigenvalue s, and the eigenfunction q. The DA procedure to derive the eigenvalue sensitivity to a feedback mechanism is, therefore, equivalent to the base state sensitivity. However, the operator shift δL caused by external feedback is not trivially obtained and may require more extensive analysis.

3.2 Adjoints in Thermoacoustics - A Literature Review

The first appearance of the adjoint equations in literature is attributed to Lagrange in 1763. He used the adjoint formalism to reduce the order of a linear, ordinary differential equation and showed how this method may be applied to a range of problems such as fluid motion, vibrating strings, and the calculation of planet movement. Since then, adjoint methods have been applied in a large variety of scientific fields, among others to conduct sensitivity analysis, solve optimization problems, or build surrogate models, *e.g.* to speed up uncertainty quantification.

The pioneering works of Tumin and Fedorov [84] and Hill [34] finally introduced adjoints in the field of hydrodynamics. Both studies applied adjoint design for the analysis of boundary-layer instability in the wake of a cylinder. Their work set the course for a number of subsequent studies in hydrodynamic stability, the most important of which are summarized in [46].

The first study applying adjoint methods in the field of thermoacoustics was published by Juniper [37] in 2011. In this study, the author assesses the optimal initial state which leads to the onset of thermoacoustic instability in a Rijke tube. The analysis did not involve the eigenvalue sensitivity but exploited the efficiency of adjoint sensitivity calculation within the optimization routine.

The first demonstration of the efficiency of adjoint eigenvalue analysis in thermoacoustics was presented by Magri and Juniper [51]. The study includes the derivation of both the continuous and discrete adjoint sensitivities for a Rijke tube containing a hot wire. By analyzing the feedback sensitivities of the system, the authors identify the strongest stabilizing mechanism that can be applied to the system. The theoretical predictions made in the study were experimentally confirmed in Rigas *et al.* [69]. Subsequent studies extend the model used in [51]. Magri and

Juniper introduce a more accurate representation of the electrically heated Rijke tube, including a mean temperature jump at the heated mesh [50]. A compact diffusion flame is introduced in [52] and [53]. The latter analyses reveal that external forcing has the strongest effect at the tip of a flame. Furthermore, the stoichiometric mixture fraction, the width of the fuel injection slots, and the heat release are found to be the most influential parameters on the eigenvalue.

The above studies demonstrated the adjoint derivations for the first-order eigenvalue drift due to changes in the base state and open loop forcing. However, the considerations were limited to the linear analysis of the simplistic Rijke tube. An extension to non-linear eigenvalue problems and second-order terms in the eigenvalue drift is provided in [37, 48].

These primary studies inspired a series of applications of adjoint methods in thermoacoustics, among others for the analysis of conical flames [62], axisymmetric, swirling M-flames [78], and degenerate eigenvalues in annular combustors [54]. Finally, an extensive comparison of the CA and DA approach applied to a Helmholtz solver can be found in [38]. The study finds that the DA approach applied to a finite difference discretized model based on the strong form of the direct equations leads to spurious oscillations in the adjoint eigenmodes at the boundary conditions. These may be circumvented by using a finite element method for the discretization of the direct equations or, alternatively, build the model based on the weak form of equations.

In addition to their applications in stability analysis, adjoint methods offer a similar, if not more promising potential for thermoacoustic optimization problems. Thermoacoustic optimization problems typically involve a large number of tuning parameters, thus gradient-enhanced solvers may be greatly accelerated by embedding the adjoint sensitivity information. For example, Caeiro *et al.* [7] performed adjoint-based shape optimization of a Helmholtz Resonator to suppress thermoacoustic oscillations, Qadri *et al.* [68] efficiently identify the optimal placement of ignition in an axisymmetric jet by exploiting adjoint gradient calculation, and Mensah and Moeck [56] identified the optimal placement and combination of Helmholtz resonators to dampen instabilities of a 2D configuration modeling an annular combustor.

The third major field of adjoint methods in thermoacoustics is the efficient resolution of uncertainties in model predictions. Since thermoacoustic systems are highly sensitive to a large number of system parameters, uncertainties in those parameters may greatly affect the quality of model predictions. A first discussion of adjoint theory applied to uncertainty quantification for an annular combustor is laid out in [48], where the adjoint framework is included into the Active Subspace method. An alternative approach is given in [77], by using an adjoint Helmholtz solver to quantify prediction uncertainties of a combustor model based on a second-order Taylor expansion of the eigenvalue problem. Finally, the application of first- and second-order multi-parameter adjoint perturbation theory for uncertainty quantification is proposed in [57]. In all three studies, uncertainty quantification was achieved faster and more efficiently than in standard Monte Carlo simulation-based methods. A more comprehensive review of the applications of adjoint methods can be found in [49].

In conclusion, the use of adjoint methods has been instrumental in analyzing, understanding, and optimizing thermoacoustics systems. Future research may utilize the adjoint gradient to accelerate and improve the training process of data-driven models such as Gaussian process models or neural networks to efficiently predict the behavior of thermoacoustic systems.

3.3 Adjoint Analysis of Thermoacoustic Network Models

Some of the aforementioned studies use a thermoacoustic network framework to describe the direct eigenvalue problem. However, most of these are based on DA, *i.e.* the adjoint eigenvalue sensitivity is calculated using the Hermitian of the system matrix resulting from the discretized direct eigenvalue problem. A comprehensive introduction to the procedure is, for instance, laid out in [79]. While the DA approach is straightforward and readily applicable to any numerical model, it also entails some disadvantages (*c.f.* Sec. 3.1). In addition, although both the CA and the HA approaches should, in principle, converge, various studies showed that convergence is not guaranteed (*e.g.* [4, 25]).

As a result, there have been a number of studies dedicated to the integration of CA into existing network frameworks.

An example of the CA approach applied to a network model is shown by Aguilar *et al.* [1]. The study introduces a wave-based adjoint network model for a simple system configuration, where the (continuous) adjoint equations and jump conditions are derived for each element of the thermoacoustic system. Having an explicit form of the adjoint equations may help to get some additional insight into the underlying physics of the system. However, deriving the adjoint equations anew for each new model is both error-prone and time-consuming.

Chapter "Contextualization of Papers", Sec. 5.2, therefore describes a novel approach to implementing adjoint design in existing network frameworks.

4 Exceptional Points

Highly sensitive eigenvalues may complicate the prediction and control of thermoacoustic instability. More specifically, an eigenvalue that has been predicted stable may become unstable for small changes in one or several parameters [39].

Parameter sensitivities and the resulting prediction uncertainties may even be enhanced for specific parameter settings, due to the existence of so-called exceptional points (XPs). The occurrence of XPs is associated with unusual physical behavior and has been studied in several scientific fields such as mechanics, electromagnetism, and quantum physics [33]. In thermoacoustics, XPs have only recently become a topic of interest. However, understanding their impact on thermoacoustic instability may be crucial to the design and control of thermoacoustic systems.

This chapter introduces the mathematical concept of XPs and the associated characteristics, and outlines their significance in thermoacoustic stability analysis.

4.1 Characteristics of Exceptional Points

Exceptional points occur when the characteristic equation resulting from the eigenvalue problem (Eq. (3.1)) has a multiple root solution in the eigenvalue s. Mathematically, this means that the algebraic multiplicity a of the eigenvalue is larger than one, in which case s is called a degenerate eigenvalue. XPs differ from other degenerate eigenvalues in the relationship between their algebraic and geometric multiplicity. The geometric multiplicity g is the dimension of the eigenspace of the eigenvalue s, *i.e.* the number of linearly independent eigenvectors associated with s. In the case of an XP, the algebraic multiplicity is larger than the geometric multiplicity $a > g$, as not only the eigenvalues but also their associated eigenfunctions coincide.

Exceptional points exhibit a set of characteristic features, which will be further explained throughout this section:

1. At the XP two (or more) eigenvalues and their associated eigenfunctions coalesce.
2. In the immediate vicinity of a two-fold XP (*i.e.* $a = 2$) the system can be represented by a two-dimensional problem. The dynamics of this reduced system are determined by the two eigenvalues that coalesce at the XP.
3. At the XP, the bi-orthogonality of the direct and adjoint eigenvector does not hold.
4. The eigenvalue sensitivity at the exceptional point is infinitely large. As a result, eigenvalue trajectories are strongly deflected in the vicinity of exceptional points.

5. Looping in the parameter space results in a half-circle of the eigenvalues. A complete circle in the eigenvalue space requires two loops in the parameter space.

4.1.1 Model reduction at the XP

In the immediate vicinity of an exceptional point, the system can be locally described by a 2x2 matrix [40]. Examples of the reduction procedure are given in [9, 31]. For an exemplary generic, two-dimensional system with a complex parameter δ

$$L(\delta) = \begin{bmatrix} 1 & \delta \\ \delta & 1 \end{bmatrix}, \tag{4.1}$$

the characteristic equation $\det(L(\delta) - sI) = 0$ yields the eigenvalues

$$s_1 = \sqrt{1+\delta^2}, \qquad s_2 = -\sqrt{1+\delta^2}. \tag{4.2}$$

The associated eigenvectors read:

$$q_{1,2}(\delta) = \begin{bmatrix} -\delta \\ 1 \pm \sqrt{1+\delta^2} \end{bmatrix}. \tag{4.3}$$

At the two XPs $\delta = \pm i$ both the eigenvalues and the eigenvectors coalesce:

$$s_{1,2} = 0, \qquad q_{1,2}(\delta) = \begin{bmatrix} \pm i \\ 1 \end{bmatrix}. \tag{4.4}$$

This is called a "branch point singularity" and is a distinctive feature of the XP [32].

4.1.2 Bi-orthogonality at the XP

Recall from the previous chapter that direct (right) and adjoint (left) eigenvectors form a bi-orthogonal basis (Eq. (3.7)). The identity holds for both eigenvalues at the XP, *i.e.* $i \to XP^+$ and $j \to XP^-$. Consequently, at the XP

$$\langle q^\dagger_{XP} | q_{XP} \rangle = 0. \tag{4.5}$$

This relation, known as self-orthogonality, is a characteristic property of the XP. It can easily be checked for the two-dimensional example introduced above:

$$\begin{bmatrix} i & 1 \end{bmatrix} \begin{bmatrix} i \\ 1 \end{bmatrix} = 0, \qquad \begin{bmatrix} -i & 1 \end{bmatrix} \begin{bmatrix} -i \\ 1 \end{bmatrix} = 0. \tag{4.6}$$

4.1.3 Infinite sensitivity and mode veering at the XP

The perturbation expansion at an XP follows the fractional power series, known as Puiseux series $s = s_0 + \sum_{j=1}^{n} s_j (\epsilon_j - \epsilon_0)^{j/a}$ [40]. A first-order expansion close to a two-fold XP ($a = 2$, $g = 1$) yields

$$s = s^* + s_1 \sqrt{\epsilon_i - \epsilon_{i,XP}} + \mathcal{O}(\epsilon_i - \epsilon_{i,XP}), \quad \epsilon_i \to \epsilon_{i,XP}, \tag{4.7}$$

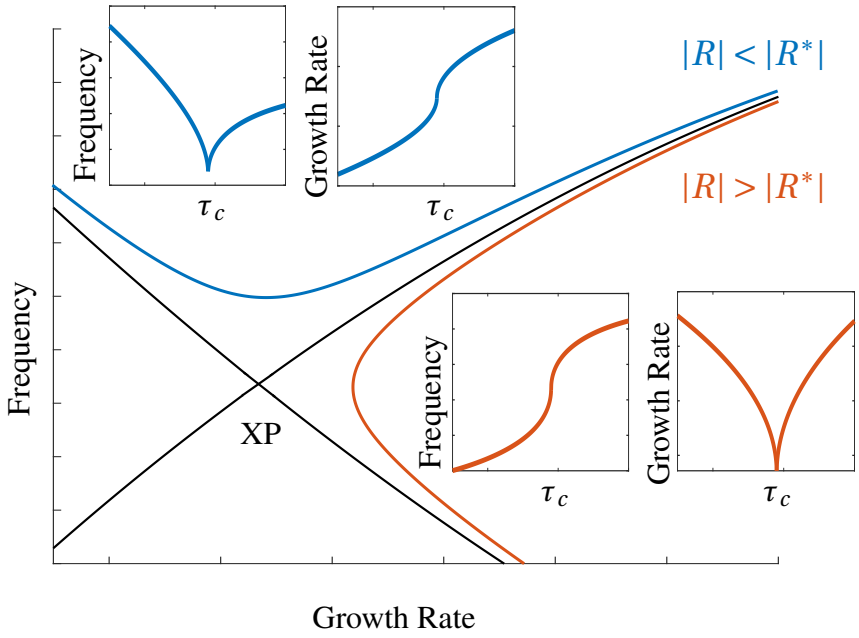

Figure 4.1: Eigenvalue trajectories at and around the exceptional point.

where ϵ_i is i-th parameter, s^* is the eigenvalue at the XP and s_1 is a constant. The sensitivity of the XP results as:

$$\frac{\partial s}{\partial \epsilon_i} = \frac{s_1}{2\sqrt{\epsilon_i - \epsilon_{i,XP}}} + h.o.t. \tag{4.8}$$

As $\epsilon_i \rightarrow \epsilon_{i,XP}$, the right side in Eq. (4.8) approaches infinity, thus indicating that the eigenvalue sensitivity at the XP becomes infinite. In addition, the sensitivity undergoes a change of sign at the exceptional point.

As a result, eigenvalues approaching an XP are subject to sudden shifts in sensitivity, entailing strongly varying responses to parameter changes [64].

The infinite sensitivity at the XP is paralleled by strong mode veering in its immediate vicinity. As a result, eigenvalues approaching an XP are subject to sudden shifts in sensitivity, entailing strongly varying responses to parameter changes [64]. Next to strong veering effects, two distinctly different trajectories emerge in close vicinity of the exceptional point. Heiss and Harney [31] describe their behavior as follows:
"*In one of the cases, the two levels avoid each other while their widths cross, in the other case, the two levels cross while their widths avoid each other.*"
Figure 4.1 illustrates these two cases: For a thermoacoustic system the flame parameter τ_c is varied where the outlet reflection coefficient R is set to (i) $R = R^*$, which corresponds to the parameter setting at the XP (black trajectories), (ii) a value slightly smaller than R^* (blue trajectories) and (iii) a value slightly larger than R^* (orange trajectories).

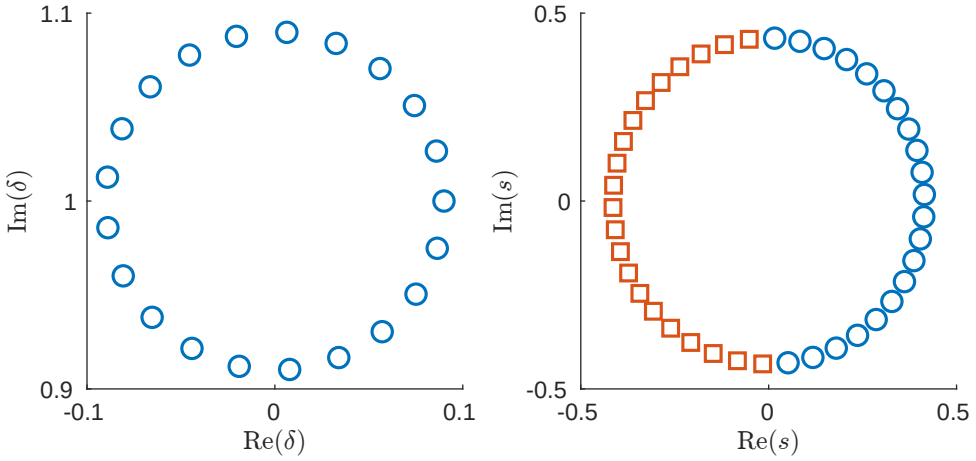

Figure 4.2: Left: Circle in the parameter space δ with the exceptional point at $\delta = i$ at the center; right: Eigenvalues s_1 (squares) and s_2 (circles) calculated for the parameter values depicted on the left.

4.1.4 Parameter looping at the XP

A closed loop in the parameter space in close vicinity to an XP results in an open loop in the eigenvalue. In other words, to get a closed loop in the eigenvalue, one has to perform two loops in the parameter space. This behavior can be demonstrated by calculating the eigenvalues for the parameters $\delta(\varphi) = i + e^{i\varphi}$ around the XP [9]. For the simple example above, the eigenvalues $s_{1,2}$ can be analytically determined as

$$s_{1,2} = \pm\sqrt{1 + (i + e^{i\varphi})^2}. \tag{4.9}$$

The results are plotted in Fig. 4.2, illustrating the looping behavior around the XP.

4.2 Exceptional Points in Thermoacoustics

In the context of thermoacoustics, the effects of XPs have been observed in several studies without drawing conclusions about their origin. For example, Sogaro *et al.* [79] observe noticeably large eigenvalues sensitivities along with strong mode veering. Mensah *et al.* [58] were the first to unequivocally identify an exceptional point in a thermoacoustic model. The publication considers a simple system that is modeled by the Helmholtz equation, with the flame being modeled as an n-τ transfer function. A global contour-integral-based method is used to identify the exceptional point and lay out its effects on nearby eigenmodes. Subsequent studies [75, 80] identified XPs as the root cause for parameter ranges with heightened sensitivity and the associated mode veering. In these primary studies, the occurrence of XPs in thermoacoustic systems is connected to the coalescence of modes of different nature, *i.e.* acoustic and ITA modes. (For further information about intrinsic thermoacoustic modes see, for example, [17, 35, 74]). However, as Orchini *et al.* [64] showed, XPs may also emerge from the coalescence of two acoustic modes. The method to locate this kind of XP is based on the infinite sensitivity at the XP, and

will be elucidated in detail in Sec. 5.3.2, together with a third approach that locates XPs by means of higher-order perturbation theory [63]. Orchini *et al.* [64] further study the interplay of thermoacoustic and ITA modes, finding that even stable XPs may influence the stability behavior of a system by introducing strong changes in the eigenvalues sensitivities. In [23], an equivalent observation is made for the interplay of mode clusters, which were initially observed in an annular combustor in [6].

The existence of XPs in thermoacoustic systems could also be observed experimentally: Bourquard and Noiray [5] experimentally and analytically studied a tunable damping system that features an XP for a specific setting of the purge mass flow, showing that stabilization is most effective at the exceptional point. Finally, Ghani *et al.* [24] identify branch-switching at the XP as the primary reason for observed sudden shifts in the stability of thermoacoustic systems.

The identification of XPs has greatly improved the fundamental understanding of thermoacoustic systems and the effects of mode interplay. However, there still remain a number of questions, *e.g.* how do XPs affect the non-linear behavior of thermoacoustic systems and what are ways to utilize XPs to optimize system behavior?

5 Contextualization and Discussion of Publications

The present chapter discusses the publications that constitute this thesis. The network model introduced in Sec. 2.2 introduces a duct element, where the cross-sectional area and mean temperature are uniform along the duct axis. In *Low-order Network Model of a Duct with Non-Uniform Cross-Section and Varying Mean Temperature in the Presence of Mean Flow* (reference PAPER_DUCT [70]) a new version of the duct element is introduced, which is capable of taking into account both temperature and geometry variations. The same network model tool is used in *A Hybrid Adjoint Network Model for Thermoacoustic Optimization* (reference PAPER_HA [72]). The study proposes an alternative formalism of the adjoint method to those introduced in Sec. 3.1, which can be easily integrated into any existing network model. An application of adjoint analysis is presented in *The Impact of Exceptional Points on the Reliability of Thermoacoustic Stability Analysis* (reference PAPER_XP [71]). In that study, the adjoint sensitivity is used to accelerate the identification process of exceptional points. The study reveals that XP may greatly affect uncertainty propagation and the quality of surrogate model predictions. The proposed algorithm to identify exceptional points is applied in *Interplay of Clusters of Acoustic and Intrinsic Thermoacoustic Modes in Can-Annular Combustors* (reference PAPER_ITA [23]). The study finds that mode veering in the vicinity of an XP strongly plays a crucial role in understanding the trajectory behavior of acoustic and ITA clusters.

5.1 The Duct Element with Varying Cross-Section and Mean Temperature Distribution

The geometry of combustors is commonly strongly simplified in thermoacoustic network models. The duct element, which is central to any model as it is the only element with axial extent (*c.f.* Sec. 2.2), assumes that all mean properties are constant along the longitudinal duct axis. Consequently, temperature variations resulting from heat transfer effects along the duct are unaccounted for. In addition, the duct cross-section is considered constant, significantly limiting the geometric complexity that can be represented by a simple model. Gradually changing cross-sectional areas are modeled as a sequence of duct elements with constant cross-sections, connected by area jumps. If one wants to include the impact of temperature variations, conventional modeling additionally requires temperature jumps at the appropriate position.

For a given temperature distribution, *e.g.* obtained from a preliminary steady-state CFD simulation, building a model this way entails a loss of information if the numerical resolution of the CFD is not matched. However, preventing this might require an excessive number of elements, resulting in an overly large and cluttered system.

Consequently, the integration of an extended duct element, which is able to take both geometry and temperature variations into account, may greatly accelerate the set-up of a new model and at the same time improve the accuracy of the results. An exemplary network model employing this element is illustrated in Fig. 5.1.

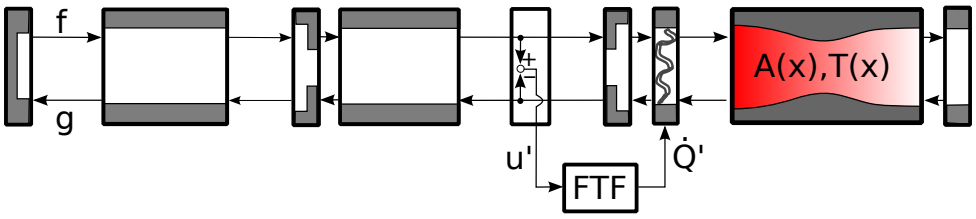

Figure 5.1: Illustration of an exemplary network model including a duct with a variable cross-sectional area and temperature profiles

In publication PAPER_DUCT, the process of designing and implementing such an element is presented. The model is based on the quasi-one-dimensional, linearized Euler equations, which read:

$$\frac{\partial p'}{\partial t} + \bar{u}\frac{\partial p'}{\partial x} + u'\frac{\partial \bar{p}}{\partial x} + \bar{p}\gamma\frac{\partial u'}{\partial x} + p'\gamma\frac{\partial \bar{u}}{\partial x} + \frac{u'\gamma\bar{p}}{A}\frac{\partial A}{\partial x} + \frac{\gamma\bar{u}p'}{A}\frac{\partial A}{\partial x} = 0, \tag{5.1a}$$

$$\frac{\partial u'}{\partial t} + u'\frac{\partial \bar{u}}{\partial x} + \bar{u}\frac{\partial u'}{\partial x} + \frac{1}{\bar{\rho}}\frac{\partial p'}{\partial x} + \frac{p'\bar{u}}{\gamma\bar{p}}\frac{\partial \bar{u}}{\partial x} - \frac{\bar{u}s'}{c_p}\frac{\partial \bar{u}}{\partial x} = 0. \tag{5.1b}$$

Subsequently, the system is cast to generalized coordinates following the procedure outlined in [18]:

$$\begin{bmatrix} \frac{p'}{\bar{\rho}c} \\ u' \end{bmatrix} = \begin{bmatrix} 1 & 1 \\ 1 & -1 \end{bmatrix} \begin{bmatrix} f \\ g \end{bmatrix}. \tag{5.2}$$

The resulting system of partial differential equations is transformed into a state-space formalism by discretizing the characteristic waves f and g in time using a third-order upwind scheme. The resulting model equations differ from the standard duct element, as they introduce a coupling between the f and g waves, which results from the change of impedance within the duct.

Comparisons with analytical solutions derived in [82, 83] and [43] show excellent agreement with the network model results.

5.2 Hybrid Adjoints

There are several possibilities for the integration of adjoint methods into an existing thermoacoustic network tool.

1. A ready solution is offered by the discrete adjoint. By extending the software framework by a single script, the adjoint sensitivities may be calculated for any kind of model, *i.e.* any combination of network elements. Within the additional script, the program evaluates the complex conjugate of the original system matrix in which the direct equations have already been discretized for numerical solving.

2. A more elaborate approach is given by the continuous adjoint. Here, the adjoint equations need to be derived and implemented for each element.

For a more detailed explanation of the CA and DA approach, see Sec. 3.1.

For a network solver, the spurious oscillations observed in [38] occur not only at the boundary conditions, but also at the interconnections of the network elements. Considering that a network model is composed of multiple elements, these oscillations may significantly impair the quality of the results and complicate the interpretation thereof. Ref. [38] shows that these oscillations can be eliminated by (i) changing the discretization scheme or (ii) using the direct equations in their weak form. However, both of these solutions would require substantial changes to an existing network model, possibly entailing unwanted effects on the prediction quality.

By implementing the CA approach, the direct network solver does not have to be fundamentally modified, yet spurious oscillations are entirely avoided. However, the CA requires the derivation and implementation of the adjoint equations for each element, thus requiring comparably large resources and an increased risk of erroneous results.

Publication PAPER-HA, introduces a hybrid approach that is both easy to implement and at the same time eliminates spurious oscillations in the eigenmodes. The HA method is based on the continuous adjoint equations but works within the framework of the network tool, where the direct equations have already been discretized. It exploits the self-adjoint character of the duct element to find a general transformation matrix for the remaining, compact network elements, thus eliminating the need to derive the CA equations for each element.

5.2.1 Methodology of the HA approach

This section summarizes the derivations of the HA approach that is presented in PAPER_HA. A more detailed derivation of the fundamental equations can be found in the original publication.

The adjoint duct equations are derived by creating a Lagrange functional of the Linearized Euler equations (2.2). The resulting adjoint equations in terms of the adjoint characteristic wave amplitudes $f^\dagger$ and $g^\dagger$ (neglecting entropy waves) read

$$\frac{\partial}{\partial t}\begin{bmatrix} f^\dagger \\ g^\dagger \end{bmatrix} = \frac{\partial}{\partial x}\begin{bmatrix} c+\bar{u} & 0 \\ 0 & \bar{u}-c \end{bmatrix}\begin{bmatrix} f^\dagger \\ g^\dagger \end{bmatrix}. \tag{5.3}$$

The system of equations is equivalent to the direct duct equations (2.4), demonstrating the self-adjoint property of the duct. Hence, instead of implementing a new, adjoint duct element, the adjoint system may be determined based on the direct duct element of the original network software. The partial integration performed on the Lagrangian further provides the relationship between direct and adjoint boundary terms at the up- and downstream ends of the duct at $x = 0$ and $x = L$:

$$\left[\bar{\rho} g g^\dagger (c-\bar{u}) - \bar{\rho} f f^\dagger (c+\bar{u})\right]_0^L = 0. \tag{5.4}$$

Equation (5.4) is central to the derivation of the HA. Based on the boundary terms, the paper demonstrates how to derive a generalized transformation to calculate the adjoint scattering matrix based on any original scattering matrix.

The following illustrative example of two ducts that are connected via an area jump is used to demonstrate the simplicity and viability of the HA approach (Fig 5.2):

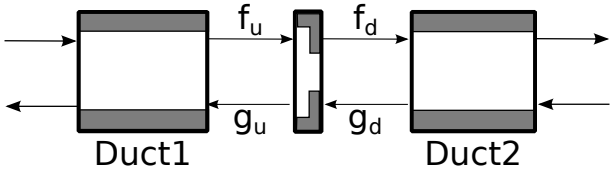

Figure 5.2: Illustration of two duct elements connected by an area jump.

Since the area jump represents an acoustically compact discontinuity, both ducts feature boundary terms from Eq. (5.4) at the position of the area jump. More specifically, the downstream boundary conditions of the upstream duct and the upstream boundary conditions of the downstream duct yield:

$$\begin{aligned} &g_u g_u^{\dagger} \bar{\rho}_u (c_u - \bar{u}_u) - f_u f_u^{\dagger} \bar{\rho}_u (c_u + \bar{u}_u) - \\ &\left(g_d g_d^{\dagger} \bar{\rho}_d (c_d - \bar{u}_d) - f_d f_d^{\dagger} \bar{\rho}_d (c_d + \bar{u}_d) \right) = 0. \end{aligned} \tag{5.5}$$

By inserting the relationship between the incoming and outgoing waves given by the scattering matrix S (Eq. (2.5)) of the discontinuity, a general transformation formalism for the adjoint scattering matrix is obtained:

$$S^{\dagger} = \frac{1}{det(S)} \begin{bmatrix} \frac{S_{22}(\bar{c}_u + \bar{u}_u)}{(\bar{c}_u - \bar{u}_u)} & -\frac{S_{21}\bar{\rho}_d(\bar{c}_d - \bar{u}_d)}{\bar{\rho}_u(\bar{c}_u - \bar{u}_u)} \\ -\frac{S_{12}\bar{\rho}_u(\bar{c}_u + \bar{u}_u)}{\bar{\rho}_d(\bar{c}_d + \bar{u}_d)} & \frac{S_{11}(\bar{c}_d - \bar{u}_d)}{(\bar{c}_d + \bar{u}_d)} \end{bmatrix}. \tag{5.6}$$

With this identity, any scattering matrix of the form Eq. (2.5) can be cast into its corresponding adjoint scattering matrix without deriving the adjoint equations. Consequently, the network model tool only needs to be extended by one additional script, which calculates the adjoint scattering matrix and reruns the system, using the same interconnection mechanism as for the direct problem.

The calculation of base state and feedback sensitivities based on the HA approach follows from the identity:

$$\delta s \frac{\partial \mathscr{L}}{\partial s} + \delta \xi \frac{\partial \mathscr{L}}{\partial \xi} = 0. \tag{5.7}$$

The first term of the equation constitutes the normalization condition for the adjoint eigenmodes:

$$\frac{\partial \mathscr{L}}{\partial s} = 0. \tag{5.8}$$

Depending on the complexity of the system, the derivation, especially of the normalization condition, may involve some more advanced derivations, yet the effort is still lower than the CA.

Additional complexity is also introduced by the duct element with variable mean temperature and cross-section (Sec. 5.1). As this element is neither compact nor self-adjoint, it has to be considered separately for the implementation of HA. However, since the extended duct may also be modeled as a sequence of ducts and compact area and/ or temperature jumps, it is evident that it does not affect the calculation of the adjoint scattering matrix.

5.2.2 Review of Aguilar et al.

As the HA is based on the CA equations and, consequently, entails the same numerical advantages, this thesis emphasizes the advantages of the HA over the CA approach. This section, therefore, takes a closer look into the implementation of the conventional CA approach, as proposed by Aguilar *et al.* [1].

For comprehensibility, the simpler of the two cases introduced in the study will be summarized. The thermoacoustic model comprises a duct with up- and downstream reflection coefficients R_u and R_d, respectively, and a heating gauze located at axial position $x = b$. The LEEs (2.3) produce the following fluctuation equations (where $\bar{u} = 0$):

$$\bar{\rho}\frac{\partial u'}{\partial t} + \frac{\partial p'}{\partial x} = 0, \tag{5.9a}$$

$$\frac{\partial p'}{\partial t} + \gamma\bar{p}\frac{\partial u'}{\partial x} = 0, \tag{5.9b}$$

along with the jump conditions:

$$\left[p'\right]_{b^-}^{b^+} = 0, \tag{5.10a}$$

$$\left[u'\right]_{b^-}^{b^+} = \frac{\gamma - 1}{\gamma\bar{p}}\int_{b^-}^{b^+} q' dx. \tag{5.10b}$$

The unsteady heat release at the gauze is modeled using the n-τ-model [11]. For the derivation of the adjoint system, the equations and jump conditions are transformed into the frequency domain using $[\cdot]' = \hat{[\cdot]}e^{st}$, yielding the following:

$$E_1 := s\bar{\rho}\hat{u} + \frac{d\hat{p}}{dx} = 0, \tag{5.11a}$$

$$E_2 := s\hat{p} + \gamma\bar{p}\frac{d\hat{u}}{dx} = 0, \tag{5.11b}$$

and

$$J1 := \left[\hat{p}\right]_{b^-}^{b^+} = 0, \tag{5.12a}$$

$$J2 := \left[\hat{u}\right]_{b^-}^{b^+} - \beta\hat{u}(b^-)e^{-s\tau} = 0, \tag{5.12b}$$

where β is the interaction index in the flame model. In the next step, the Lagrangian functional is created:

$$\mathscr{L} := s - \langle\hat{u}^\dagger, E1\rangle - \langle\hat{p}^\dagger, E2\rangle - \langle\hat{g}^\dagger, J1\rangle - \langle\hat{h}^\dagger, J2\rangle. \tag{5.13}$$

The variables $\hat{g}^\dagger, \hat{h}^\dagger$ are the adjoint quantities corresponding to the direct jump conditions $J1$ and $J2$. Integration by parts of Eqs. (5.11) gives the adjoint set of equations:

$$-s^*\bar{\rho}\hat{u}^\dagger + \gamma\bar{p}\frac{d\hat{p}^\dagger}{dx} = 0, \tag{5.14a}$$

$$-s^*\hat{p}^\dagger + \frac{d\hat{u}^\dagger}{dx} = 0. \tag{5.14b}$$

The boundary terms arising from the integration by parts provide the jump conditions:

$$\left[\frac{\gamma\bar{p}}{\gamma-1}\hat{p}^\dagger\right]_{b^-}^{b^+} + \beta\hat{p}^\dagger(b^-)e^{-s^*\tau} = 0, \tag{5.15a}$$

$$\left[\hat{u}^\dagger\right]_{b^-}^{b^+} = 0. \tag{5.15b}$$

With the adjoint equations and boundary conditions, one can build a network for the thermoacoustic system equivalently to the direct system (*c.f.* [81]).

5.2.3 Minimal example: Adjoint area jump

In this section, the usefulness of the HA is demonstrated by analyzing a simple system consisting of a duct with an area change at axial position $x = l$. The mean flow is considered negligible, and the speed of sound is constant ($\bar{c}_u = \bar{c}_d$).

The jump conditions at the area change read:

$$\left[p'\right]_{l^-}^{l^+} = 0, \tag{5.16a}$$

$$\left[Au'\right]_{l^-}^{l^+} = 0, \tag{5.16b}$$

where A is the duct Area and l^- and l^+ the axial positions immediately up- and downstream of the jump. With $\alpha = A(l^+)/A(l^-)$ the following scattering matrix relates the f and g waves before and after the are jump (*e.g.* [76]):

$$S = \begin{pmatrix} \frac{2}{\alpha+1} & \frac{\alpha-1}{\alpha+1} \\ -\frac{\alpha-1}{\alpha+1} & \frac{2\alpha}{\alpha+1} \end{pmatrix}. \tag{5.17a}$$

To compare both approaches, the scattering matrix will first be derived using the standard CA approach. The procedure can be summarized as follows:

1. Derivation of the adjoint duct equations and boundary conditions.
2. Insertion of the direct jump conditions into the adjoint boundary conditions.
3. Insertion of the adjoint characteristic wave amplitudes and solving for the scattering matrix.

In contrast, the HA approach requires one single step to calculate the adjoint scattering matrix: Inserting the elements of the direct scattering matrix in Eq. (5.17a) into the transformation matrix given in Eq. (5.6).

Steps (1) and (2) are conducted according to the procedure outlined in Sec. 5.2.2, yielding the following set of adjoint boundary conditions:

$$\left[\hat{u}^\dagger\right]_{l^-}^{l^+} = 0, \tag{5.18a}$$

$$\left[A\hat{p}^\dagger\right]_{l^-}^{l^+} = 0. \tag{5.18b}$$

Note that the adjoint boundary conditions according to [1] need to be derived anew as soon as the direct jump conditions change, for instance, by inserting a temperature jump after the area jump. The relationship between the primitive adjoint variables $\hat{u}^\dagger, \hat{p}^\dagger$ and the adjoint wave amplitudes $f^\dagger, g^\dagger$, which follows from diagonalizing the adjoint duct equations (5.3) reads:

$$\hat{u}^\dagger = f^\dagger - g^\dagger \tag{5.19a}$$

$$\hat{p}^\dagger = \left(f^\dagger + g^\dagger\right)/c. \tag{5.19b}$$

Replacing the primitive adjoint variables in the jump conditions and solving for $f_d^\dagger$ and $g_u^\dagger$ leads to the following expression for the adjoint scattering matrix:

$$S^\dagger = \begin{bmatrix} \frac{2\alpha}{\alpha+1} & \frac{\alpha-1}{\alpha+1} \\ -\frac{\alpha-1}{\alpha+1} & \frac{2}{\alpha+1} \end{bmatrix} \tag{5.20}$$

The same result is obtained by the HA approach:

$$S^\dagger = \frac{1}{det(S)} \begin{bmatrix} S_{22} & -S_{21} \\ -S_{12} & S_{11} \end{bmatrix} = \begin{bmatrix} \frac{2\alpha}{\alpha+1} & \frac{\alpha-1}{\alpha+1} \\ -\frac{\alpha-1}{\alpha+1} & \frac{2}{\alpha+1} \end{bmatrix} \tag{5.21}$$

Evidently, both approaches yield the same scattering matrix for the adjoint area jump. However, the HA eliminates the need to derive the adjoint equations, thus delivering more reliable results more efficiently.

5.2.4 Comparison between CA, DA, and HA

In Fig. 5.3 the steps for the different adjoint approaches are summarized for a state-space network model. Both the hybrid and the discrete adjoint make use of the steps already performed by the direct network model. The HA uses the original scattering and discretized matrices but needs to perform the interconnection of the adjoint elements in order to calculate the adjoint eigenvalues and eigenvectors. The DA steps in after the interconnection of the direct matrices and, therefore, avoids a second interconnection of the adjoint matrices. Here, the adjoint system matrix is calculated by taking the conjugate transpose of the direct system matrix, also known as the Hermitian. The Hermitian is readily obtained using a reverse routine-calling algorithm [19, 46]). In contrast to the DA and HA approach, each step performed for the direct network model has to be repeated for the CA approach, demonstrating again why the implementation of the CA takes a comparably large effort. On the other hand, the derivation of the adjoint equations may offer some additional insight into the system dynamics, thus justifying the additional steps for some specific purposes.

Regarding the implementation, the DA approach represents the most efficient method to calculate the adjoint system for an existing network model. However, the eigenvectors calculated from the DA method exhibit spurious oscillations at each boundary and jump condition of the thermoacoustic network model. Hence, the eigenmodes of more elaborate models, for instance annular combustors, are misrepresented at multiple locations, which significantly impairs the

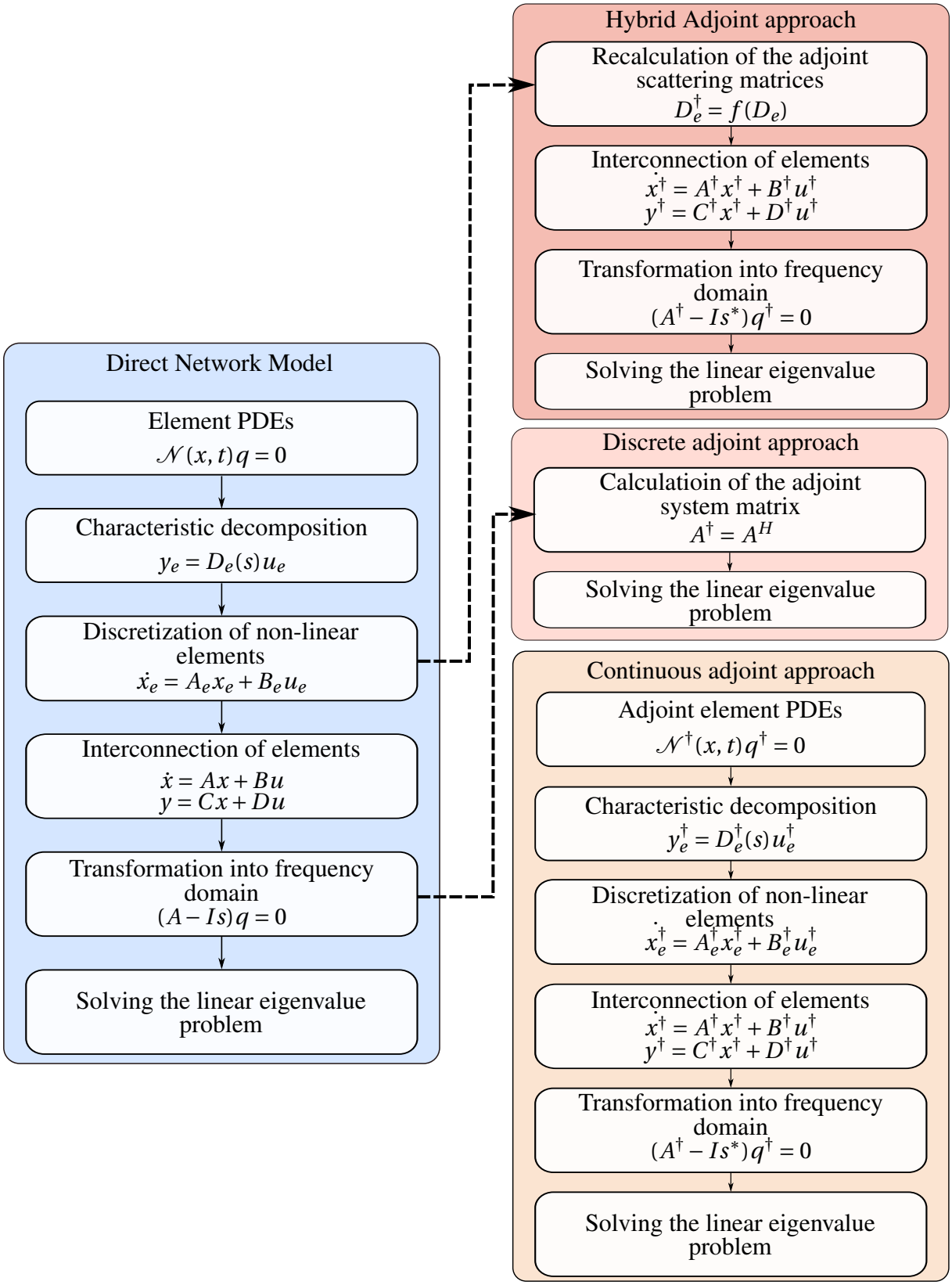

Figure 5.3: Comparison of CA, DA, and HA steps for an existing state-space network tool

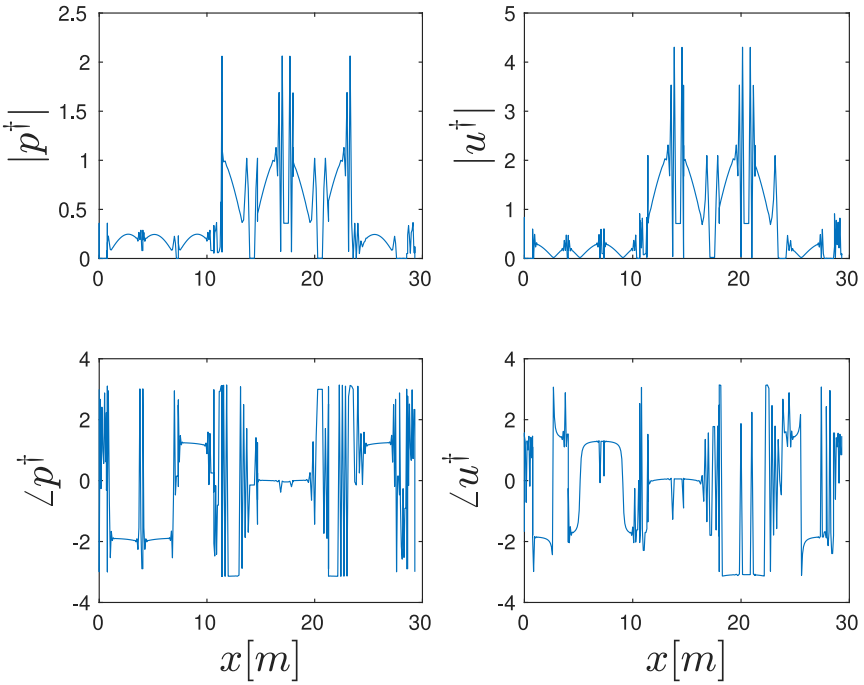

Figure 5.4: Spurious oscillations obtained when calculating the adjoint eigenvectors of the annular combustor in PAPER_XP via the DA approach.

interpretability of the results. An example of this effect is illustrated in Fig. 5.4, which is obtained for the annular combustor model studied in PAPER_HA. These oscillations are avoided by both the HA and the CA approaches.

In addition, while determining the adjoint system may be straightforward using the DA approach, calculating the base state and feedback sensitivities requires the determination of the shifted matrix δL, which may include a more extensive analysis [1].

The HA approach offers a ready solution for existing network models. Being easy to implement for a generic network model, it avoids both spurious oscillations and excessive derivations. However, normalizing the eigenfunctions according to Eq. (5.8) is not trivial and could pose a significant challenge for models that include more complex flame functions.

An overview of the advantages and disadvantages of each method is given in table 5.1. There is no general recommendation on which method is preferable, as different cases and objectives call for different approaches. However, for an existing network model based on a finite difference discretization, the HA method offers the best compromise between implementation effort and the quality of the results.

	Advantages	Disadvantages
CA	Additional insight through adjoint equations.	Effort for derivation and implementation.
DA	No derivation required. Fast implementation.	Spurious oscillations for FD discretization of the strong form of equations. Calculation of feedback sensitivity not trivial.
HA	No derivation required. Fast implementation.	Normalization not trivial.

Table 5.1: Overview of the advantages and disadvantages of the CA, DA, and HA approaches.

5.3 Exceptional Points

Exceptional points in thermoacoustics were first investigated in [58]. However, the exceptional points in previous studies either exhibited high, negative growth rates and had thus little effect on the system's instability behavior, or were associated with nonphysical parameter values like negative time lags at the flame. In PAPER_XP, the authors propose a new method to identify the parameter setting associated with an exceptional point in thermoacoustic systems. The model used for the analysis includes a realistic FTF, which results from the flame impulse response (FIR) model introduced by Komarek and Polifke [41] with the alternations proposed by Guo *et al.*[27]. This constitutes a substantial improvement to previous studies of XPs in thermoacoustic models, which were limited to simple configurations (*e.g.* a Rijke tube) and/or a rudimentary n-τ flame model. Another novelty of the study is that, with the proposed algorithm, the authors were able to identify a physically relevant, *unstable* XP for the first time in a thermoacoustic system. Based on the XP identified, the influence of XPs on the uncertainty of thermoacoustic network predictions is analyzed. The paper uses the network model introduced in Sec. 2.2.

5.3.1 Discrete adjoints in state-space network models

The study proposes a general framework to calculate the adjoint eigenvalue sensitivity based on the discrete adjoint approach. The DA is, in principle, straightforward to implement: the adjoint system matrix is calculated as the Hermitian of the direct system matrix. However, the evaluation of the eigenvalue drift of a generalized eigenvalue problem (3.1) for a change in any parameter p_i, which is given as

$$\frac{\delta s}{\delta p_i} = -\frac{\langle q^\dagger, \frac{\partial L\{s,p\}}{\partial p_i} q\rangle}{\langle q^\dagger, \frac{\partial L\{s,p\}}{\partial s} q\rangle} \tag{5.22}$$

requires knowledge of the operator derivatives $\frac{\partial L\{s,p\}}{\partial p_i}$ and $\frac{\partial L\{s,p\}}{\partial s}$.

In the case of a state-space model, the operator L is given as $L_{SS}\{s,p\} = A(p) - sI$, thus the derivative $\frac{\partial L\{s,p\}}{\partial p_i}$ is obtained from the system matrix A. In PAPER_XP, a preliminary analysis reveals that, for the parameters used in the study, A can be split into various matrices $A = A_0 + A_i(p_i)$, where the dependency of A on p_i appears only in the corresponding matrix $A_i(p_i)$. This not only allows the computation of the adjoint eigenvalue sensitivities but also eliminates the need to rebuild the system matrix by interconnecting the elements after changing the parameters.

5.3.2 Identification of XPs

In this section, the method of identifying XPs introduced in PAPER_XP is shortly introduced and differentiated from the methods proposed in [64] and [63].

5.3.2.1 Identifying XPs based on eigenvalue coalescence

In non-Hermitian system operators, exceptional points can be found for a specific configuration in two real design parameters [9, 33]. Schaefer *et al.*(PAPER_XP) tune the time delay τ_c of the flame model and the downstream reflection coefficient R_{out} to identify XPs. The time lag τ_c can be interpreted as the time needed for an inertial wave to propagate from the swirl generator to the flame base [2], whereas damping devices or the turbine working conditions determine the value of R_{out} [65].

The algorithm to identify the values of τ_c and R_{out} at an XP is graphically illustrated in Fig. 5.5. The solver requires two initial eigenvalues $s_{A,0}$ and $s_{B,0}$ which coalesce at the sought after XP.

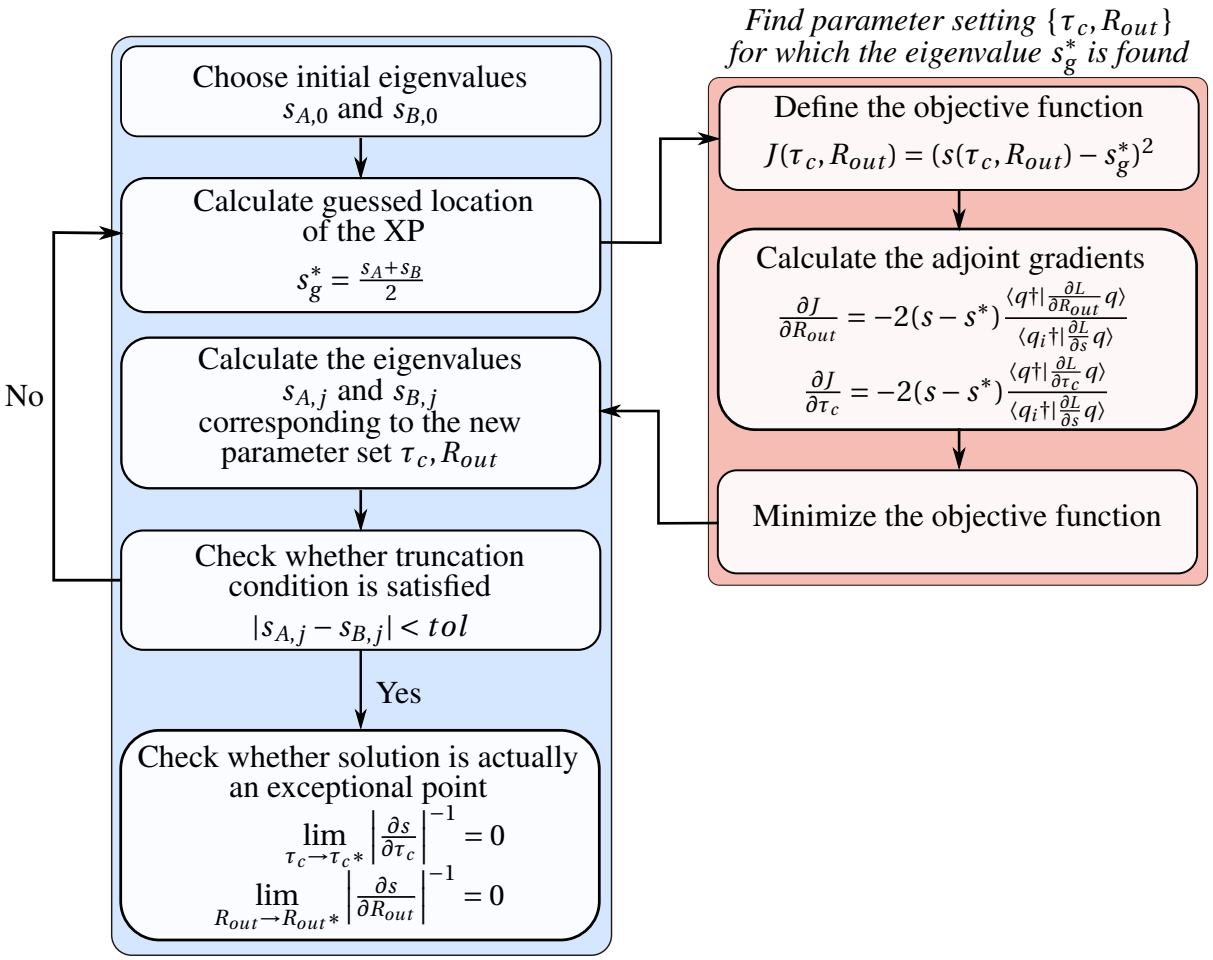

Figure 5.5: Comparison of CA, DA, and HA steps for an existing state-space network tool

These may be selected at random or by pre-analyzing the thermoacoustic system. For instance,

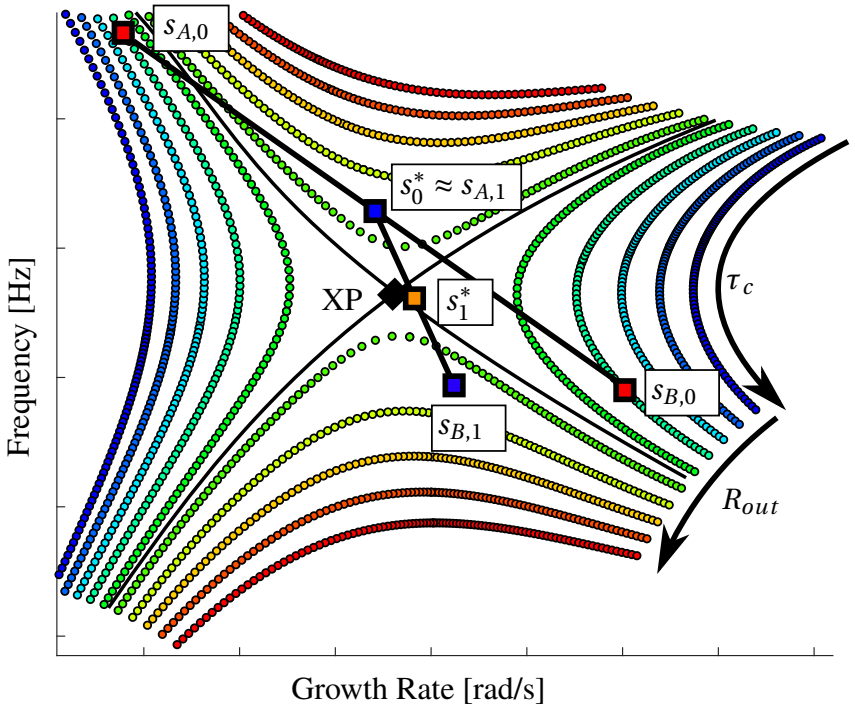

Figure 5.6: Illustration of two iterations of the outer loop: Red: Initial eigenvalues; blue: eigenvalues found in the second iteration, orange: guessed location of XP after two iterations

the probability of finding an XP for a physically realistic parameter setting increases by selecting one mode of acoustic and one of intrinsic origin. After selecting the initial eigenvalues the outer loop of the solver calculates the guessed location at the XP s_g^*, which is approximated as the arithmetic mean of $s_{A,0}$ and $s_{B,0}$. Within the inner loop, an adjoint gradient optimization routine finds the corresponding parameter setting $\{\tau_c, R_{out}\}$ for which the system has an eigenvalue at the guessed location s_g^*. The outer loop uses the found parameters to calculate the two eigenvalues closest to s_g^* and determines how close these eigenvalues are to each other. If the square of the Euclidean distance is below a pre-determined tolerance the loop is exited. In this case, the algorithm checks, whether the solution found is an XP by calculating the inverse sensibility - again using the DA formalism. This step is necessary as the solver may converge towards a semi-simple eigenvalue, which is frequently observed in rationally symmetric combustors. Failing the truncation criteria, a new guess for the estimate of the XP is calculated using the updated eigenvalues $s_{A,j}$ and $s_{B,j}$ (where j counts the iterations of the outer loop).

A graphical illustration of how the XP is approached in the outer loop is given in Fig. 5.6.

5.3.2.2 Identifying XPs based on eigenvalue sensitivity

Orchini *et al.* [64] propose a different approach to identify XPs in thermoacoustic systems. Their numerical solver uses a special feature of the XP: As a parameter ξ is changed such that the eigenvalue s approaches an XP, the eigenvalue sensitivity becomes infinite, thus its inverse

approaches zero:

$$\lim_{\xi \to \xi_{XP}} \left| \frac{\partial s}{\partial \xi} \right|^{-1} = 0. \tag{5.23}$$

The study uses the discrete adjoint to calculate the eigenvalue sensitivity (*c.f.* Sec. 3.1), which reads:

$$\frac{\delta s}{\delta \xi} = -\frac{\langle \hat{p}^\dagger | \frac{\partial L}{\partial \xi} \hat{p} \rangle}{\langle \hat{p}^\dagger | \frac{\partial L}{\partial s} \hat{p} \rangle}, \tag{5.24}$$

where $\hat{p}$ and $\hat{p}^\dagger$ represent the direct and adjoint eigenvector of pressure fluctuations, respectively, and L contains the discretized eigenvalue problem. This expression is valid for any non-defective eigenvalue, *i.e.* for all eigenvalues *except* for the XP. Given that the bi-orthogonality condition (Eq. (3.7)) no longer holds at the XP, the derivation of Eq. (5.24) as shown in [51], is not applicable at the XP. However, the expression is valid in the immediate vicinity of the XP, where the sensitivity of the eigenvalues is also extremely large.

The identification of XPs can, thus, be conducted using standard multi-parameter root-finding algorithms. However, each iteration of the iterative scheme requires the solution of an eigenvalue problem and the evaluation of Eq. (5.24). Considering that the latter requires approximately the same computational effort as the original eigenvalue problem, solving this root problem may require substantial computational resources. In addition, for the algorithm to converge towards an XP, a well-informed initial guess is required, which may be hard to identify in the first place.

5.3.2.3 Identifying XPs using perturbation theory

In another study, Orchini *et al.* [63] propose to use higher-order adjoint perturbation theory to locate XPs. The theory builds on the work of Mensah *et al.* [59] which the reader is referred to for a detailed description of the method.

The dependence of eigenvalues on a parameter ϵ can be expressed through a power series expansion which, for semi-simple eigenvalues, takes the form

$$s(\epsilon) \approx s_0 + \sum_{j=1}^{N} \epsilon^j s_j, \tag{5.25}$$

where ϵ is a perturbation parameter centered at a reference value $\epsilon_0 = 0$. The coefficients s_j are jth-order corrections and are generally given as

$$s_j = -\frac{\langle \hat{p}_0^\dagger | r_j \rangle}{\langle \hat{p}_0^\dagger | \frac{\partial L}{\partial s} \hat{p}_0 \rangle}. \tag{5.26}$$

A general expression for r_j at any order can be found in the appendix of [63] .

For eigenvalues in the vicinity of a singularity located at $\epsilon = \epsilon_{sng}$, the eigenvalue parameter dependence takes the form

$$(\epsilon - \epsilon_{sng})^k. \tag{5.27}$$

For an exceptional point, k is equal to $1/a$, where a is the algebraic multiplicity of the eigenvalue at the EP.

The values of ϵ_{sng} and the exponent k can be estimated from the coefficients s_j of a power series that is expanded close to the singularity:

$$\epsilon_{sng} = \epsilon_0 + \frac{s_j s_{j-1}}{(j+1)s_{j+1}s_{j-1} - j s_j^2}, \tag{5.28a}$$

$$k = \frac{(j^2-1)s_{j+1}s_{j-1} - (j s_j)^2}{(j+1)s_{j+1}s_{j-1} - j s_j^2}. \tag{5.28b}$$

This estimation converges to the closest singularity, with a radius of convergence defined as

$$R_c = |\epsilon_{sng} - \epsilon_0|. \tag{5.29}$$

To accurately locate an XP, an iterative scheme is proposed, following the steps

1. Evaluate the expansion coefficients s_j of an eigenvalue up to about order $N = 10$ in Eq. (5.26).
2. Estimate the closest singularity ϵ_{sng} using the results of step 1. at the highest available order (Eq. (5.28a)).
3. Evaluate the radius of convergence in Eq. (5.29). If R_c is larger than a predefined threshold, step 1. is repeated with the updated expansion point $\epsilon_0 + \epsilon_{sng} \rightarrow \epsilon_0$.

Once R_c falls below the predefined threshold, the expansion point coincides with the singular parameter, where the error scales with the magnitude of the threshold.

With this method, the singularity parameter ϵ_{sng} will, in all likelihood, be a complex number. The XP identified with the proposed method is, therefore, typically not physical but serves theoretical research purposes. Furthermore, even though the corresponding parameter setting is non-physical, the theoretical existence of an XP affects the (physical) eigenvalue trajectories in its vicinity.

5.3.2.4 Comparison of identification methods

Each of the three methods for the location of XPs is based on a different mathematical ansatz, which exploits different features of the XP. The method introduced in PAPER_XP utilizes the nature of XPs originating from two eigenvalues coalescing. The method does not require intensive preliminary analysis to determine a working initial guess: The two initial eigenvalues may even be selected at random with a high likelihood of convergence. However, the method may converge towards a semi-simple instead of a defective eigenvalue. Compared to the other two schemes, the coalescence-based algorithm may first seem inefficient, as it uses an "outer loop" where the guessed eigenvalue is updated and an "inner loop" where the objective function is minimized. However, the minimization typically requires few iterations, as the routine provides a well-informed initial guess for the optimization.

The sensitivity-based ansatz reduces the XP localization procedure to a root finding problem. However, a good initial guess for the root solver requires a-priori information about the location

of the XP, which is generally not available. As a result, finding an XP with this method requires a lot of trial and error using different values for the initial guess.

A similar problem occurs when trying to locate the XP using perturbation theory. The estimation of the parameters ϵ_{sng} and k (Eqs. (5.28)) is most accurate in close vicinity to an XP and, thus, depends on an adequate initial guess. In addition, the estimation may as well converge towards a pole singularity instead of the desired branch point singularity.

Both Schaefer *et al.* and Orchini *et al.* use the DA sensitivity to enhance the efficiency of the solver. For two tuning parameters, the calculation of the adjoint sensitivity reduces the number of resource-intensive operations in each iteration from three to two: one eigenvalue problem and one evaluation of the eigenvalue sensitivities instead of three evaluations of the eigenvalue problem. If a complex-valued parameter is selected, as it is in the perturbation-theory ansatz, the advantages of adjoint methods vanish, and the solver may use a standard finite difference scheme with a comparable resulting runtime. However, identifying realistic XPs is of great interest, especially unstable ones that not only affect the trajectories of the eigenvalues nearby but also have an impact on the dynamics of the system. The coalescence-based ansatz is the only one with which such a physically viable, unstable XP could be identified.

In summary, both the sensitivity-based and the perturbation-theory-based approaches may offer more profound insight into the stability behavior of thermoacoustic systems. With the sensitivity-based method, one can even identify realistic XPs with physical parameter settings. However, a well-informed initial guess is vital for both methods to converge. An analysis applying these methods is, therefore, recommendable for systems, where increased sensitivity or strong mode veering already indicates the existence of an XP in close vicinity. In contrast, the coalescence-based approach uses physical parameters and converges even for a random initial guess. As such, it offers the highest probability of identifying an exceptional point, even for largely unexplored models.

5.3.3 Uncertainty quantification and XPs

The identification method introduced in the previous section makes fast and reliable determination of the parameter setting associated with an XP possible. Subsequently, the respective system may be analyzed in detail, shedding light on the impact of XPs on the thermoacoustic system behavior. In PAPER_XP the identified unstable XP is analyzed to investigate its impact on the process and results of uncertainty quantification. Uncertainties arise naturally, *e.g.* from the experimental or computational determination of the FTF parameters. These parameters merely constitute the best fit to the data and are based on general model assumptions. In addition, stochastic fluctuations may cause the operational conditions to deviate from the nominal condition.

The propagation of input uncertainties to model predictions is most easily determined using Monte Carlo methods. However, depending on the complexity of the thermoacoustic model, the evaluation of the eigenvalue problem describing the thermoacoustic model may get computationally costly. As a result, Monte Carlo methods, which require numerous system evaluations to ensure convergence, can become economically impracticable. By identifying an efficient surrogate model that replicates the system response of the original system, the cost-intensive

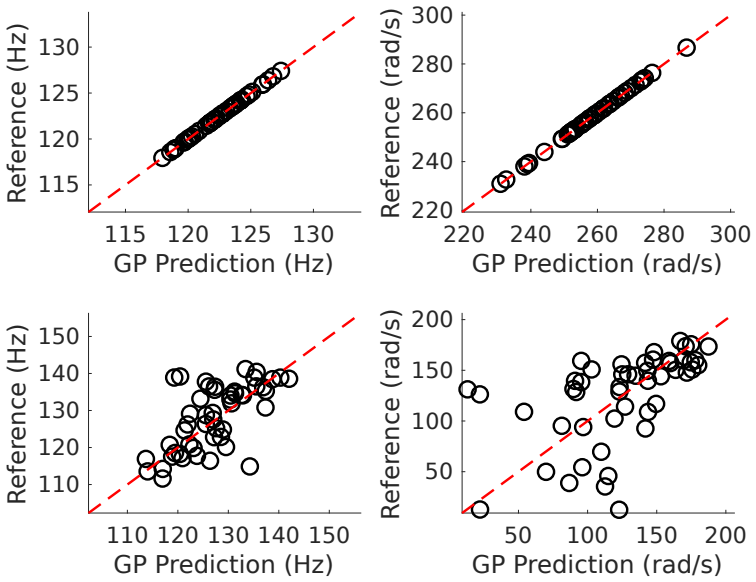

Figure 5.7: Comparison of frequency (left) and growth rate (right) predicted by the GP model vs. by the high-fidelity model at the simple eigenvalue (first row) and at the XP (second row)

evaluation of the high-fidelity model can be reduced by various orders of magnitude (*c.f.* for example [10, 26]). The study employs the machine learning method called Gaussian Process (GP) to study the potential impact of XPs on the quality of surrogate model predictions. The training and modeling framework is adopted from Guo *et al.* [27] and can be referred to therein.

Two models are trained: One at the XP and one for a simple eigenvalue that is distant from the XP. As a measure of prediction accuracy, the generalization error ϵ is evaluated based on leave-one-out cross-validation [55]. A comparison of the generalization error for increasing numbers of training samples shows that for the reference model at the simple eigenvalue, the GP model trained with 40 or more training samples accurately predicts both frequency and growth rate. In contrast, the XP surrogate model predictions do not converge towards the network model predictions, even for increased numbers of samples. A comparison of the prediction quality of the two GP models is given in Fig. 5.7. The predictions for frequency (left) and growth rate (right) of the high-fidelity model are plotted over those of the GP models. For accurate model predictions, the data points are distributed along the 45° line through the origin, which is the case for the reference GP model (first row). For the GP model at the XP, the data is widely distributed, indicating low prediction accuracy. The study finds three reasons, why the surrogate model fails at the XP:

1. The algebraic multiplicity of the XP entails two eigenvalues for each parameter setting close to the XP. The eigenvalues returned by the numeric solver can thus not be attributed to one single eigenvalue trajectory, but two. As the GP model is not able to distinguish between these two trajectories, it fails to capture the system dynamics of the high-fidelity system.

2. The growth rate and frequency functions exhibit a second-order discontinuity at the XP

which cannot be represented by the holomorphic ansatz function of the GP model.

3. The infinite sensitivity at the XP leads to large eigenvalue drifts in its immediate vicinity. As a result, the training (and testing) data contain few eigenvalues that fall within this region.

To improve the accuracy of the surrogate model predictions it is therefore advisable to

1. make sure that there is no mode switching in the training data, *i.e.* the training data represent just one eigenvalue along a single trajectory.
2. use an alternative ansatz function that is able to correctly represent a second-order discontinuity.
3. make sure that the training samples are adequately distributed not only in parameter space but also in the resulting eigenvalue space.

In PAPER_XP, the uncertainty quantification is eventually performed using standard Monte Carlo simulation. Since the underlying thermoacoustic system was of mediocre complexity, the resulting computational cost was manageable. The resulting probability density functions (PDFs) for frequency and growth rate are reproduced in Fig. 5.8. For the exceptional point, the two eigenvalues that can be found for each parameter setting are reflected in two peaks in the probability density functions of frequency and growth rate. As a result, the total variance at the exceptional point is significantly larger than the variance at the simple eigenvalue. The study concludes that exceptional points may interfere with classical methods of uncertainty quantification, as results obtained from surrogate models may be unreliable. This is especially critical because the effect of uncertainties is exacerbated in the vicinity of an exceptional point.

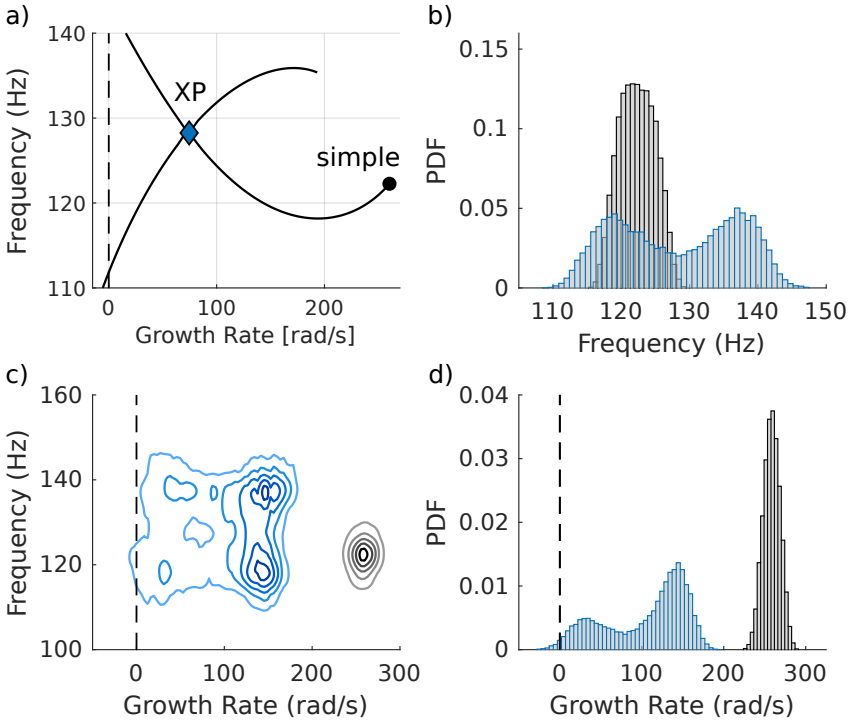

Figure 5.8: Left: Locations of the XP and the simple reference eigenvalue, below the corresponding joint PDF of frequency and growth rate. Isolines range from 10% (light) to 90% (dark) of the maximum probability density. Right: Separate PDFs of frequency and growth rate at the two eigenvalues.

5.3.4 Interplay of Clusters of Acoustic and ITA modes

The algorithm to identify XPs and the associated parameter settings was applied in PAPER_ITA. The paper analyzes the behavior of acoustic and ITA clusters in a can-annular combustor for varying parameter settings. To gain fundamental insight into the system behavior, the can-annular combustor under investigation is reduced to a Rijke tube where two-dimensional effects of the can-can communication are represented by an equivalent reflection coefficient. This ansatz, which was originally introduced in [22] is valid under specific assumptions that are discussed in detail in the original publication.

5.3.4.1 Mode interplay in a generic Rijke tube

Before studying mode interaction in the can-annular combustor model, a primary study considers a classical Rijke tube to investigate the interplay of two solitary modes of ITA and acoustic origin. A set of dimensionless numbers is introduced to obtain a generic description of the thermoacoustic model, allowing to draw general conclusions from the results. Subsequently, the interplay of ITA and acoustic eigenmodes is studied by increasing the dimensionless propagation time downstream of the flame τ_u^* for a set of fixed values of the dimensionless propagation time upstream of the flame τ_d^*.

For small values of τ_d^* and τ_u^*, *i.e.* for short upstream and downstream lengths of the Rijke tube, the acoustic and ITA modes do not interplay. As τ_u^* is increased, the ITA mode converges toward a value corresponding to a semi-anechoic system as $\lim_{\tau_d \to \infty} |R_d| \approx 0$.
A different behavior is observed for larger values of τ_u^*. Instead of converging towards an effective semi-anechoic system behavior, the ITA mode switches nature and turns into an acoustic mode, while the acoustic mode approaches the semi-anechoic eigenmode. For even larger values of τ_u^*, corresponding to a long upstream length of the Rijke tube, the presence of an exceptional point becomes evident. The trajectories of both eigenmodes exhibit strong mode veering, first converging towards each other and suddenly changing directions as they approach the XP.

5.3.4.2 Mode interplay in an annular combustor

Subsequently, the study is extended to an annular combustor model by including two-dimensional effects which are modeled by the equivalent outlet reflection coefficient. The resulting model is identical in its flame response and upstream conditions for all azimuthal modes, differing only in their total downstream propagation time. As a result, all of these modes are located on the eigenmode trajectory of varying τ_d^*.
Again, the presence of an exceptional point is found to strongly affect the shape of these trajectories, introducing strong veering. Based on these effects, the behavior of two seemingly entangled clusters of acoustic and ITA modes could be interpreted and explained. Understanding these effects potentially improves the process of engine design, allowing for small-scale adaptions whose effect can be predicted *a-priori*.

6 Model Order Reduction at the XP

In Sec. 4.1, the characteristics of the XP were introduced. In close vicinity of an XP, the system can be reduced to an effective two-dimensional system. A description of the reduction process for variations of a complex-valued parameter λ can be found in [31]. Cartarius *et al.* [9] described a different approach, where two real-valued parameters γ and ζ are changed around the XP. The parameter values at the XP are denoted γ_0 and ζ_0. According to [9], the elements of the effective, two-dimensional matrix M have the form

$$M_{i,j} = a_{i,j}^{(0)} + a_{i,j}^{(\gamma)}(\gamma - \gamma_0) + a_{i,j}^{(\zeta)}(\zeta - \zeta_0), \quad i,j \in 1,2. \tag{6.1}$$

An expansion in the eigenvalues of M gives:

$$\lambda_1 + \lambda_2 = tr(M) = c_1 + c_2(\gamma - \gamma 0) + c_3(\zeta - \zeta_0), \tag{6.2a}$$

$$\begin{aligned}(\lambda_1 - \lambda_2)^2 &= tr(M)^2 - 4det(M) \\ &= c_4 + c_5(\gamma - \gamma_0) + c_6(\zeta - \zeta_0) + c_7(\gamma - \gamma_0)^2 + c_8(\zeta - \zeta_0)^2 + c_9(\gamma - \gamma_0)(\zeta - \zeta_0).\end{aligned} \tag{6.2b}$$

Cartarius *et al.* state that eigenvalues do not change under a similarity transformation of the corresponding matrix and the explicit choice of the M is not relevant. Consequently, the representation given in Eqs. (6.2) is preferable as it introduces fewer coefficients. In fact, the determination of the model parameters requires only 6 samples, 3 for the parameters in Eq. (6.2a) and the same samples plus 3 additional ones for the parameters in Eq. (6.2b).

For the XP identified in PAPER_XP and reviewed in the previous section, a two-dimensional system is obtained for variations of the parameters τ_c and R_{out}. The resulting eigenvalue predictions show excellent agreement with the high-fidelity model (Fig. 6.1) while reducing the number of degrees of freedom from 427 to 2. The reduced model is only valid in close proximity to the XP and its accuracy decreases with increasing parameter distance to the XP $(\tau_c - \tau_c^*)$ and $(R_{out} - R_{out}^*)$. However, for a maximum variation of 10% of τ_c and R_{out} around the XP, the maximum deviation of predictions is still within 0.3% of the corresponding eigenvalue. It is, therefore, possible to exploit the $2D$ model reduction for uncertainty analysis at the XP.

In PAPER_XP the uncertainty quantification was conducted by studying the influence of uncertainties in 6 input parameters. A minor modification of Eq. (6.1) allows the introduction of N parameters ξ_k that are varied around the XP:

$$M_{i,j} = a_{i,j}^{(0)} + \sum_{k=1}^{N} a_{i,j}^{(xi_k)}(\xi_k - \xi_{k,0}), \quad i,j \in [1,2]. \tag{6.3}$$

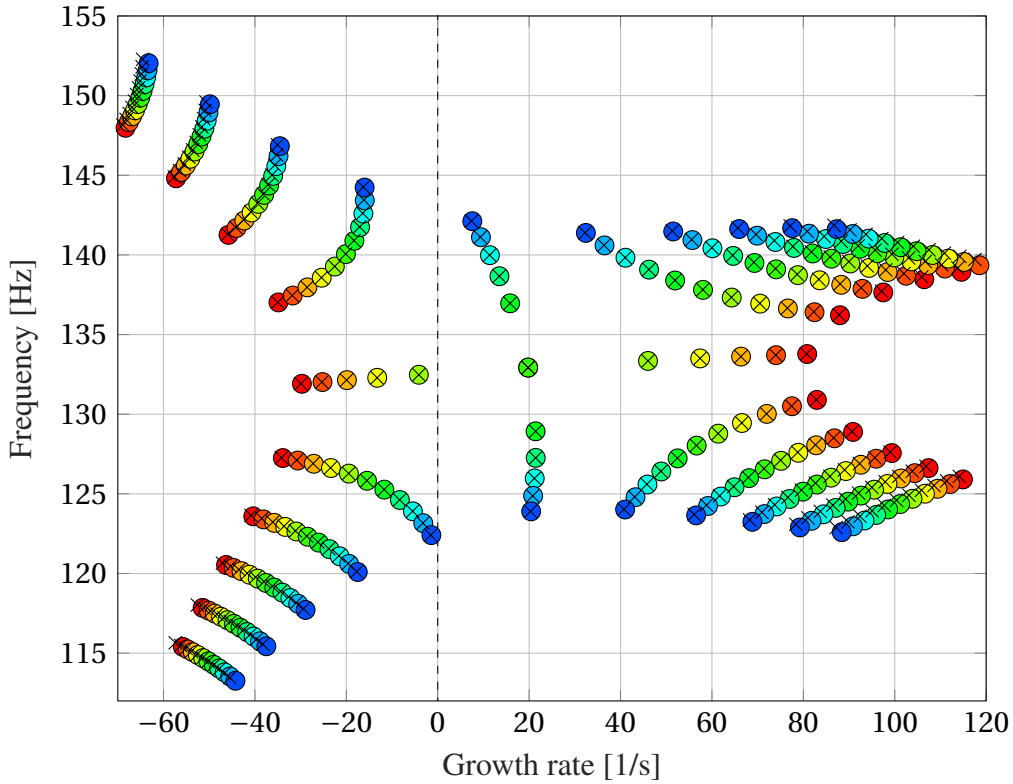

Figure 6.1: Predictions of the 2D model (round markers) vs. predictions of the high-fidelity model (cross markers).

The corresponding transformation equivalent to Eqs. (6.2) reads:

$$\lambda_1 + \lambda_2 = tr(M) = c_1 + c_k(\xi_k - \xi_{k,0}), \tag{6.4a}$$

$$\begin{aligned}(\lambda_1 - \lambda_2)^2 &= tr(M)^2 - 4det(M) \\ &= d_1 + \sum_{k=1}^{N} e_k(\xi_k - \xi_{k,0}) + f_k(\xi_k - \xi_{k,0})^2 \\ &\quad + \sum_{k=1}^{N}\sum_{m=k+1}^{N} g_{k,m}(\xi_k - \xi_{k,0})(\xi_m - \xi_{m,0}).\end{aligned} \tag{6.4b}$$

For 6 uncertain parameters, the reduced-order model introduces 35 new parameters whose determination requires the evaluation of 28 samples.

A detailed description of the selected parameters and the assumed uncertainty distributions is given in the original publication. The validation of the extended $2D$ model (Fig. 6.2), which is conducted equivalently to the surrogate model validation in PAPER_XP, shows that the 2D model accurately predicts both eigenvalues close to the XP for the specified range in uncertain parameters.

Consequently, the $2D$ model may be employed to calculate the propagation of uncertainties near the XP. Provided the existence of an XP is known *a-priori*, this may greatly reduce computational cost: Instead of evaluating the high-fidelity model for each data sample of the Monte-Carlo Simulation, the eigenvalues are determined by evaluating Eqs. (6.4a) and (6.4b). An ex-

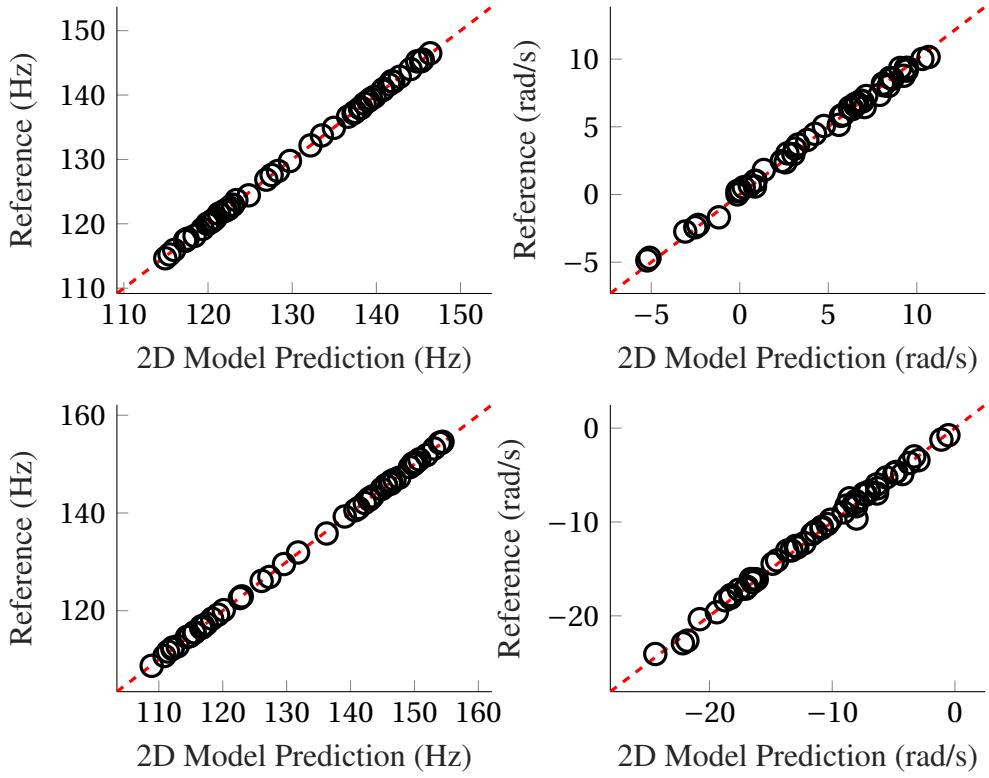

Figure 6.2: Comparison of the predictions of frequency (left) and growth rate (right) of both eigenvalues close to the XP obtained using the high-fidelity model and reduced-order model at the XP.

emplary evaluation of the probability functions of eigenvalues following this procedure shows excellent results (Fig. 6.3). Although the original, high-fidelity model was a comparably cheap low-order model, the computation time for Monte-Carlo evaluations via the $2D$ model amounts to only $\sim 1\%$ of the computation time when using the high-fidelity model.

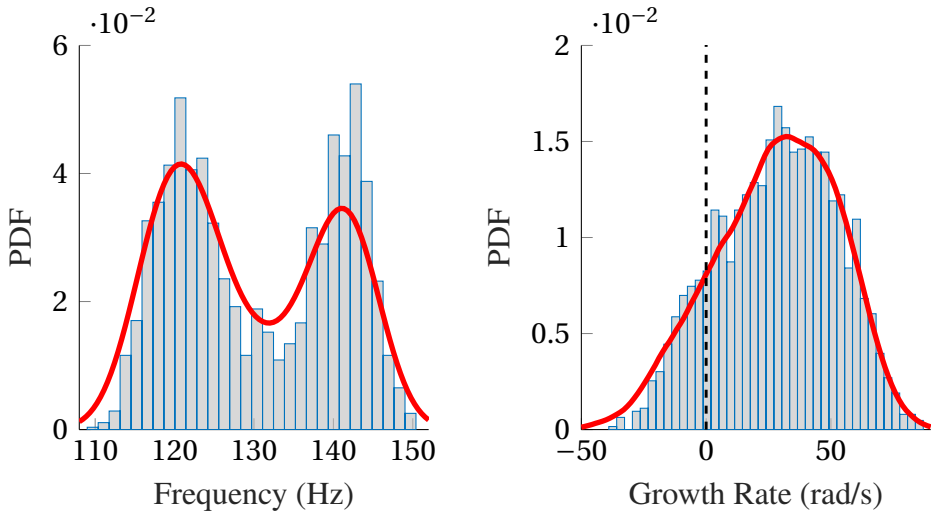

Figure 6.3: Comparison of the probability density functions of frequency (left) and growth rate (right) obtained using the high-fidelity model and reduced-order model at the XP. The red line is a kernel fit to the distribution obtained via high-fidelity calculation, the histograms are obtained via the reduced model.

7 Time-series Development at the XP

The reliable identification of XPs in thermoacoustic systems opens up new angles to analyze the system dynamics. The impact of XPs in linear stability analysis has been found to be significant. A logical next step to this analysis is the extension to the non-linear regime. In particular, the influence of XPs on the development of velocity and pressure time series merits a closer look.

The non-linear flame response is commonly modeled by means of a Flame Describing Function (FDF) [14, 61]. The FDF can be regarded as an FTF, that not only depends on the frequency but also on the amplitude of input perturbations. FDF representation of flame dynamics relies on weakly non-linear model assumptions as it ignores the effect of higher harmonics. Nevertheless, embedding an FDF in low-order network models allows the prediction of non-linear phenomena such as limit cycle oscillations and non-linear triggering [61].

In order to determine an XP for a non-linear flame model equivalently to the approach in PAPER_XP, the parameters of the flame describing function need to be parameterizable similarly to the FTF model employed for the linear analysis. A suitable model was introduced by Doehner *et al.* [12]. The study proposes a flame model which is based on the two ordinary differential equations describing two coupled mass-spring-damper oscillators with a symmetric, nonlinear damping term. The model equations read:

$$\frac{d^2x_1}{d\tau^2} = \left(\frac{1}{\delta}+2\right)u' - \alpha\frac{dx_1}{d\tau} - \beta\frac{dx_1}{d\tau}x_1^2 - x_1 + \delta(x_2 - x_1), \tag{7.1a}$$

$$\frac{d^2x_2}{d\tau^2} = -\alpha\frac{dx_2}{d\tau} - \beta\frac{dx_2}{d\tau} + \frac{2}{\zeta}(x_2 - x_1), \tag{7.1b}$$

$$\frac{q'}{d\tau} = -\frac{dx_2}{d\tau} + \frac{2}{\zeta}(x_2 - q'), \tag{7.1c}$$

where u' represents the (input) velocity perturbations at the flame base and q' the resulting heat release fluctuations. In the original study, the parameters α, β, γ, ζ are determined by finding the best fit of the flame model to time series data stemming from high-fidelity CFD simulations.

In order to investigate the impact of XPs on non-linear dynamics, a suitable thermoacoustic model has to be found. The requirements for the model can be summarized as follows:

- There should be no unstable eigenvalues, other than those associated with the XP: If there are other unstable modes, these may significantly alter the dynamics of the system, thus the effects of the XP cannot be identified beyond doubt.
- The growth rate of the XP should be close to zero: For highly stable systems, oscillations are immediately damped. For highly unstable systems the dynamics develop very fast and making it hard to discern particular effects.

A suitable configuration is found by employing the method introduced in PAPER_XP for the equivalent linear system ($\beta = 0$) and tuning the model and flame parameters. The values of the flame parameters are of the same order as those identified in Doehner *et al.*.

The resulting FDF is shown in Fig. 7.1.

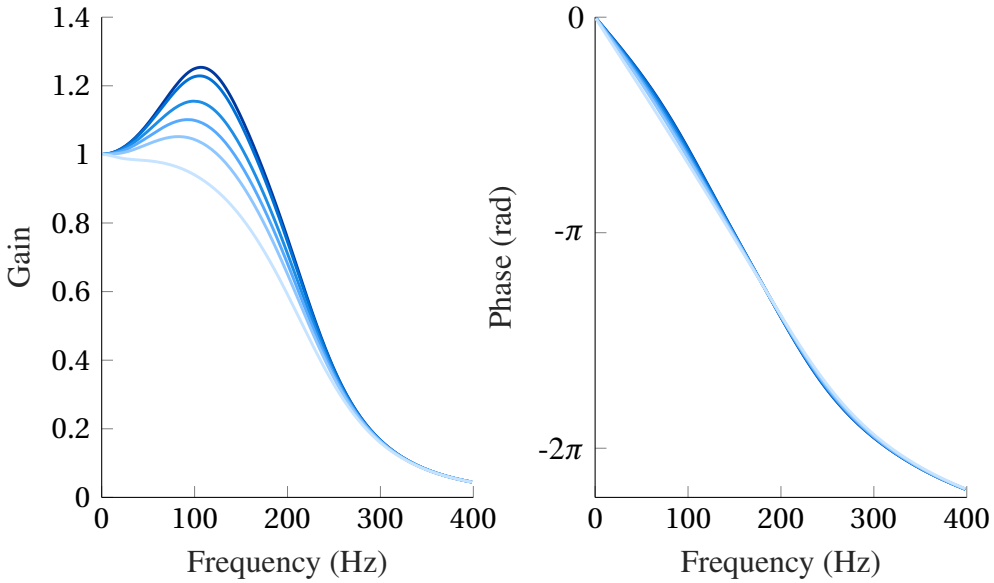

Figure 7.1: Gain (left) and phase (right) of the flame describing function obtained with the Non-Linear Double Oscillator. Lighter shades of blue indicate increasing forcing amplitudes.

Subsequently, the time series of the non-linear model is analyzed by numerically solving the state space model. Due to the presence of two eigenvalues that are close to each other, the velocity perturbations leading up to the limit cycle show an interference pattern between two frequencies, also known as beating (Fig. 7.2).

The spectrum of the velocity perturbation time series shows that, once the limit cycle is reached, one frequency dominates. On the contrary, for the oscillations leading up to the limit cycle, the two frequencies associated with the limit cycle are equally pronounced in the frequency spectrum.

Although the XP has an impact on the time series leading up to the limit cycle, the limit cycle behavior in the vicinity of an XP does not show any anomaly.

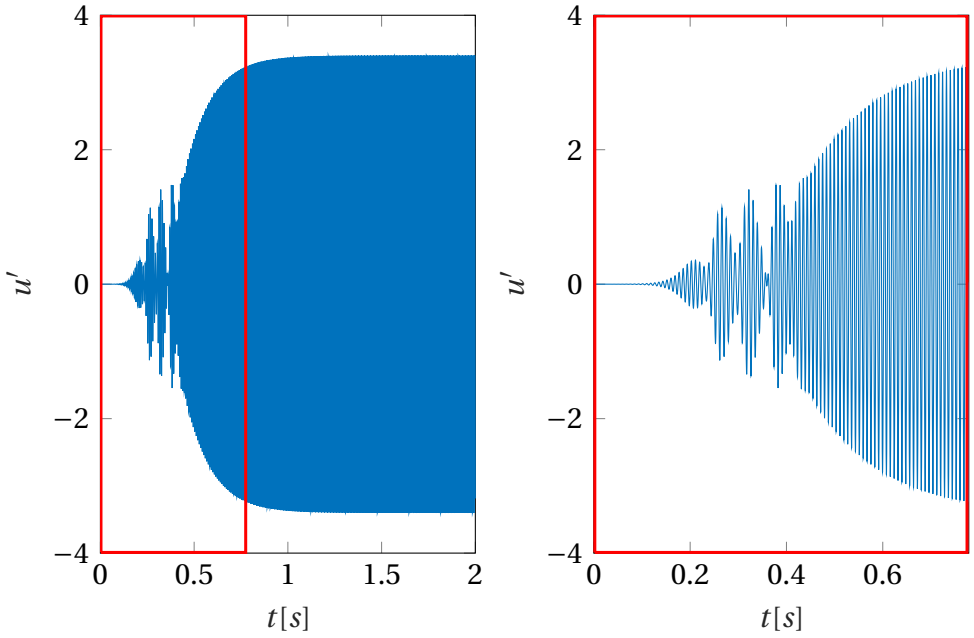

Figure 7.2: Time series of velocity perturbations. Left: Entire time series. Right: Time series before LC is reached.

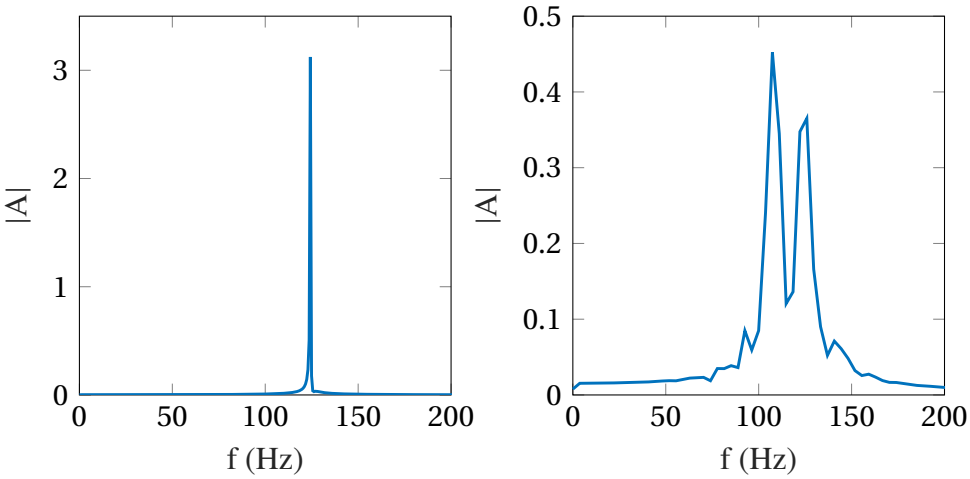

Figure 7.3: Frequency spectrum of the velocity signal at the LC (left) and leading up to the LC (right)

8 Summary of Papers

This chapter lists and summarizes the publications connected to the thesis. Furthermore, the respective contribution of the authors to each paper is laid out. Note that the arrangement of publications does not follow a chronological order, but instead emphasizes the advancements in methodology.

8.1 Low-order Network Model of a Duct with Non-Uniform Cross-Section and Varying Mean Temperature in the Presence of Mean Flow

The element equations and implementation strategy for a duct element, which models both temperature and cross-section area changes along its longitudinal axis, are laid out (see Sec. 5.1). The extended network tool is validated against analytical results.

Original Abstract: Stability analysis of thermoacoustic systems is often carried out with low-order network models. This paper introduces a method to include a duct element with varying cross-sectional area and an arbitrary mean temperature profile in a thermoacoustic network model. Based on the quasi-one-dimensional form of the linearized Euler equations (LEEs) for a perfect, inviscid gas, the system equations are formulated in a state-space framework in terms of the Riemann invariants f and g. This approach is predicated on one additional assumption, i.e. that the direct impact of entropy fluctuations on the acoustic waves inside the duct is small. A comparison of model results with analytical analysis shows excellent agreement. Eigenvalues are predicted with good accuracy, even for coarse grids. Furthermore, the mode shapes and frequency responses match those found in the literature, demonstrating the validity of the approach.

Contribution according to Contributor Role Taxonomy scheme (CRediT):

Contribution	Author
Conceptualization	F. Schaefer, W. Polifke
Methodology	F. Schaefer
Software	F. Schaefer
Validation	F. Schaefer, W. Polifke
Formal analysis	F. Schaefer
Data Curation	F. Schaefer
Writing - Original Draft	F. Schaefer
Writing - Review Editing	F. Schaefer, W. Polifke
Visualization	F. Schaefer
Supervision	W. Polifke

Status: Published in the Proceedings of the *AIAA Propulsion and Energy Forum*.

Review Process: Extended abstract peer-reviewed, Scopus-listed.

Reference: F. Schaefer and W. Polifke. Low-order network modeling of a duct with non-uniform cross-section and arbitrary mean temperature gradient in the presence of mean flow. In *AIAA Propulsion and Energy Forum*, AIAA 2019-4376, page 5, Indianapolis, Indiana, USA, 2019. doi: 10.2514/6.2019-4376.

8.2 A Hybrid Adjoint Network Model for Thermoacoustic Optimization

A novel approach to calculate the adjoint system corresponding to a direct network model is introduced (see Sec. 5.2). It combines the advantages of the flexible and straightforward DA approach with the resourcefulness and superior interpretability of the CA approach.

Original Abstract: Exceptional points can be found for specific sets of parameters in thermoacoustic systems. At an exceptional point, two eigenvalues and their corresponding eigenfunctions coalesce. Given that the sensitivity of these eigenvalues to parameter changes becomes infinite at the exceptional point, their occurrence may greatly affect the outcome and reliability of numerical stability analysis. We propose a new method to identify exceptional points in thermoacoustic systems. By iteratively updating the system parameters, two initially selected eigenvalues are shifted towards each other, ultimately colliding and generating the exceptional point. Using this algorithm, we were able to identify for the first time a physically meaningful exceptional point with positive growth rate in a thermoacoustic model. Furthermore, our analysis goes beyond previous studies inasmuch as we employ a more realistic flame transfer function to model flame dynamics. Building on these results, we analyze the effect of exceptional points on the reliability of thermoacoustic stability analysis. In the context of uncertainty quantification, we show that surrogate modeling is not reliable in the vicinity of an exceptional point, even when large sets of training samples are provided. The impact of exceptional points on the propagation of input uncertainties is demonstrated via Monte Carlo computations. The increased sensitivity associated with the exceptional point results in large variances for eigenvalue predictions, which needs to be taken into account for reliable stability analysis.

Contribution according to Contributor Role Taxonomy scheme (CRediT):

Contribution	Author
Conceptualization	F. Schaefer
Methodology	F. Schaefer
Software	F. Schaefer
Validation	F. Schaefer
Formal analysis	F. Schaefer
Data Curation	F. Schaefer
Writing - Original Draft	F. Schaefer
Writing - Review Editing	F. Schaefer, L. Magri, W. Polifke
Visualization	F. Schaefer
Supervision	W. Polifke

Status Published in *Journal of Engineering for Gas Turbines and Power*.

Review Process: Peer-reviewed, Scopus-listed.

Reference: Schaefer, F., Magri, L., and Polifke, W. (January 3, 2022). "A Hybrid Adjoint Network Model for Thermoacoustic Optimization." ASME. *J. Eng. Gas Turbines Power*. March 2022; 144(3): 031017. https://doi.org/10.1115/1.4051959

8.3 The Impact of Exceptional Points on the Reliability of Thermoacoustic Stability Analysis

Adjoint design is employed to enable efficient identification of XPs in thermoacoustic systems. As a novelty, an unstable XP could be located for a physical parameter setting and a realistic flame model. Subsequent analysis reveals that the quality of surrogate models and the reliability of network predictions are significantly impaired in close vicinity of XPs (Sec. 5.3).

Original Abstract: Exceptional points can be found for specific sets of parameters in thermoacoustic systems. At an exceptional point, two eigenvalues and their corresponding eigenfunctions coalesce. Given that the sensitivity of these eigenvalues to parameter changes becomes infinite at the exceptional point, their occurrence may greatly affect the outcome and reliability of numerical stability analysis. We propose a new method to identify exceptional points in thermoacoustic systems. By iteratively updating the system parameters, two initially selected eigenvalues are shifted towards each other, ultimately colliding and generating the exceptional point. Using this algorithm, we were able to identify for the first time a physically meaningful exceptional point with positive growth rate in a thermoacoustic model. Furthermore, our analysis goes beyond previous studies inasmuch as we employ a more realistic flame transfer function to model flame dynamics. Building on these results, we analyze the effect of exceptional points on the reliability of thermoacoustic stability analysis. In the context of uncertainty quantification, we show that surrogate modeling is not reliable in the vicinity of an exceptional point, even when large sets of training samples are provided. The impact of exceptional points on the propagation of input uncertainties is demonstrated via Monte Carlo computations. The increased sensitivity associated with the exceptional point results in large variances for eigenvalue predictions, which needs to be taken into account for reliable stability analysis.

Contribution according to Contributor Role Taxonomy scheme (CRediT):

Contribution	Author
Conceptualization	F. Schaefer, W. Polifke
Methodology	F. Schaefer
Software	F. Schaefer, S. Guo
Validation	F. Schaefer
Formal analysis	F. Schaefer
Data Curation	F. Schaefer
Writing - Original Draft	F. Schaefer
Writing - Review Editing	F. Schaefer, S. Guo, W. Polifke
Visualization	F. Schaefer, S. Guo
Supervision	W. Polifke

Status: Published in *Journal of Engineering for Gas Turbines and Power*.

Review Process: Peer-reviewed, Scopus-listed.

Reference: Schaefer, F., Guo, S., and Polifke, W. (January 18, 2021). "The Impact of Exceptional Points on the Reliability of Thermoacoustic Stability Analysis." ASME. *J. Eng. Gas Turbines Power*. February 2021; 143(2): 021010. https://doi.org/10.1115/1.4049351

8.4 Interplay of Clusters of Acoustic and Intrinsic Thermoacoustic Modes in Can-Annular Combustors

The interplay of clusters containing multiple intrinsic thermoacoustic modes is studied. Exceptional points, which are identified using the algorithm introduced in Sec. 5.3.2, are found to strongly influence the nature and trajectories of thermoacoustic modes.

Original Abstract: Thermoacoustic systems can exhibit self-excited instabilities of two natures, namely cavity modes or intrinsic thermoacoustic (ITA) modes. In heavy-duty land-based gas turbines with can-annular combustors, the cross-talk between cans causes the cavity modes of various azimuthal order to create clusters, i.e., ensembles of modes with close frequencies. Similarly, in systems exhibiting rotational symmetry, ITA modes also have the peculiar behavior of forming clusters. In the present study, we investigate how such clusters interplay when they are located in the same frequency range. We first consider a simple Rijke tube configuration and derive a general analytical low-order network model using only dimensionless numbers. We investigate the trajectories of the eigenmodes when changing the downstream length and the flame position. In particular, we show that ITA and acoustic modes can switch nature and their trajectories are strongly influenced by the presence of exceptional points. We then study a generic can-annular combustor. We show that such configuration can be approximated by an equivalent Rijke tube. We demonstrate that, in the absence of mean flow, the eigenvalues of the system necessarily lie on specific trajectories imposed by the upstream conditions.

Contribution according to Contributor Role Taxonomy scheme (CRediT):

Contribution	Author
Conceptualization	G. J. J. Fournier, M. Haeringer, C. F. Silva, W. Polifke
Methodology	G. J. J. Fournier, M. Haeringer
Software	G. J. J. Fournier, F. Schaefer
Validation	G. J. J. Fournier
Formal analysis	G. J. J. Fournier
Data Curation	G. J. J. Fournier
Writing - Original Draft	G. J. J. Fournier
Writing - Review Editing	G. J. J. Fournier, F. Schaefer, M. Haeringer, C. F. Silva, W. Polifke
Visualization	G. J. J. Fournier
Supervision	C. F. Silva, W. Polifke

Status: Published in *Journal of Engineering for Gas Turbines and Power*.

Review Process: Peer-reviewed, Scopus-listed.

Reference: Fournier, G. J. J., Schaefer, F., Haeringer, M., Silva, C. F., and Polifke, W. (October 14, 2022). "Interplay of Clusters of Acoustic and Intrinsic Thermoacoustic Modes in Can-Annular Combustors." ASME. *J. Eng. Gas Turbines Power*. December 2022; 144(12): 121015.

9 Conclusion and Outlook

The integration of adjoint methods into established network model frameworks contributes to a better understanding and more efficient control of thermoacoustic instability phenomena.

The present thesis shows how adjoint methods may be implemented into an existing framework without applying major changes to the base software. Adjoint functionalities, like displaying the adjoint eigenmodes or calculating the eigenvalue shift, can be used to the full extent by adding just one additional script to the software. Within this script, the scattering matrices of the compact elements are calculated according to the derivations presented in this thesis. This "hybrid adjoint" way thus utilizes the derivations and implementation of the original software, making it far less error-prone and time-consuming than the classical "continuous adjoint", which it is based on. The adjoint variables and sensitivities give additional insight into the physics of thermoacoustic systems. Moreover, the calculation of the eigenvalue sensitivity with respect to all variables enables the implementation of systematic optimization strategies with decreased computational effort and improved gradient accuracy compared to conventional procedures.

Consequently, future research may use the accurate calculation of the eigenmodes to study fundamental effects due to external feedback mechanisms or internal parametric settings on the thermoacoustic system. Furthermore, next to helping control thermoacoustic instability, the adjoint sensitivity may be used to (i) further optimize thermoacoustic systems regarding their dynamical behavior, (ii) find efficient ways to assess the uncertainty of a system or (iii) enhance the training process of data-driven models including deep neural networks.

The thesis further shows how adjoints may be applied to locate realistic parameter settings associated with exceptional points. Based on the presented algorithm, it was found that

1. unstable exceptional points can be found in thermoacoustic systems for realistic parameter settings,

2. exceptional points greatly affect the reliability of stability predictions,

3. classical surrogate models may not be able to represent the model behavior in the vicinity of an XP, and

4. strong mode veering associated with an XP plays a decisive role in explaining the behavior of seemingly entangled ITA and acoustic clusters.

In order to efficiently study uncertainty propagation at an XP, this thesis proposes an alternative ansatz to classical surrogate modeling. By reducing the model to an effective $2x2$ system, uncertainty prediction via Monte Carlo simulation can be significantly reduced. This is possible, as the dynamics at an XP are determined solely by the two eigenvalues coalescing at the XP.

Furthermore, the linear analysis of XPs is extended to a non-linear analysis, using a parametric flame describing function.

The proposed algorithm of XP identification facilitates further analysis of exceptional points which, for instance, may be directed at studying dynamical parametric encircling of XPs, similar to what has been presented in [13]. This will provide fundamental insight into the dynamics of thermoacoustic systems.
Furthermore, the analysis of XPs by means of adjoint network models may help to further improve the fundamental understanding of XPs in order to exploit the unusual physical behavior for the optimization of thermoacoustic combustor design.

Bibliography

[1] J. G. Aguilar, L. Magri, and M. P. Juniper. Adjoint-based sensitivity analysis of low-order thermoacoustic networks using a wave-based approach. *Journal of Computational Physics*, 341:163–181, July 2017. ISSN 0021-9991. doi: 10.1016/j.jcp.2017.04.013.

[2] A. Albayrak and W. Polifke. Propagation Velocity of Inertial Waves in Cylindrical Swirling Flow. In *23nd Int. Congress on Sound and Vibration (ICSV23)*, Athens, Greece, 2016. IIAV.

[3] M. Bauerheim, J.-F. Parmentier, P. Salas, F. Nicoud, and T. Poinsot. An analytical model for azimuthal thermoacoustic modes in an annular chamber fed by an annular plenum. *Combustion and Flame*, 161(5):1374–1389, May 2014. ISSN 0010-2180. doi: 10.1016/j.combustflame.2013.11.014.

[4] T. R. Bewley. Flow control: New challenges for a new Renaissance. *Progress in Aerospace Sciences*, 37(1):21–58, Jan. 2001. ISSN 03760421. doi: 10.1016/S0376-0421(00)00016-6.

[5] C. Bourquard and N. Noiray. Stabilization of acoustic modes using Helmholtz and Quarter-Wave resonators tuned at exceptional points. *Journal of Sound and Vibration*, 445:288–307, Apr. 2019. ISSN 0022-460X. doi: 10.1016/j.jsv.2018.12.011.

[6] P. E. Buschmann, G. A. Mensah, and J. P. Moeck. Intrinsic thermoacoustic modes in an annular combustion chamber. *Combustion and Flame*, 214:251–262, Apr. 2020. ISSN 00102180. doi: 10.1016/j.combustflame.2019.11.006.

[7] F. Caeiro, C. Sovardi, K. Förner, and W. Polifke. Shape Optimization of a Helmholtz Resonator using an Adjoint Method. *Int. J. Spray Combust. Dyn.*, 9(4):394–408, 2017. doi: 10.1177/1756827717703576.

[8] G. Campa and M. P. Juniper. Obtaining bifurcation diagrams with a thermoacoustic network model. In *ASME Turbo Expo 2012: Turbine Technical Conference and Exposition*, pages 167–177. American Society of Mechanical Engineers, 2012.

[9] H. Cartarius, J. Main, and G. Wunner. Exceptional points in the spectra of atoms in external fields. *Phys. Rev. A*, 79(5):053408, May 2009. ISSN 1050-2947, 1094-1622. doi: 10.1103/PhysRevA.79.053408.

[10] P. Chattopadhyay, S. Mondal, C. Bhattacharya, A. Mukhopadhyay, and A. Ray. Dynamic Data-Driven Design of Lean Premixed Combustors for Thermoacoustically Stable Operations. *J. Mech. Des*, 139(11):111419–111419–10, Oct. 2017. ISSN 1050-0472. doi: 10.1115/1.4037307.

[11] L. Crocco. Research on combustion instability in liquid propellant rockets. *Symposium (International) on Combustion*, 12:85–99, 1969.

[12] G. Doehner, M. Haeringer, and C. F. Silva. Nonlinear flame response modelling by a parsimonious set of ordinary differential equations. *International Journal of Spray and Combustion Dynamics*, 14(1-2):17–29, May 2022. ISSN 1756-8277, 1756-8285. doi: 10.1177/17568277221094760.

[13] J. Doppler, A. A. Mailybaev, J. Böhm, U. Kuhl, A. Girschik, F. Libisch, T. J. Milburn, P. Rabl, N. Moiseyev, and S. Rotter. Dynamically encircling an exceptional point for asymmetric mode switching. *Nature*, 537(7618):76–79, Sept. 2016. ISSN 0028-0836, 1476-4687. doi: 10.1038/nature18605.

[14] A. P. Dowling and S. R. Stow. Acoustic Analysis of Gas Turbine Combustors. *Journal of Propulsion and Power*, 19(5):751–764, Sept. 2003. ISSN 0748-4658. doi: 10.2514/2.6192.

[15] T. Emmert. *State Space Modeling of Thermoacoustic Systems with Application to Intrinsic Feedback*. PhD thesis, TU München, München, Germany, 2016.

[16] T. Emmert, S. Jaensch, C. Sovardi, and W. Polifke. taX - a Flexible Tool for Low-Order Duct Acoustic Simulation in Time and Frequency Domain. In *7th Forum Acusticum*, Krakow, Sept. 2014. DEGA.

[17] T. Emmert, S. Bomberg, and W. Polifke. Intrinsic Thermoacoustic Instability of Premixed Flames. *Combustion and Flame*, 162(1):75–85, Jan. 2015. ISSN 00102180. doi: 10.1016/j.combustflame.2014.06.008.

[18] T. Emmert, M. Meindl, S. Jaensch, and W. Polifke. Linear State Space Interconnect Modeling of Acoustic Systems. *Acta Acustica united with Acustica*, 102(5):824–833, Sept. 2016. ISSN 16101928. doi: 10.3813/AAA.918997.

[19] R. M. Errico. What Is an Adjoint Model? *Bull. Amer. Meteor. Soc.*, 78(11):2577–2591, Nov. 1997. ISSN 0003-0007, 1520-0477. doi: 10.1175/1520-0477(1997)078<2577:WIAAM>2.0.CO;2.

[20] S. Evesque, W. Polifke, and C. Pankiewitz. Spinning and Azimuthally Standing Acoustic Modes in Annular Combustors. In *9th AIAA/CEAS Aeroacoustics Conf.*, AIAA 2003-3182, Hilton Head, S.C., U.S.A., 2003. doi: 10.2514/6.2003-3182.

[21] G. J. J. Fournier. taX Tutorial, 2022.

[22] G. J. J. Fournier, M. Haeringer, C. F. Silva, and W. Polifke. Low-Order Modeling to Investigate Clusters of Intrinsic Thermoacoustic Modes in Annular Combustors. *Journal of Engineering for Gas Turbines and Power*, 143(4):041025, Apr. 2021. ISSN 0742-4795, 1528-8919. doi: 10.1115/1.4049356.

[23] G. J. J. Fournier, F. Schaefer, M. Haeringer, C. F. Silva, and W. Polifke. Interplay of Clusters of Acoustic and Intrinsic Thermoacoustic Modes in Can-Annular Combustors. *Journal of Engineering for Gas Turbines and Power*, 144(12):121015, Dec. 2022. ISSN 0742-4795, 1528-8919. doi: 10.1115/1.4055381.

[24] A. Ghani and W. Polifke. An exceptional point switches stability of a thermoacoustic experiment. *Journal of Fluid Mechanics*, 920:R3, Aug. 2021. ISSN 0022-1120, 1469-7645. doi: 10.1017/jfm.2021.480.

[25] M. B. Giles and N. A. Pierce. An introduction to the adjoint approach to design. *Flow, turbulence and combustion*, 65(3-4):393–415, 2000.

[26] S. Guo, C. F. Silva, A. Ghani, and W. Polifke. Quantification and Propagation of Uncertainties in Identification of Flame Impulse Response for Thermoacoustic Stability Analysis. *J. Eng. Gas Turbines Power*, 141(2):021032–10, Feb. 2019. ISSN 0742-4795. doi: 10.1115/1.4041652.

[27] S. Guo, C. F. Silva, and W. Polifke. Efficient Robust Design for Thermoacoustic Instability Analysis: A Gaussian Process Approach. *Journal of Engineering for Gas Turbines and Power*, 142(3):031026, Mar. 2020. ISSN 0742-4795, 1528-8919. doi: 10.1115/1.4044197.

[28] S. Güttel and F. Tisseur. The nonlinear eigenvalue problem. *Acta Numerica*, 26:1–94, May 2017. ISSN 0962-4929, 1474-0508. doi: 10.1017/S0962492917000034.

[29] M. Haeringer and W. Polifke. Time Domain Bloch Boundary Conditions for Efficient Simulation of Thermoacoustic Limit-Cycles in (Can-)Annular Combustors. *J. Eng. Gas Turbines Power*, 141(12):121005, 2019. doi: 10.1115/1.4044869.

[30] K. Hartz, T. Lenck, S. Mueller, P. Godron, M. Zackariat, F. Heilmann, F. Hein, J. Metz, J. Hoppe, A. Kraus, J. Steitz, U. Weiss, S. Wieland, B. Saerbeck, M. Holl, A. Graf, and U. Maier. Agora Energiewende (2023): Die Energiewende in Deutschland: Stand der Dinge 2022. Rückblick auf die wesentlichen Entwicklungen sowie Ausblick auf 2023. Technical report, Agora Energiewende, 2022.

[31] W. Heiss and H. Harney. The chirality of exceptional points. *The European Physical Journal D*, 17(2):149–151, Nov. 2001. ISSN 14346060. doi: 10.1007/s100530170017.

[32] W. D. Heiss. Exceptional points of non-Hermitian operators. *J. Phys. A: Math. Gen.*, 37 (6):2455–2464, Feb. 2004. ISSN 0305-4470, 1361-6447. doi: 10.1088/0305-4470/37/6/034.

[33] W. D. Heiss. The physics of exceptional points. *Journal of Physics A: Mathematical and Theoretical*, 45(44):444016, Nov. 2012. ISSN 1751-8113, 1751-8121. doi: 10.1088/1751-8113/45/44/444016.

[34] D. Hill. A theoretical approach for analyzing the restabilization of wakes. In *30th Aerospace Sciences Meeting and Exhibit*, Reno,NV,U.S.A., Jan. 1992. American Institute of Aeronautics and Astronautics. doi: 10.2514/6.1992-67.

[35] N. Hosseini, V. Kornilov, I. Lopez Arteaga, W. Polifke, O. Teerling, and L. de Goey. Intrinsic thermoacoustic modes and their interplay with acoustic modes in a Rijke burner. *International Journal of Spray and Combustion Dynamics*, 10(4):315–325, Dec. 2018. ISSN 1756-8277, 1756-8285. doi: 10.1177/1756827718782884.

[36] https://gitlab.lrz.de/tfd/tax. taX Network Model Tool. Technical University Munich, 2014.

[37] M. P. Juniper. Transient growth and triggering in the horizontal Rijke tube. *Int. J. Spray Combust. Dynamics*, 3(3):109–224, 2011. doi: 10.1260/1756-8277.3.3.209.

[38] M. P. Juniper. Sensitivity analysis of thermoacoustic instability with adjoint Helmholtz solvers. *Phys. Rev. Fluids*, 3(11):110509, Nov. 2018. doi: 10.1103/PhysRevFluids.3.110509.

[39] M. P. Juniper and R. I. Sujith. Sensitivity and Nonlinearity of Thermoacoustic Oscillations. *Annual Review of Fluid Mechanics*, 50(1):661–689, Jan. 2018. ISSN 0066-4189, 1545-4479. doi: 10.1146/annurev-fluid-122316-045125.

[40] T. Kato and Springer-Verlag (Berlin). *Perturbation Theory for Linear Operators*. Springer, Berlin, 2005. ISBN 978-3-540-58661-6 978-3-642-66282-9.

[41] T. Komarek and W. Polifke. Impact of Swirl Fluctuations on the Flame Response of a Perfectly Premixed Swirl Burner. *Engineering for Gas Turbines and Power*, 132(6): 061503, June 2010. doi: 10.1115/1.4000127.

[42] C. Laurent, M. Bauerheim, T. Poinsot, and F. Nicoud. A novel modal expansion method for low-order modeling of thermoacoustic instabilities in complex geometries. *Combustion and Flame*, 206:334–348, Aug. 2019. ISSN 0010-2180. doi: 10.1016/j.combustflame.2019.05.010.

[43] J. Li and A. S. Morgans. The one-dimensional acoustic field in a duct with arbitrary mean axial temperature gradient and mean flow. *Journal of Sound and Vibration*, 400:248–269, July 2017. ISSN 0022-460X. doi: 10.1016/j.jsv.2017.03.047.

[44] J. Li, Y. Xia, A. S. Morgans, and X. Han. Numerical prediction of combustion instability limit cycle oscillations for a combustor with a long flame. *Combustion and Flame*, 185: 28–43, Nov. 2017. ISSN 0010-2180. doi: 10.1016/j.combustflame.2017.06.018.

[45] J. Li, D. Yang, C. Luzzato, and A. Morgans. Open source combustion instability low order simulator (OSCILOS). Technical Report, Imperial College London, 2017.

[46] P. Luchini and A. Bottaro. Adjoint Equations in Stability Analysis. *Annual Review of Fluid Mechanics*, 46(1):493–517, 2014. doi: 10.1146/annurev-fluid-010313-141253.

[47] M. A. Macquisten, M. Whiteman, S. R. Stow, and A. J. Moran. Exploitation of Measured Flame Transfer Functions for a Two-Phase Lean Fuel Injector to Predict Thermoacoustic Modes in Full Annular Combustors. In *Volume 4A: Combustion, Fuels and Emissions*, page V04AT04A003, Düsseldorf, Germany, June 2014. American Society of Mechanical Engineers. ISBN 978-0-7918-4568-4. doi: 10.1115/GT2014-25036.

[48] L. Magri. *Adjoint Methods in Thermo-Acoustic and Combustion Instability*. PhD thesis, University of Cambridge, 2015.

[49] L. Magri. Adjoint methods as design tools in thermoacoustics. *Appl. Mech. Rev*, Feb. 2019. ISSN 0003-6900. doi: 10.1115/1.4042821.

[50] L. Magri and M. Juniper. Adjoint-based linear analysis in reduced order thermo-acoustic models. *Int. J. Spray Combust. Dynamics*, 6(3):225–246, 2014.

[51] L. Magri and M. P. Juniper. Sensitivity analysis of a time-delayed thermo-acoustic system via an adjoint-based approach. *Journal of Fluid Mechanics*, 719:183–202, Mar. 2013. ISSN 1469-7645. doi: 10.1017/jfm.2012.639.

[52] L. Magri and M. P. Juniper. A Theoretical Approach for Passive Control of Thermoacoustic Oscillations: Application to Ducted Flames. *Journal of Engineering for Gas Turbines and Power*, 135(9):091604, Sept. 2013. ISSN 0742-4795, 1528-8919. doi: 10.1115/1.4024957.

[53] L. Magri and M. P. Juniper. Global modes, receptivity, and sensitivity analysis of diffusion flames coupled with duct acoustics. *Journal of Fluid Mechanics*, 752:237–265, Aug. 2014. doi: 10.1017/jfm.2014.328.

[54] L. Magri, M. Bauerheim, and M. P. Juniper. Stability analysis of thermo-acoustic nonlinear eigenproblems in annular combustors. Part I. Sensitivity. *Journal of Computational Physics*, 325:395–410, Nov. 2016. ISSN 0021-9991. doi: 10.1016/j.jcp.2016.07.032.

[55] Marelli Stefano and Sudret Bruno. UQLab: A Framework for Uncertainty Quantification in Matlab. *Vulnerability, Uncertainty, and Risk*, pages 2554–2563, 2014. ISSN 9780784413609. doi: 10.1061/9780784413609.257.

[56] G. A. Mensah and J. P. Moeck. Acoustic Damper Placement and Tuning for Annular Combustors: An Adjoint-Based Optimization Study. *Journal of Engineering for Gas Turbines and Power*, 139(6):061501, June 2017. ISSN 0742-4795, 1528-8919. doi: 10.1115/1.4035201.

[57] G. A. Mensah, L. Magri, and J. P. Moeck. Methods for the Calculation of Thermoacoustic Stability Margins and Monte Carlo-Free Uncertainty Quantification. In *Proceedings of ASME Turbo Expo 2017: Turbomachinery Technical Conference and Exposition*, Charlotte, NC, USA, June 2017. American Society of Mechanical Engineers Digital Collection. doi: 10.1115/GT2017-64829.

[58] G. A. Mensah, L. Magri, C. F. Silva, P. E. Buschmann, and J. P. Moeck. Exceptional points in the thermoacoustic spectrum. *Journal of Sound and Vibration*, 433:124–128, Oct. 2018. ISSN 0022-460X. doi: 10.1016/j.jsv.2018.06.069.

[59] G. A. Mensah, A. Orchini, and J. P. Moeck. Perturbation theory of nonlinear, non-self-adjoint eigenvalue problems: Simple eigenvalues. *Journal of Sound and Vibration*, 473: 115200, May 2020. ISSN 0022460X. doi: 10.1016/j.jsv.2020.115200.

[60] G. A. Mensah, P. E. Buschmann, and A. Orchini. Iterative solvers for the thermoacoustic nonlinear eigenvalue problem and their convergence properties. *International Journal of Spray and Combustion Dynamics*, 14(1-2):30–41, 2022. ISSN 1756-8277, 1756-8285. doi: 10.1177/17568277221084464.

[61] N. Noiray, D. Durox, T. Schuller, and S. Candel. A Unified Framework for Nonlinear Combustion Instability Analysis Based on the Flame Describing Function. *J. Fluid Mech.*, 615:139–167, 2008. doi: 10.1017/S0022112008003613.

[62] A. Orchini and M. P. Juniper. Linear Stability and Adjoint Sensitivity Analysis of Thermoacoustic Networks with Premixed Flames. *Combustion and Flame*, 165:97–108, Mar. 2016. ISSN 00102180. doi: 10.1016/j.combustflame.2015.10.011.

[63] A. Orchini, L. Magri, C. F. Silva, G. A. Mensah, and J. P. Moeck. Degenerate perturbation theory in thermoacoustics: High-order sensitivities and exceptional points. *J. Fluid Mech.*, 903:A37, Nov. 2020. ISSN 0022-1120, 1469-7645. doi: 10.1017/jfm.2020.586.

[64] A. Orchini, C. F. Silva, G. A. Mensah, and J. P. Moeck. Thermoacoustic modes of intrinsic and acoustic origin and their interplay with exceptional points. *Combustion and Flame*, 211:83–95, Jan. 2020. ISSN 00102180. doi: 10.1016/j.combustflame.2019.09.018.

[65] T. Poinsot. Prediction and control of combustion instabilities in real engines. *Proceedings of the Combustion Institute*, 36(1):1–28, 2017. ISSN 15407489. doi: 10.1016/j.proci.2016.05.007.

[66] T. Poinsot and D. Veynante. *Theoretical and Numerical Combustion*. RT Edwards, Inc., 2005.

[67] W. Polifke. Modeling and analysis of premixed flame dynamics by means of distributed time delays. *Progress in Energy and Combustion Science*, 79:100845, July 2020. ISSN 03601285. doi: 10.1016/j.pecs.2020.100845.

[68] U. A. Qadri, L. Magri, M. Ihme, and P. J. Schmid. Optimal ignition placement in diffusion flames by nonlinear adjoint looping. In *Proceedings of the Summer Program*, 2016.

[69] G. Rigas, N. P. Jamieson, L. K. B. Li, and M. P. Juniper. Experimental Sensitivity Analysis and Control of Thermoacoustic Systems. *Journal of Fluid Mechanics*, 787, Jan. 2016. ISSN 0022-1120, 1469-7645. doi: 10.1017/jfm.2015.715.

[70] F. Schaefer and W. Polifke. Low-order network modeling of a duct with non-uniform cross-section and arbitrary mean temperature gradient in the presence of mean flow. In *AIAA Propulsion and Energy 2019 Forum*, Indianapolis, IN, USA, Aug. 2019. American Institute of Aeronautics and Astronautics. ISBN 978-1-62410-590-6. doi: 10.2514/6.2019-4376.

[71] F. Schaefer, S. Guo, and W. Polifke. The Impact of Exceptional Points on the Reliability of Thermoacoustic Stability Analysis. *Journal of Engineering for Gas Turbines and Power*, 143(2):021010, Feb. 2021. ISSN 0742-4795, 1528-8919. doi: 10.1115/1.4049351.

[72] F. Schaefer, L. Magri, and W. Polifke. A Hybrid Adjoint Network Model for Thermoacoustic Optimization. *Journal of Engineering for Gas Turbines and Power*, 144(3): 031017, Mar. 2022. ISSN 0742-4795, 1528-8919. doi: 10.1115/1.4051959.

[73] B. Schuermans, V. Bellucci, D. Nowak, and C. O. Paschereit. Modelling of Complex Thermoacoustic Systems: A State-Space Approach. In *Ninth Int. Congress on Sound and Vibration, ICSV9*, Orlando, FL, U.S.A., May 2002. IIAV.

[74] C. F. Silva. Intrinsic thermoacoustic instabilities. *Progress in Energy and Combustion Science*, 95:101065, Mar. 2023. ISSN 03601285. doi: 10.1016/j.pecs.2022.101065.

[75] C. F. Silva and W. Polifke. Non-dimensional groups for similarity analysis of thermoacoustic instabilities. *Proceedings of the Combustion Institute*, 37(4):5289–5297, 2019. ISSN 15407489. doi: 10.1016/j.proci.2018.06.144.

[76] C. F. Silva, M. Merk, T. Komarek, and W. Polifke. The Contribution of Intrinsic Thermoacoustic Feedback to Combustion Noise and Resonances of a Confined Turbulent Premixed Flame. In *International Symposium: Thermoacoustic Instabilities in Gas Turbines and Rocket Engines*, Garching, Germany, May 2016.

[77] C. F. Silva, L. Magri, T. Runte, and W. Polifke. Uncertainty quantification of growth rates of thermoacoustic instability by an adjoint Helmholtz solver. *J. Eng. Gas Turbines and Power*, 139(1):011901, 2017. doi: 10.1115/1.4034203.

[78] C. S. Skene and P. J. Schmid. Adjoint-based parametric sensitivity analysis for swirling M-flames. *Journal of Fluid Mechanics*, 859:516–542, Jan. 2019. ISSN 0022-1120, 1469-7645. doi: 10.1017/jfm.2018.793.

[79] F. Sogaro, P. Schmid, and A. S. Morgans. Sensitivity Analysis of Thermoacoustic Instabilities. In *24th International Congress on Sound and Vibration, ICSV 2017*, London, UK, July 2017. IIAV.

[80] F. M. Sogaro, P. J. Schmid, and A. S. Morgans. Thermoacoustic interplay between intrinsic thermoacoustic and acoustic modes: Non-normality and high sensitivities. *Journal of Fluid Mechanics*, 878:190–220, Nov. 2019. ISSN 0022-1120, 1469-7645. doi: 10.1017/jfm.2019.632.

[81] S. R. Stow and A. P. Dowling. Modelling of Circumferential Modal Coupling due to Helmholtz Resonators. In *Int'l Gas Turbine and Aeroengine Congress & Exposition*, Atlanta, GA, U.S.A., June 2003.

[82] R. I. Sujith, G. A. Waldherr, and B. Zinn. An Exact Solution for One-Dimensional Acoustic Fields in Duct with an Axial Temperature Gradient. *Journal of Sound and Vibration*, 184(3):389–402, 1995. doi: 10.1006/jsvi.1995.0323.

[83] S. Temkin. *Elements of Acoustics*. John Wiley & Sons, 1996.

[84] A. M. Tumin and A. V. Fedorov. Instability wave excitation by a localized vibrator in the boundary layer. *J Appl Mech Tech Phys*, 25(6):867–873, Nov. 1984. ISSN 0021-8944, 1573-8620. doi: 10.1007/BF00911661.

[85] D. Yang, D. Laera, and A. S. Morgans. A systematic study of nonlinear coupling of thermoacoustic modes in annular combustors. *Journal of Sound and Vibration*, 456:137–161, Sept. 2019. ISSN 0022-460X. doi: 10.1016/j.jsv.2019.04.025.

List of Figures

List of Tables

Appendices

Low-order Network Model of a Duct with Non-Uniform Cross-Section and Varying Mean Temperature in the Presence of Mean Flow

F. Schaefer* and W. Polifke †
Technical University of Munich, Faculty of Mechanical Engineering, D-85747 Garching, Germany

Stability analysis of thermoacoustic systems is often carried out with low-order network models. This paper introduces a method to include a duct element with varying cross-sectional area and an arbitrary mean temperature profile in a thermoacoustic network model. Based on the quasi one-dimensional form of the linearized Euler equations (LEEs) for a perfect, inviscid gas, the system equations are formulated in a state space framework in terms of the Riemann invariants f and g. This approach is predicated on one additional assumption, i.e. that the direct impact of entropy fluctuations on the acoustic waves inside the duct is small. A comparison of model results with analytical analysis shows excellent agreement. Eigenvalues are predicted with good accuracy, even for coarse grids. Furthermore, the mode shapes and frequency responses match those found in the literature, demonstrating the validity of the approach.

Introduction

Reliable prediction of unstable thermoacoustic behavior constitutes a major challenge in the design of combustion systems such as gas turbine engines. Driven by a coupling of heat release fluctuations and pressure oscillations, such instabilities manifest themselves as large-amplitude acoustic oscillations, which may reduce the operational flexibility of the engine or even cause structural damage. In order to avoid or reduce the costs of iterative, full-scale CFD calculations, primary engine design studies rely on *low order models* (LOM) to predict and eliminate thermoacoustic instabilities. This includes reducing the describing model equations to a (quasi-) one-dimensional domain, thus significantly decreasing the computational effort.

In network models, the system is decomposed into various subsystems, called *elements*. The complexity of each element is adjusted according to the level of detail required by the respective physical mechanisms. The global system dynamics can be obtained by interconnecting various elements, which are available in a network library. This architecture allows for efficient modeling of a wide variety of systems by combining the respective characteristic elements. An exemplary model of a combustion system is illustrated in Figure 1.

*Research Assistant, Technical University of Munich, Thermo-Fluid Dynamics Group, schaefer@tfd.mw.tum.de.
†Professor, Technical University of Munich, Thermo-Fluid Dynamics Group, polifke@tum.de.

Owing to its large number of applications in the field of thermoacoustics, duct elements with temperature gradient and variable cross section have been the subject of analysis in numerous publications during the last decade. Sujith et. al [1] derived an analytical solution for inhomogeneous, constant-area ducts in the absence of mean flow. This analysis was extended to incorporate mean flow by Karthik et. al [2]. Cummings [3] and Li and Morgans [4] also derived approximate analytical solutions for moderate Mach numbers using a WKB type approach. Analytical solutions have also been derived for certain duct shapes with constant temperature, e.g. the *exponential horn* [5].

Based on the general assumption of an inviscid flow with perfect gas properties, this paper derives the basic equations for a duct with both non-zero mean temperature gradient and non-uniform cross-sectional area in the presence of mean flow. The model assumes that the impact of entropy fluctuations on the acoustic field can be neglected. This assumption does not apply to systems where mean flow gradients and Mach numbers are large, e.g. as the flow enters a nozzle with choked cross-section. However, for systems of moderate Mach number and mean flow gradients the presented approach accurately resolves the acoustic field.

The model equations are incorporated as a new element into the low-order network model *taX*[*], introduced by Emmert and Jaensch [6]. Analytical solutions derived in previous works are used to verify the model.

Using this extension of the network model, the system dynamics can be obtained given arbitrary profiles of both mean temperature and cross-sectional area in the combustion chamber, thus accounting for heat transfer effects and a large variety of chamber geometries. The respective profile can be entered by the user either as an explicit function depending on the axial coordinate of the duct or by loading a data file that results from simulation or measurement.

Background

Network models often employ the *traveling wave approach*, i.e. the linearized Euler equations (LEEs) are solved based on Riemann decomposition of the primitive variables. Wave propagation is thus described in terms of two characteristic plane waves $f(t - x/c)$ and $g(t + x/c)$ propagating in the up- and downstream direction, respectively. For the modeling of longitudinal acoustics, this requires a (quasi) one-dimensional flow, i.e. all physical quantities are constant across the duct cross section and the fundamental mode is below the cut-off frequency. This representation

[*]tool available at https://gitlab.lrz.de/tfd/tax

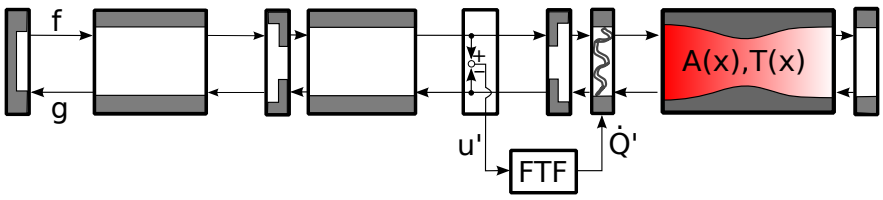

Fig. 1 Illustration of an exemplary network model including a duct with variable cross-sectional area and temperature profiles

of the acoustic field offers several advantages. On the one hand, the causality of the system is implicitly given by the direction of propagation of the input waves f at the entrance and g at the downstream end of the duct. On the other hand, the reflection (r) and transmission (t) behavior for each element is directly captured by the so-called *scattering matrix*, which relates the two traveling waves at downstream (d) and upstream (u) position:

$$\begin{bmatrix} g_u \\ f_d \end{bmatrix} = \underbrace{\begin{bmatrix} r_u & t_d \\ t_u & r_d \end{bmatrix}}_{S} \begin{bmatrix} f_u \\ g_d \end{bmatrix} \tag{1}$$

For a duct element with constant cross-sectional area and temperature, the two plane waves travel independently within the duct, i.e. they are decoupled ($r_d = 0, r_u = 0$).

However, if these waves are subject to a discontinuous change in the cross-sectional area, gas properties or, in general, impedance, they are partially reflected and partially transmitted. For smooth changes, the acoustic field can be seen as a superposition of reflected and transmitted waves caused by a multitude of infinitesimally discontinuous changes [7]. Consequently, the two plane waves do not propagate independently but are coupled as each wave undergoes continuously excited partial reflections.

Derivation of the model equations

To determine the relationship between the two coupled waves f and g, the quasi-one dimensional mass, momentum and energy conservation equations for a perfect, inviscid gas are considered [8]:

$$A\frac{\partial \rho}{\partial t} + \frac{\partial(\rho u A)}{\partial x} = 0 \tag{2}$$

$$\rho\frac{\partial u}{\partial t} + \rho u\frac{\partial u}{\partial x} + \frac{\partial p}{\partial x} = 0 \tag{3}$$

$$\frac{\partial s}{\partial t} + u\frac{\partial s}{\partial x} = \frac{R\dot{q}}{p}, \tag{4}$$

where ρ, u, p, s, R and A denote the density, axial velocity, pressure, specific entropy, the universal gas constant and cross-sectional area, respectively, and $\dot{q}$ represents the rate of heat release per unit of volume. By decomposing the flow into a steady, time-averaged flow (denoted $\bar{()}$) and small perturbations (denoted $()'$) the system can be linearized,

resulting in the LEEs:

$$\frac{\partial \rho'}{\partial t} + \bar{u}\frac{\partial \rho'}{\partial x} + u'\frac{\partial \bar{\rho}}{\partial x} + \bar{\rho}\frac{\partial u'}{\partial x} + \rho'\frac{\partial \bar{u}}{\partial x} + \frac{u'\bar{\rho}}{A}\frac{\partial A}{\partial x} + \frac{\bar{u}\rho'}{A}\frac{\partial A}{\partial x} = 0 \tag{5}$$

$$\bar{\rho}\frac{\partial u'}{\partial t} + \rho'\bar{u}\frac{\partial \bar{u}}{\partial x} + \bar{\rho}u'\frac{\partial \bar{u}}{\partial x} + \bar{\rho}\bar{u}\frac{\partial u'}{\partial x} + \frac{\partial p'}{\partial x} = 0 \tag{6}$$

$$\frac{\partial s'}{\partial t} + \bar{u}\frac{\partial s'}{\partial x} + \frac{R\bar{q}}{\bar{p}}\left(\frac{u'}{\bar{u}} + \frac{p'}{\bar{p}}\right) = 0. \tag{7}$$

Using the ansatz described in [4], fluctuations of density ρ' are expressed in terms of fluctuations of pressure p' and entropy s', the speed of sound c, the mean density $\bar{\rho}$ and the heat capacity at constant pressure $c_p = \gamma R/(\gamma - 1)$ (γ represents the ratio of specific heats):

$$\rho' = \frac{p'}{c^2} - \frac{\bar{\rho}}{c_p}s'. \tag{8}$$

Note that c_p is considered constant along the duct. Subsequently, by adding equations 5 and 7, the entropy fluctuations can be eliminated from the mass conservation equation. The linearized mass and momentum equations can then be expressed in terms of the acoustic pressure p' and the acoustic velocity u':

$$\frac{\partial p'}{\partial t} + \bar{u}\frac{\partial p'}{\partial x} + u'\frac{\partial \bar{p}}{\partial x} + \bar{p}\gamma\frac{\partial u'}{\partial x} + p'\gamma\frac{\partial \bar{u}}{\partial x} + \frac{u'\gamma\bar{p}}{A}\frac{\partial A}{\partial x} + \frac{\gamma\bar{u}p'}{A}\frac{\partial A}{\partial x} = 0, \tag{9}$$

$$\frac{\partial u'}{\partial t} + u'\frac{\partial \bar{u}}{\partial x} + \bar{u}\frac{\partial u'}{\partial x} + \frac{1}{\bar{\rho}}\frac{\partial p'}{\partial x} + \frac{p'\bar{u}}{\gamma\bar{p}}\frac{\partial \bar{u}}{\partial x} - \frac{\bar{u}s'}{c_p}\frac{\partial \bar{u}}{\partial x} = 0. \tag{10}$$

The last term in equation (10)) describes the direct, local impact of entropy fluctuations on the acoustic wave field. This term vanishes if there are no gradients in mean flow velocity $\bar{u}$. Furthermore, for moderate mean flow gradients and Mach numbers and large frequencies, the entropy fluctuations s' become insubstantial, as detailed in the Appendix. The acoustic field can then be considered decoupled from the entropy, i.e. it is fully described by equations (9) and (10). The energy equation (7) thus no longer needs to be considered as an additional model equation.

The system is transformed to generalized coordinates according to [9]

$$\begin{bmatrix} \frac{p'}{\bar{\rho}c} \\ u' \end{bmatrix} = \begin{bmatrix} 1 & 1 \\ 1 & -1 \end{bmatrix} \begin{bmatrix} f \\ g \end{bmatrix}, \tag{11}$$

with $c = \sqrt{\gamma RT}$ depending directly on the temperature T. The resulting two equations describe the acoustics of the duct in terms of f and g. The mean field quantities $\bar{p}, \bar{u}$ and $\bar{\rho}$ can be derived from the compressible Bernoulli equation and

the ideal gas law, as shown in Appendix A of [4].

$$\frac{\partial f}{\partial t} = -(\bar{u}+c)\frac{\partial f}{\partial x} - \underbrace{\frac{1}{2}\left(\frac{1}{\bar{\rho}c}\frac{\partial \bar{p}}{dx} + \left(\frac{\bar{u}}{c}+1\right)\frac{1}{\bar{\rho}}\frac{\partial \bar{\rho}c}{dx} + \left(\gamma+\frac{\bar{u}}{c}+1\right)\frac{\partial \bar{u}}{dx} + (c+\gamma\bar{u})\frac{1}{A}\frac{\partial A}{dx}\right)}_{\psi_1} f \tag{12}$$
$$- \underbrace{\frac{1}{2}\left(-\frac{1}{\bar{\rho}c}\frac{\partial \bar{p}}{dx} + \left(\frac{\bar{u}}{c}+1\right)\frac{1}{\bar{\rho}}\frac{\partial \bar{\rho}c}{dx} + \left(\gamma+\frac{\bar{u}}{c}-1\right)\frac{\partial \bar{u}}{dx} + (-c-\gamma\bar{u})\frac{1}{A}\frac{\partial A}{dx}\right)}_{\psi_2} g,$$

$$\frac{\partial g}{\partial t} = (-\bar{u}+c)\frac{\partial g}{\partial x} - \underbrace{\frac{1}{2}\left(\frac{1}{\bar{\rho}c}\frac{\partial \bar{p}}{dx} + \left(\frac{\bar{u}}{c}-1\right)\frac{1}{\bar{\rho}}\frac{\partial \bar{\rho}c}{dx} + \left(\gamma-\frac{\bar{u}}{c}-1\right)\frac{\partial \bar{u}}{dx} + (c-\gamma\bar{u})\frac{1}{A}\frac{\partial A}{dx}\right)}_{\psi_3} f \tag{13}$$
$$- \underbrace{\frac{1}{2}\left(-\frac{1}{\bar{\rho}c}\frac{\partial \bar{p}}{dx} + \left(\frac{\bar{u}}{c}-1\right)\frac{1}{\bar{\rho}}\frac{\partial \bar{\rho}c}{dx} + \left(\gamma-\frac{\bar{u}}{c}+1\right)\frac{\partial \bar{u}}{dx} + (-c+\gamma\bar{u})\frac{1}{A}\frac{\partial A}{dx}\right)}_{\psi_4} g$$

The first term on the right-hand side of equations (12) and (13) is in line with the model equations obtained for a simple duct (see [9]). However, for a variable cross-section with mean temperature gradient, both the mean axial velocity $\bar{u}(x)$ and the speed of sound $c(x)$ depend on the axial coordinate x of the duct, which has to be taken into account for the discretization of the system. The third term in equation (12) represents the influence of g on the evolution of f, and the second term in equation (13) represents the influence of f on g. The coupling of the two waves by scattering at mean flow gradients described at the beginning of this section is thus included and quantified in the model equations.

Implementation

The network model taX describes the acoustic system via a state space formalism. In the state space approach, a set of ordinary differential equations that relate the input u and output y of a system is used to represent the system dynamics

$$E\dot{x} = Ax + Bu,$$
$$y = Cx + Du,$$

where x is the state vector and A, B, C, D and E the system matrices [9]. In contrast to stability analysis in the frequency domain, the state-space formulation produces an easily solvable linear eigenvalue problem. In matrix form, equations (12)-(13) read

$$\frac{\partial}{\partial t}\begin{bmatrix} f \\ g \end{bmatrix} = \begin{bmatrix} -(c+\bar{u}) & 0 \\ 0 & (c-\bar{u}) \end{bmatrix}\frac{\partial}{\partial x}\begin{bmatrix} f \\ g \end{bmatrix} + \begin{bmatrix} \psi_1 & \psi_2 \\ \psi_3 & \psi_4 \end{bmatrix}\begin{bmatrix} f \\ g \end{bmatrix},$$

where ψ_1, ψ_2, ψ_3 and ψ_4 represent the labeled terms on the right-hand side of equations (12)-(13). Although a third order upwind scheme is used in taX, the discretization is demonstrated by way of example using a first order upwind scheme:

$$\begin{aligned}\frac{df_j}{dt} &= -(c_j + \bar{u}_j)\frac{f_j - f_{j-1}}{\Delta x} + \psi_{1,j} f_j + \psi_{2,j} g_j \\ &= \left(\frac{-(c_j + \bar{u}_j)}{\Delta x} + \psi_{1,j}\right) f_j + \frac{(c_j + \bar{u}_j)}{\Delta x} f_{j-1} + \psi_{2,j} g_j,\end{aligned} \tag{14}$$

$$\begin{aligned}\frac{dg_j}{dt} &= (c_j - u_j)\frac{g_{j+1} - g_j}{\Delta x} + \psi_{3,j} f_j + \psi_{4,j} g_j \\ &= \frac{(c_j - \bar{u}_j)}{\Delta x} g_{j+1} + \left(\frac{(c_j + \bar{u}_j)}{\Delta x} + \psi_{4,j}\right) g_j + \psi_{3,j} f_j.\end{aligned} \tag{15}$$

Note that g propagates in upstream direction and is discretized accordingly. The state space system is formalized with the state and input vectors

$$x^T = \begin{bmatrix} f_2 & f_3 & \cdots & f_n & g_1 & g_2 & \cdots & g_{n-1} \end{bmatrix}, u = \begin{bmatrix} f_1 \\ g_n \end{bmatrix},$$

where n is the number of discretization points within the duct element. The system matrix can be assembled as

$$A = A_{cu} + A_{\psi} = \begin{bmatrix} A_{cu,ff} & [0] \\ [0] & A_{cu,gg} \end{bmatrix} + \begin{bmatrix} A_{\psi,ff} & A_{\psi,fg} \\ A_{\psi,gf} & A_{\psi,gg} \end{bmatrix}, \tag{16}$$

where $A_{cu,ff}$ and $A_{\psi,ff}$ are given by

$$A_{cu,ff} = \frac{1}{\Delta x}\begin{bmatrix} -(c_2 + \bar{u}_2) & 0 & 0 & 0 & \cdots & 0 & 0 \\ (c_3 + \bar{u}_3) & -(c_3 + \bar{u}_3) & 0 & 0 & \cdots & 0 & 0 \\ 0 & (c_4 + \bar{u}_4) & -(c_4 + \bar{u}_4) & 0 & \cdots & 0 & 0 \\ \vdots & 0 & \ddots & \ddots & \cdots & \vdots & \vdots \\ 0 & 0 & 0 & 0 & \cdots & c_n + \bar{u}_n & -(c_n + \bar{u}_n) \end{bmatrix}, \tag{17}$$

$$A_{\psi,ff} = \begin{bmatrix} \psi_{1,2} & 0 & 0 & 0 & \cdots & 0 \\ 0 & \psi_{1,3} & 0 & 0 & \cdots & 0 \\ 0 & 0 & \psi_{1,4} & 0 & \cdots & 0 \\ \vdots & \vdots & 0 & \ddots & \cdots & \vdots \\ 0 & 0 & 0 & 0 & \cdots & \psi_{1,n} \end{bmatrix}, \tag{18}$$

and similarly for the other sub-matrices $A_{cu,gg}$, $A_{\psi,\_g}$.

The global system dynamics is obtained by interconnecting the individual subsystems. In this context, the global system matrices A, B, C, D and E are derived from the subsystem matrices (e.g. A_{duct1}, B_{duct1},..). A more detailed mathematical formulation can be found in [9]. Having determined the system matrices, the eigenvalues can be calculated by solving the linear eigenvalue problem

$$(Es - A)x = 0. \tag{19}$$

The system is stable if

$$\mathfrak{Re}(s_i) < 0 \tag{20}$$

for all eigenvalues s_i. This linear eigenvalue problem can be solved using standard algorithms, enabling efficient stability analysis, which represents a significant advantage of the state space approach over alternative methods. By interconnecting different elements, as illustrated in Figure 1, systems of arbitrary topology can be modeled and investigated regarding their stability behavior for specified parameter setups.

Results and Discussion

In order to verify the approach, the results of various taX models that include the new duct element are compared with (semi-)analytical solutions taken from the literature. Since analytical solutions only exist for either cross-sectional or temperature variations, the two effects are investigated separately.

Variable Cross-Section

The element is first evaluated for a duct with variable cross-sectional area. For this purpose, the case of an "exponential horn" is examined. For this duct geometry, the profile of the cross-sectional area is specified explicitly as a function of the axial coordinate of the duct as

$$A(x) = A(0)\exp(2mx) \tag{21}$$

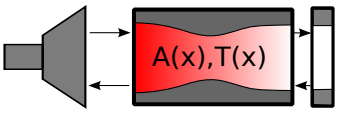

Fig. 2 Acoustic network system of an exponential horn

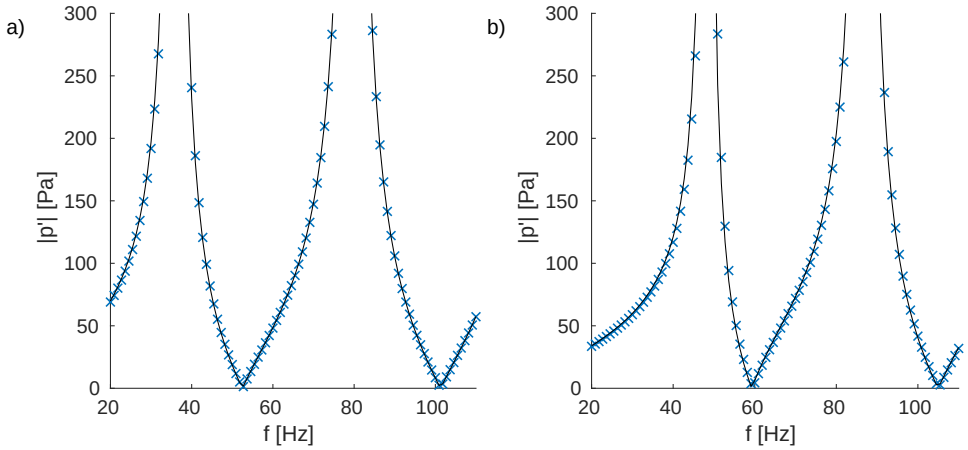

Fig. 3 Pressure magnitude at the throat of an exponential horn for $m = 1$ and $m = 2$, taX (x) vs. analytical (-) solution

where m is the mode number. Temkin [5] showed that an exact analytical solution for this case can be derived when the mean flow through the duct is set to zero. The schematic structure of the taX model is illustrated in Figure 2. The system is excited at the throat of the duct by a loudspeaker with constant forcing amplitude $\epsilon = 1m/s$. The mouth of the horn is considered an open end, its length is set to $L = 1m$. Gas properties along the duct remain constant. Figure 3 compares the pressure magnitude at the throat of the exponential horn obtained by taX with the analytical solution for the first two mode numbers. The results show excellent agreement between the numerical and the analytical solutions. A comparison of the eigenvalues further shows that the model predicts the eigenfrequencies for both a closed and an open ended duct with adequate accuracy with deviations around 1% for the first two eigenvalues using only $n = 25$ grid points.

Axial Temperature Gradient

By transforming the LEEs to the mean temperature space, Sujith et. al [1] were able to derive an analytically solvable expression describing the acoustics in a duct with a linear temperature profile. However, the applicability of that study is limited to flows with small Mach numbers, as mean flow effects are neglected. Li and Morgans [4] extended this work to non-linear temperature profiles using an adapted WKB approximation. Since only Mach number terms of higher order than M^2 were neglected, the analysis is valid for low and moderate Mach number flows.

In this section the proposed model is validated against both of these analytical approaches. Table 1 lists the first

Table 1 Comparison of the first four taX eigenfrequencies with analytical solution

$T(x) = T_1 + mx$	T1 [K]	500	700	900	1100
	$m[K/m]$	-50	-100	-150	-200
$f_0[1/s]$	taX	23.54	25.04	26.33	27.48
	analytical	23.61	25.15	26.48	27.67
$f_1[1/s]$	taX	74.16	81.56	87.92	93.69
	analytical	74.23	81.61	88	93.7
$f_2[1/s]$	taX	124.02	136.69	147.67	157.47
	analytical	124.15	136.8	147.74	157.51
$f_3[1/s]$	taX	173.61	191.43	206.84	220.62
	analytical	173.97	191.81	207.24	221.03

four eigenfrequencies for different linear temperature profiles obtained by the low-order network model and compares them to the exact solution derived by Sujith et. al [1]. The model considers a duct of length $L = 4m$ which is closed at one and open at the other end. The temperature at the open end is fixed at $T_2 = 300K$, whereas the temperature at the duct entrance T_1 and the slope of the linear temperature profile m are increased gradually. Due to the open-closed boundary conditions, the fundamental mode f_0 corresponds to a quarter wave and the first three harmonics f_1, f_2 and f_3 to a three-quarter, five-quarter and seven-quarter wave, respectively. The duct is discretized using a grid size of $n = 25$, which corresponds to a resolution of only 10 grid points for the shortest wavelength ($f \approx 200s^{-1}$) of the constant-temperature reference case ($T(x) = T_2$).

Table 1 confirms that the effect of the temperature profile on the eigenvalues is reliably captured by the proposed network model approach. Despite the coarse resolution of the grid, the first four eigenfrequencies are calculated with a maximum deviation of 0.7%.

To test the model for non-linear temperature profiles and to include the effect of mean flow, the frequency response of the modeled system is compared to the analytical solution given by [4]. The non-linear temperature profile is given as

$$T(x) = \frac{T_1 - T_2}{2} \sin\left(\frac{5\pi}{4}\frac{x}{L} + \frac{\pi}{4}\right) + \frac{T_1 + T_2}{2}.$$

This function describes an initially rising and then gradually falling temperature curve, which corresponds roughly to a temperature profile in combustion chambers. Figure 4 shows the predicted gain and phase of the normalized acoustic pressure (a and c) and velocity (b and d) along the duct. The model parameters are set to $L = 1m$, $\gamma = 1.4$, $R = 287$, $M = 0$, $T_1 = 1600$, $T2 = 800$ and $f = 1.5c_0$, where f is the frequency and c_0 is the speed of sound at axial position $x = 0$. The duct element is discretized using a uniform grid containing 100 grid points. The numerical and analytical results are in good agreement with a maximum deviation of 3% in both gain and phase. It is thus concluded that the model can make reliable predictions even for non-linear temperature profiles.

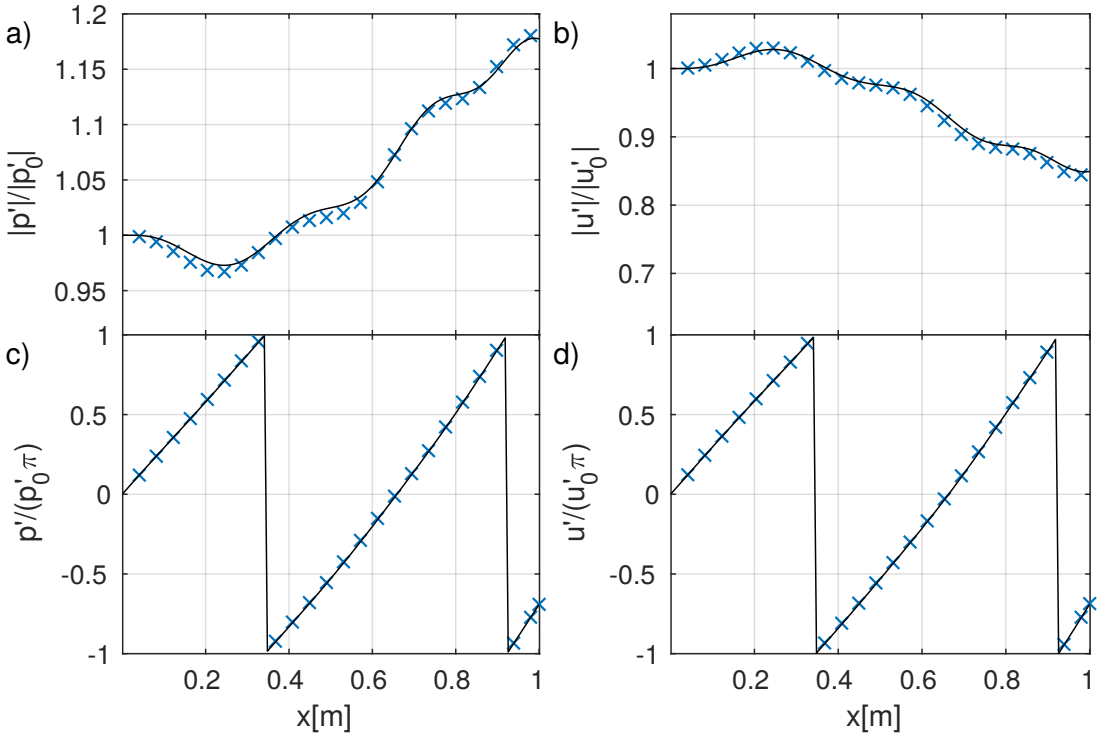

Fig. 4 Frequency response with $f = 1.5c_0$, $M = 0$ and a non-linear temperature profile along the duct. Analytical (-) vs. taX (x) solution

In order to ensure the accuracy of the analytic solution, the effect of mean flow is investigated for a linear temperature profile. The mean flow velocity is defined by the Mach number $M = 0.2$ at the entrance of the duct. Besides the Mach number and the temperature profile, all model parameters are adopted from the non-linear case. The temperature function is given by

$$T(x) = T_1 - \frac{T_1 - T_2}{L} x.$$

Figure 5 shows the frequency response for the linear temperature profile in the presence of mean flow. The numerical solution matches the analytical prediction almost perfectly, deviating by a maximum of 0.46% in gain and 0.26% in phase for a resolution of 80 grid points. The effect of mean temperature upon the acoustic field is thus adequately resolved.

Conclusion

A method for integrating a duct element with variable cross-sectional area and mean temperature gradient into a network model was presented. The comparison with analytical results has shown that the model predicts both eigenfrequencies and the development of the acoustic quantities with satisfactory accuracy at low computational cost. In

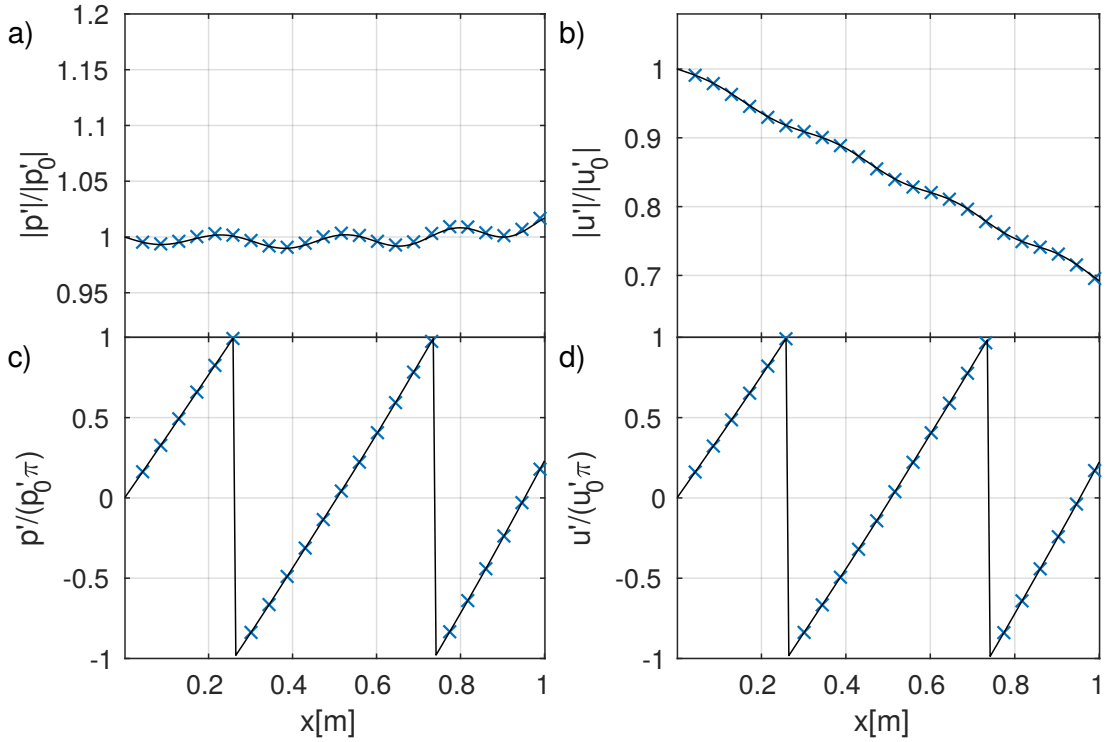

Fig. 5 Frequency response with $f = 1.5c_0$, $M = 0.2$ and a linear temperature profile along the duct. Analytical (-) vs. taX (x) solution

contrast to the analytical approaches, neither the temperature nor the cross-sectional area profiles are restricted to specific functions. Furthermore, a change of one of these functions does not require a renewed analysis but is automatically integrated into the model equations. Due to the network architecture, the duct element can also be used with arbitrary boundary conditions and in combination with other, more complex elements, both of which would greatly complicate an analytical analysis.

The consideration of temperature and area gradients allows more accurate modeling of a variety of systems as it incorporates heat transfer effects and is able to represent geometrically complex burner systems. The introduced element is thus a valuable extension to the existing network system, and may constitute an important feature for future investigations.

Appendix

The influence of entropy wave generation on the acoustic field

By inserting Gibbs' relation into the time-averaged energy equation, an expression for the time-averaged volumetric heat flux $\bar{\dot{q}}$ can be found. All perturbations are assumed harmonic and can be expressed as $y' = \hat{y}e^{i\omega t}$. The entropy

wave $\hat{s}$ can then be obtained by solving the following differential equation

$$\hat{s} + \frac{\bar{u}}{i\omega}\frac{d\hat{s}}{dx} = \frac{\bar{u}c_p}{i\omega}\left((1-M^2)\frac{1}{\bar{\rho}}\frac{d\bar{\rho}}{dx} + \frac{M^2}{A}\frac{dA}{dx}\right)\left(\frac{\hat{p}}{\bar{p}} + \frac{\hat{u}}{\bar{u}}\right). \tag{22}$$

The right-hand side of equation 22 represents the generation of entropy due to the interaction of the acoustic waves with mean flow gradients. For low Mach number flows, terms of order $M^2 << 1$ can be neglected. Furthermore, the pressure perturbations of plane waves can be estimated as $\hat{p} \sim O(\bar{\rho}c\hat{u})$, rendering pressure fluctuations in equation 22 negligible compared to velocity fluctuations [4]. The entropy wave equation is thus obtained as

$$\hat{s} + \frac{\bar{u}}{i\omega}\frac{d\hat{s}}{dx} \approx -\frac{c_p}{i\omega}\frac{1}{T}\frac{dT}{dx}\hat{u}. \tag{23}$$

For a duct with constant temperature and for sufficiently high frequencies with moderate temperature gradients, the right-hand side of equation 23 is negligible. The resulting entropy wave is then described by

$$s'(x,t) = \hat{s}(x=0)e^{i(\omega t - kx)}. \tag{24}$$

Assuming that there is no entropy wave entering the system ($s'(x=0)=0$), entropy perturbations can be neglected altogether, allowing us to proceed with the two-equations system.

References

[1] Sujith, R. I., Waldherr, G. A., and Zinn, B., "An Exact Solution for One-Dimensional Acoustic Fields in Duct with an Axial Temperature Gradient," *Journal of Sound and Vibration*, Vol. 184, No. 3, 1995, pp. 389–402.

[2] Karthik, B., Kumar, B. M., and Sujith, R. I., "Exact Solutions to One-Dimensional Acoustic Fields with Temperature Gradient and Mean Flow," *The Journal of the Acoustical Society of America*, Vol. 108, No. 1, 2000, pp. 38–43.

[3] Cummings, A., "Ducts with Axial Temperature Gradients: An Approximate Solution for Sound Transmission and Generation," *Journal of Sound and Vibration*, Vol. 51, No. 1, 1977, pp. 55–67.

[4] Li, J., and Morgans, A. S., "The One-Dimensional Acoustic Field in a Duct with Arbitrary Mean Axial Temperature Gradient and Mean Flow," *Journal of Sound and Vibration*, Vol. 400, 2017, pp. 248–269. doi:10.1016/j.jsv.2017.03.047.

[5] Temkin, S. (ed.), *Elements of Acoustics*, John Wiley & Sons, 1996.

[6] Emmert, T., Jaensch, S., Sovardi, C., and Polifke, W., "taX - a Flexible Tool for Low-Order Duct Acoustic Simulation in Time and Frequency Domain," *7th Forum Acusticum*, DEGA, Krakow, 2014.

[7] Subrahmanyam, P. B., Sujith, R. I., and Lieuwen, T. C., "A Family of Exact Transient Solutions for Acoustic Wave Propagation in Inhomogeneous, Non-Uniform Area Ducts," *J. of Sound and Vibration*, , No. 4, 2001, pp. 705–715.

[8] Nicoud, F., and Wieczorek, K., "About the Zero Mach Number Assumption in the Calculation of Thermoacoustic Instabilities," *International Journal of Spray and Combustion Dynamics*, Vol. 1, No. 1, 2009, pp. 67–111.

[9] Emmert, T., Meindl, M., Jaensch, S., and Polifke, W., "Linear State Space Interconnect Modeling of Acoustic Systems," *Acta Acustica united with Acustica*, Vol. 102, No. 5, 2016, pp. 824–833. doi:10.3813/AAA.918997.

[10] Li, J., and Morgans, A. S., "Simplified Models for the Thermodynamic Properties along a Combustor and Their Effect on Thermoacoustic Instability Prediction," *Fuel*, Vol. 184, 2016, pp. 735–748. doi:10.1016/j.fuel.2016.07.050.

Felicitas Schäfer[1]
Department of Mechanical Engineering,
Technical University of Munich,
Garching 85748, Germany
e-mail: schaefer@tfd.mw.tum.de

Luca Magri
Aeronautics Department South Kensington Campus,
Imperial College London,
London SW7 2AZ, UK

Wolfgang Polifke
Department of Mechanical Engineering,
Technical University of Munich,
Garching 85748, Germany

A Hybrid Adjoint Network Model for Thermoacoustic Optimization

A method is proposed that allows the computation of the continuous adjoint of a thermoacoustic network model based on the discretized direct equations. This hybrid approach exploits the self-adjoint character of the duct element, which allows all jump conditions to be derived from the direct scattering matrix. In this way, the need to derive the adjoint equations for every element of the network model is eliminated. This methodology combines the advantages of the discrete and continuous adjoint, as the accuracy of the continuous adjoint is achieved while maintaining the flexibility of the discrete adjoint. It is demonstrated how the obtained adjoint system may be utilized to optimize a thermoacoustic configuration by determining the optimal damper setting for an annular combustor.
[DOI: 10.1115/1.4051959]

1 Introduction

As emission regulations have become stricter, the development of gas turbine engines has increasingly shifted to engines operating at lean combustion conditions. However, a significant drawback of this design technique is that such flames become more responsive to acoustics. A constructive coupling of pressure and heat release fluctuations at the flame may result in an amplification of oscillations, which can affect engine emissions, decrease the engine lifetime, and cause structural damage [1]. Predicting and controlling thermoacoustic instabilities has, therefore, become a major challenge in the development of modern gas turbine engines. The design of a system that is linearly stable over the entire operating regime may require extensive testing, curtailments in flexibility by avoiding specific operating conditions, or the retrofitting of passive dampers such as Helmholtz resonators. To avoid costs caused by late adaptions to the design, thermoacoustic stability analysis is incorporated into primary engine development [2]. These analyses rely on different levels of abstraction to model the thermoacoustic system. Being highly flexible and cost-efficient, low-order network models have become an essential tool for the prediction and elimination of instabilities in early stages of the design process. Network models are applied to determine the system eigenmodes, which are linearly stable if their growth rates are negative. Having identified an unstable mode, the system parameters need to be adapted in order to stabilize the system. Unfortunately, since thermoacoustic systems are highly sensitive to a large number of parameters, adjusting the parameters via trial-and-error may be prohibitively expensive [3,4]. A more efficient approach to optimize the system employs adjoint analysis. Adjoint methods allow the computation of the sensitivity of an eigenvalue with respect to *all* parameters with only one additional computation [4,5]. In contrast, approximating the sensitivity with a finite difference approach would require at least one additional computation for each system parameter, while yielding less accurate results. For comparable accuracy, higher order finite difference schemes would be required, which further increases the computational cost. As such, adjoint analysis has shown to be highly efficient for the analysis and optimization of thermoacoustic systems. The systematic determination of the optimal parameter setting may be used a priori to determine the most influential parameters and to tune them in order to design a system that is stable over its range of operating conditions, and a posteriori to determine the optimal placement and geometric parameters of damping devices [2,4]. Mensah et al. [6] presented a strategy on optimal placement and parameter tuning of a Helmholtz resonator in an annular combustor based on adjoint perturbation theory. Another application of the adjoint theory is the quantification of uncertainty, where cheap surrogate models may be identified to significantly decrease the overall computational cost [7,8].

There are two different approaches to integrate adjoint analysis into low-order network models: the continuous adjoint (CA), where the adjoint equations are derived from the primary equations and discretized afterward, and the discrete adjoint (DA), which is derived from the discretized form of the direct equations. The discrete adjoint approach is, in general, easier to implement for an existing tool, as it merely requires evaluation of the complex conjugate system matrix [5]. However, the resulting adjoint eigenmodes often exhibit spurious oscillations at the boundary and jump conditions, which may deteriorate the analysis. This was elaborated in Ref. [2], where the author compared the combination of various discretization schemes with the CA and DA approach, respectively, for a Helmholtz solver modeling a Rijke tube. The study finds that the DA with a finite difference discretization leads to oscillation in the adjoint system. Since the original software tool is based on a finite difference discretization of the duct element, eliminating spurious oscillations would require fundamental changes of the software tool.

The adjoint system obtained via the CA approach does not suffer from this shortcoming. However, deriving the adjoint equations for each element is time-consuming and involves the implementation of a completely new set of adjoint elements. An example of the CA approach applied to a network model is shown by Aguilar et al. [9]. The study introduces a wave-based adjoint network model for a simple system configuration, where the (continuous) adjoint equations and jump conditions are derived for each element of the thermoacoustic system. Next to the elimination of spurious predictions near jump conditions, the system analysis via the CA approach offers physical insight into the original system, since adjoint equations may be interpreted directly.

In this paper, we introduce an approach that eliminates the need to derive the adjoint equations for each element to receive the adjoint of a (thermo-)acoustic network model of arbitrary topology and complexity. Based on the adjoint equations of a simple duct element, the adjoint scattering matrix for a generic compact element is derived as a function of the direct scattering matrix. This approach maintains the flexibility of the discrete adjoint and is easily implemented in the original network model tool. It further allows the consideration of entropy waves without adding significant effort. At the

[1]Corresponding author.
Manuscript received July 8, 2021; final manuscript received July 14, 2021; published online January 3, 2022. Editor: Jerzy T. Sawicki.

same time, problems stemming from the transformation to the adjoint system with the DA approach are avoided.

The paper is structured as follows: We first introduce the structure of the network model considered in this study. In the following two sections, we derive the adjoint system and the corresponding expressions for the base state and feedback sensitivities. We validate our model by comparing it to an adjoint Helmholtz model, on the one hand, and to results obtained from the discrete adjoint, on the other hand. We subsequently show how our model may be used to optimize the parameter setting of a system of passive damping devices for an annular combustor. The last section concludes this study.

Thermoacoustic Network Models

The proposed approach to incorporate adjoint analysis into a low-order network model framework is based on the TU Munich software TAX [10]. However, proposed derivations of the system can, after some adaptions, be applied to any thermoacoustic network model. Unlike most other implementations of thermoacoustic network models, TAX is based on a representation of the thermoacoustic system in the time domain as a state-space system. The resulting eigenvalue problem is linear, offering a compelling advantage to frequency domain considerations. On the other hand, unlike frequency domain models, the TAX framework is not able to incorporate directly nonlinear analytical expressions, such as the solution of the duct element. Consequently, the respective elements need to be discretized, which introduces discretization errors that grow with frequency and may result in large system matrices, especially for networks that are comprised of many elements.

The Representation of the Duct Element in TAX

The network model separated the system into various base elements, of which the duct is assumed to be the only component with significant axial extend, i.e., all other elements are treated as acoustically compact. The element equations for the thermoacoustic duct are derived from the Euler equations for a perfect gas. For flows where viscosity and heat conduction are neglected, these are expressed in terms of the density ρ, the velocity u, and the pressure p

$$\frac{\partial \rho}{\partial t} + u\frac{\partial \rho}{\partial x} + \rho\frac{\partial u}{\partial x} = 0 \tag{1a}$$

$$\rho\frac{\partial u}{\partial t} + \rho u\frac{\partial u}{\partial x} + \frac{\partial p}{\partial x} = 0 \tag{1b}$$

$$\frac{\partial p}{\partial t} + u\frac{\partial p}{\partial x} + \gamma p\frac{\partial u}{\partial x} = 0 \tag{1c}$$

In order to linearize the system, we decompose the primitive variables into a steady, time-averaged part (denoted $\bar{}$) and a small perturbation part (denoted $'$). Following Ref. [2], we perturb the acoustic equations by injecting a mass term per unit volume per unit time $\varepsilon\delta\dot{m}$, a force term per unit volume $\varepsilon\delta f$, and a heat release rate term per unit volume per unit time $\varepsilon\delta\dot{q}$. These perturbations can represent any physical perturbation to the system and will later be used to derive the feedback sensitivity. However, for the following derivation of the direct and adjoint equations, the perturbation terms are initially set to zero

$$\frac{\partial \rho'}{\partial t} + \bar{u}\frac{\partial \rho'}{\partial x} + \bar{\rho}\frac{\partial u'}{\partial x} = \varepsilon\delta m \tag{2a}$$

$$\bar{\rho}\frac{\partial u'}{\partial t} + \bar{\rho}\bar{u}\frac{\partial u'}{\partial x} + \frac{\partial p'}{\partial x} = \varepsilon\delta f \tag{2b}$$

$$\frac{\partial p'}{\partial t} + \bar{u}\frac{\partial p'}{\partial x} + \gamma\bar{p}\frac{\partial u'}{\partial x} = \varepsilon\delta\dot{q} \tag{2c}$$

The mean flow quantities are assumed to be constant over the duct. We replace the density fluctuations by the normalized entropy fluctuations $\varsigma' = s'/c_p = p'/(\gamma\bar{p}) - \rho'/\bar{\rho}$. This is convenient, as the density depends on both pressure and entropy oscillations. The system of equations thus reduces to

$$E_1 := \frac{\partial p'}{\partial t} + \bar{u}\frac{\partial p'}{\partial x} + \gamma\bar{p}\frac{\partial u'}{\partial x} = 0 \tag{3a}$$

$$E_2 := \bar{\rho}\frac{\partial u'}{\partial t} + \bar{\rho}\bar{u}\frac{\partial u'}{\partial x} + \frac{\partial p'}{\partial x} = 0 \tag{3b}$$

$$E_3 := \frac{\partial \varsigma'}{\partial t} + \bar{u}\frac{\partial \varsigma'}{\partial x} = 0 \tag{3c}$$

This system can be decoupled using the characteristic wave amplitudes f, g, and ς, yielding the following system of equations:

$$\frac{\partial}{\partial t}\begin{bmatrix} f \\ g \\ \varsigma \end{bmatrix} = \begin{bmatrix} -(\bar{c}+\bar{u}) & 0 & 0 \\ 0 & (\bar{c}-\bar{u}) & 0 \\ 0 & 0 & -\bar{u} \end{bmatrix}\frac{\partial}{\partial x}\begin{bmatrix} f \\ g \\ \varsigma \end{bmatrix} \tag{4}$$

Equation (4) describes two plane waves f and g propagating in down- and upstream direction with the velocities $(\bar{c}+\bar{u})$ and $(\bar{c}-\bar{u})$, respectively. In addition, an entropy wave ς propagates downstream with the mean flow velocity $\bar{u}$. Thus, the incident waves f_u, g_d, and ς_u leave the duct section after a time delay inversely proportional to their propagating velocity. In the Laplace domain, this relation is captured by the scattering matrix S of the duct section

$$\begin{bmatrix} g_u \\ f_d \\ \varsigma_d \end{bmatrix} = \underbrace{\begin{bmatrix} 0 & e^{-s\tau_g} & 0 \\ e^{-s\tau_f} & 0 & 0 \\ 0 & 0 & e^{-s\tau_\varsigma} \end{bmatrix}}_{S}\begin{bmatrix} f_u \\ g_d \\ \varsigma_u \end{bmatrix} \tag{5}$$

which leads to a nonlinear problem in the eigenvalue s. As there exist efficient solvers for algebraic eigenvalue problems, it is advantageous to approximate this solution by a state-space model. In TAX, Eq. (4) is, therefore, discretized in space, yielding a system of form

$$\dot{x} = Ax + Bu \tag{6}$$

The Representation of the Flame Element in TAX

For compact elements, such as temperature and area jumps, the element dynamics are described by the element scattering matrix. However, the integration of a time-delay flame model again introduces a nonlinearity in the eigenvalue. For example, the n-τ-model assumes that the flame response to a velocity perturbation at the root of the flame is a delayed fluctuation in the heat release fluctuation

$$\dot{Q}' = nu'(t-\tau) \tag{7}$$

which can be solved analytically in the Laplace domain

$$\dot{Q}' = ne^{-s\tau}u'(s) \tag{8}$$

A state-space representation can be retrieved by expressing the delay by an advection equation with an artificial state $\tilde{x}$, whose values at the boundaries determine the time delay [11]

$$\frac{\partial \tilde{x}}{\partial t} + \frac{\partial \tilde{x}}{\partial \theta} = 0 \tag{9a}$$

$$\tilde{x}(t)|_{\theta=0} = u'(t) \tag{9b}$$

$$\tilde{x}(t)|_{\theta=\tau} = u'(t-\tau) \tag{9c}$$

Subsequent spatial discretization of this artificial advection equation transforms the flame model into a state-space model. By increasing the resolution, the accuracy may be improved. This represents a significant advantage to approximation schemes like a rational polynomial approximation of the exponential function.

Discontinuities

Compact elements representing a discontinuity, such as area or temperature jumps, are fully described via their respective scattering matrix, which relates the up- and downstream characteristic wave amplitudes to each other, as demonstrated for the duct element in Eq. (5). In general, the components $S_{1,1}$, $S_{1,2}$, $S_{2,1}$, and $S_{2,2}$ describe the acoustic matrix and express the reflection and transmission behavior of the plane waves across the element. $S_{1,3}$ and $S_{2,3}$ express the contribution of entropy fluctuations to acoustics, which is zero for elements with constant mean temperature. Correspondingly, $S_{3,1}$ and $S_{3,2}$ quantify the entropy fluctuations related to acoustics, while $S_{3,3}$ is the part of entropy fluctuations that is convected through the discontinuity.

In summary, each element in the TAX framework is described in terms of the element matrices A_e, B_e, C_e, and D_e, as

$$\dot{x_e} = A_e x + B_e u \tag{10}$$

$$y = C_e x + D_e u \tag{11}$$

By interconnecting theses matrices [10], the global system matrices are obtained. The problem, thus, reduces to a linear eigenvalue problem

$$(A_g - \mathrm{sI})q = 0 \tag{12}$$

where A_g is the global system matrix, $s = \omega i + \sigma$ is the complex-valued eigenvalue with frequency ω and growth rate σ, and q is the corresponding eigenfunction.

Derivation of the Hybrid Adjoint System

In this section, we derive the adjoint transformation of a generic direct network model to its corresponding adjoint system.

The Adjoint Duct

In order to derive the hybrid adjoint (HA) system, we first derive the continuous adjoint equations for the duct element. From the direct Euler Eq. (3), we create a Lagrange functional [4] as follows:

$$\mathcal{L} = \langle p^\dagger | E_1 \rangle + \langle u^\dagger | E_2 \rangle + \langle \varsigma^\dagger | E_3 \rangle \tag{13}$$

Note that the Lagrangian for the entire network model also includes the jump conditions (*cf.* Ref. [9]), which may have an impact on the normalization of eigenfunctions for the calculation of the base state and feedback sensitivities. The Lagrangian approach demands that the first variation of the Lagrangian with respect to any variably ξ be equal to zero, for arbitrary variations $\delta\xi$

$$\frac{\partial \mathcal{L}}{\partial \xi} = \lim_{\varepsilon \to 0} \frac{\mathcal{L}(\xi + \varepsilon\delta\xi) - \mathcal{L}(\xi)}{\varepsilon} \tag{14}$$

Equation (14) is trivially given when ξ is one of the adjoint variables, which leads to the original direct system equations. We derive the adjoint equations by evaluating the derivatives of the Lagrangian with respect to the direct variables. This requires integration by parts, resulting in a set of adjoint equations

$$\frac{\partial \rho^\dagger}{\partial t} + \bar{u}\frac{\partial \rho^\dagger}{\partial x} = 0 \tag{15a}$$

$$\bar{\rho}\frac{\partial u^\dagger}{\partial t} + \bar{\rho}\bar{u}\frac{\partial u^\dagger}{\partial x} + \gamma\bar{p}\frac{\partial p^\dagger}{\partial x} = 0 \tag{15b}$$

$$\frac{\partial p^\dagger}{\partial t} + \bar{u}\frac{\partial p^\dagger}{\partial x} + \frac{\partial u^\dagger}{\partial x} = 0 \tag{15c}$$

along with the relationship between direct and adjoint boundary terms at $x = 0$ and $x = L$

$$[p'(u^\dagger + p^\dagger) + u'(\bar{\rho}\bar{c}^2 p^\dagger + \bar{\rho}\bar{u}u^\dagger) + \bar{u}\varsigma'\varsigma^\dagger]_0^L = 0 \tag{16}$$

Diagonalizing Eq. (15) reveals the self-adjoint character of the duct (cf. Eq. (4))

$$\frac{\partial}{\partial t}\begin{bmatrix} f^\dagger \\ g^\dagger \\ \varsigma^\dagger \end{bmatrix} = \frac{\partial}{\partial x}\begin{bmatrix} c+\bar{u} & 0 & 0 \\ 0 & \bar{u}-c & 0 \\ 0 & 0 & \bar{u} \end{bmatrix}\begin{bmatrix} f^\dagger \\ g^\dagger \\ \varsigma^\dagger \end{bmatrix} \tag{17}$$

Thus, the duct element does not require any modification of the original network software to obtain the adjoint system. The relationship between the adjoint primitive variables and the corresponding Riemann invariants follows as:

$$p^\dagger = (f^\dagger + g^\dagger)/\bar{c} \tag{18}$$

$$u^\dagger = (f^\dagger - g^\dagger) \tag{19}$$

Substituting the adjoint and direct Riemann invariants into Eq. (16) gives

$$\left[\bar{\rho}gg^\dagger(\bar{c}-\bar{u}) - \bar{\rho}ff^\dagger(\bar{c}+\bar{u}) - \varsigma\varsigma^\dagger\bar{u}\right]_0^L = 0 \tag{20}$$

Transformation of the Scattering Matrix

From the conditions (20), the direct scattering matrix can be transformed into its corresponding adjoint scattering matrix without the need to derive the adjoint jump conditions. For clarity, we show the derivation of the adjoint scattering matrix only for a 2×2 acoustic scattering matrix, where the acoustic-entropy coupling is negligible and entropy oscillations are convected across the discontinuity without any amplification or damping. This simplified system is illustrated in Fig. 1.

The direct scattering matrix is then generally described as

$$\begin{bmatrix} g_u \\ f_d \end{bmatrix} = \begin{bmatrix} S_{11} & S_{12} \\ S_{21} & S_{22} \end{bmatrix}\begin{bmatrix} f_u \\ g_d \end{bmatrix} \tag{21}$$

The relevant terms of the duct boundary conditions are those corresponding to the downstream end of duct 1

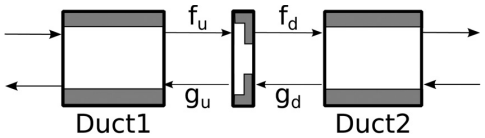

Fig. 1 Exemplary illustration of a network consisting of two ducts and a discontinuity

($f_u = f_{\text{duct1}}(x_1 = L_1)$, $g_u = g_{\text{duct1}}(x_1 = L_1)$) and the upstream end of duct 2 ($f_d = f_{\text{duct2}}(x_2 = 0)$, $g_d = g_{\text{duct2}}(x_2 = L_2)$)

$$g_u g_u^{\dagger} \bar{\rho}_u(\bar{c}_u - \bar{u}_u) - f_u f_u^{\dagger} \bar{\rho}_u(\bar{c}_u + \bar{u}_u) - (g_d g_d^{\dagger} \bar{\rho}_d(\bar{c}_d - \bar{u}_d) - f_d f_d^{\dagger} \bar{\rho}_d(\bar{c}_d + \bar{u}_d)) = 0 \tag{22}$$

The information given by the direct scattering matrix can now be substituted into Eq. (22)

$$((S_{11} f_u + S_{12} g_d) g_u^{\dagger} \bar{\rho}_u(\bar{c}_u - \bar{u}_u) - f_u f_u^{\dagger} \bar{\rho}_u(\bar{c}_u + \bar{u}_u)) - (g_d g_d^{\dagger} \bar{\rho}_d(\bar{c}_d - \bar{u}_d) - (S_{21} f_u + S_{22} g_d) f_d^{\dagger} \bar{\rho}_d(\bar{c}_d + \bar{u}_d)) = 0 \tag{23}$$

The adjoint scattering matrix follows from the requirement that Eq. (23) must hold for every f_u, g_d:

$$S^{\dagger} = \frac{1}{\det(S)} \begin{bmatrix} \dfrac{S_{22}(\bar{c}_u + \bar{u}_u)}{(\bar{c}_u - \bar{u}_u)} & -\dfrac{S_{21}\bar{\rho}_d(\bar{c}_d - \bar{u}_d)}{\bar{\rho}_u(\bar{c}_u - \bar{u}_u)} \\ -\dfrac{S_{12}\bar{\rho}_u(\bar{c}_u + \bar{u}_u)}{\bar{\rho}_d(\bar{c}_d + \bar{u}_d)} & \dfrac{S_{11}(\bar{c}_d - \bar{u}_d)}{(\bar{c}_d + \bar{u}_d)} \end{bmatrix} \tag{24}$$

This transformation of the direct into the adjoint scattering matrix is valid for all elements that are fully captured by the 2×2 acoustic scattering matrix. We thus eliminate the need to derive the adjoint equations from first principle for each compact element for every system as demonstrated in Ref. [9]. The adjoint model inherently relies on the same assumption made to the original element. The consideration of entropy waves, i.e., the derivation of the 3×3 adjoint scattering matrix, does not introduce any additional difficulties and can be performed in the same manner as demonstrated for the acoustic scattering matrix.

Transformation of the Flame Element

As described in the section The Representation of the Flame Element in Tax, the flame element in TAX is not described via a scattering matrix, but the time delay is discretized in the element state matrix A. It is, therefore, not possible to use the adjoint scattering matrix to transform the element into its associated adjoint element. For a direct system, the element equations are given by

$$\begin{bmatrix} g_u \\ f_d \end{bmatrix} = \begin{bmatrix} S_{11} & S_{12} & S_{13} \\ S_{21} & S_{22} & S_{23} \end{bmatrix} \begin{bmatrix} f_u \\ g_d \\ Q'_{\text{norm}} \end{bmatrix} \tag{25}$$

with

$$Q'_{\text{norm}} = \frac{Q'}{\bar{Q}} = \mathcal{F} \frac{u'_{\text{ref}}}{\bar{u}_{\text{ref}}} \tag{26}$$

where u'_{ref} is a normalized reference velocity perturbation and $\mathcal{F}$ is the flame transfer function. In order to keep the basic TAX structure, we assume that the adjoint heat release can be described in terms of the original flame transfer function with a negative time delay $Q^{\dagger}_{\text{norm}} = \mathcal{F}(\tau)^{\dagger} u^{\dagger}_{\text{ref,norm}} = \mathcal{F}(-\tau) u^{\dagger}_{\text{ref,norm}}$. This assumption holds for any time delay transfer function, i.e., the proposed approach may be applied to more complex flame transfer function (FTFs), including ones based on the finite impulse response $\mathcal{F} = \sum_k h_k e^{-ik\delta t}$ [12,13], as integration by parts does not affect the flame shape (*cf.* Ref. [2]). The negative time delay indicates that the system is anticausal, which is a known characteristic of adjoint models [4] as the adjoint system evolves backward in time. We now need to determine the adjoint scattering matrix and reference velocity perturbation $u^{\dagger}_{\text{ref}}$, such that we obtain the associated adjoint flame element. The reference velocity perturbation of the direct system equals the velocity perturbation at the flame hold, therefore, we replace it with $u'_{\text{ref}} = u'_u = f_u - g_u$. With this relation, Eq. (25) can be rewritten into the burner scattering matrix. After determining the corresponding adjoint scattering matrix according to Eq. (24), we retransform the system into the original representation, where $u^{\dagger}_{\text{norm}}$ follows from the coefficients of the FTF as:

$$u^{\dagger}_{\text{ref,norm}} = (S_{12}S_{23} - S_{13}S_{22})\bar{\rho}_d(\bar{c}_d + \bar{u}_d) f_d^{\dagger} + S_{13}\bar{\rho}_d(\bar{c}_d - \bar{u}_d) g_d^{\dagger} \tag{27}$$

This indicates that the adjoint flame responds to perturbation *downstream* of the flame due to the adjoint system developing backward in time. The adjoint element results as

$$\begin{bmatrix} g_u^{\dagger} \\ f_d^{\dagger} \end{bmatrix} = \begin{bmatrix} S_{11}^{\dagger} & S_{21}^{\dagger} & -\dfrac{S_{22} - S_{11}S_{22} + S_{12}S_{21}}{\det(S_{ac})S_{12}\bar{\rho}_u\bar{u}_u(\bar{c}_u - \bar{u}_u)} \\ S_{21}^{\dagger} & S_{22}^{\dagger} & \dfrac{1}{\det(S_{ac})\bar{\rho}_d\bar{u}_u(\bar{c}_d + \bar{u}_d)} \end{bmatrix} \begin{bmatrix} f_u^{\dagger} \\ g_d^{\dagger} \\ Q^{\dagger}_{\text{norm}} \end{bmatrix} \tag{28}$$

where $S^{\dagger}$ is the adjoint scattering matrix as defined in Eq. (24), and $\det(S_{ac}) = S_{11}S_{22} - S_{12}S_{21}$ is the determinant of the acoustic scattering matrix.

Advantages of the Hybrid Adjoint Approach

The main advantage of the HA approach compared to the CA approach is the significant reduction of implementation effort. For the CA approach, the adjoint equations have to be derived and implemented for each element of the network model. The HA approach, on the other hand, merely requires the (one-time) derivation of the adjoint equations of the duct element, as shown above. Furthermore, as the duct itself is a self-adjoint element, the adjoint duct element is equal to the direct one, eliminating the need to add any element to the model library. The adjoint system via the HA approach is, thus, obtained by simply rewriting the scattering matrices of the compact elements. For this, the original software does not have to be manipulated or extended—the transformation of the original into the adjoint system can be executed via a single separate script. Afterward, the original software can be used to analyze the modified system, e.g., to calculate the system eigenvalues. In addition, more complex analyses that include the consideration of mean flow or entropy waves do not pose additional challenges, which is a compelling advantage over the CA approach.

The DA approach offers similar advantages regarding implementation effort and flexibility as the HA approach, as it transforms the original system into the adjoint system by simply taking the Hermitian of the system matrix. However, as will be shown next, this transformation accounts for spurious oscillations at the jump and boundary conditions of the adjoint eigenmodes. This may significantly impair the quality and interpretability of the results.

Determination of Base State and Feedback Sensitivities

A major advantage of adjoint design in thermoacoustic systems is its capacity to efficiently determine the system sensitivities. For the entire system, the Lagrangian functional comprises separate Euler equations for each duct element of the system. Boundary terms and jump conditions are included via integration by parts, equivalent to Eq. (16). The Lagrangian for a duct thus follows as:

$$\begin{aligned} \mathcal{L} &= s - \langle \rho^{\dagger} | E_1 \rangle - \langle u^{\dagger} | E_2 \rangle - \langle p^{\dagger} | E_3 \rangle \\ &= s + \left\langle \frac{\partial \rho^{\dagger}}{\partial x} \middle| \int E_1 dx \right\rangle + \left\langle \frac{\partial u^{\dagger}}{\partial x} \middle| \int E_2 dx \right\rangle + \left\langle \frac{\partial p^{\dagger}}{\partial x} \middle| \int E_3 dx \right\rangle \\ &\quad - \left[p' \left(u^{\dagger} + p^{\dagger} \right) + u' \left(\bar{\rho} \bar{c}^2 p^{\dagger} + \bar{\rho} \bar{u} u^{\dagger} \right) + \bar{u} \varsigma' \varsigma^{\dagger} \right]_0^L \end{aligned} \tag{29}$$

where dependencies introduced by the jump conditions appear explicitly via the boundary terms contained within the square brackets. A more detailed derivation is given in Ref. [9]. In order to obtain the correct values for the system sensitivity, we disturb the system by the parameter shift $\xi \rightarrow \xi + \varepsilon\delta\xi$ which yields a shift in the eigenvalue $s \rightarrow s + \delta\varepsilon s$. The perturbation of the Lagrangian $\mathcal{L}(s, \xi)$ follows as:

$$\mathcal{L} + \varepsilon\delta s \frac{\partial \mathcal{L}}{\partial s} + \varepsilon\delta\xi \frac{\partial \mathcal{L}}{\partial \xi} = 0 \tag{30}$$

Considering terms at order ε gives

$$\delta s \frac{\partial \mathcal{L}}{\partial s} + \delta\xi \frac{\partial \mathcal{L}}{\partial \xi} = 0 \tag{31}$$

The normalization condition is given by the first term of the equation

$$\frac{\partial \mathcal{L}}{\partial s} = 0 \tag{32}$$

Base State Sensitivity

The base state sensitivity describes the eigenvalue shift of the base system due to small changes in the system parameters. Thus, by analyzing the base state sensitivity for the most unstable eigenvalue, we can determine influential parameters and how we need to change them in order to stabilize the system. By interpreting the base state sensitivities we may learn the thermoacoustic behavior of a given system. To obtain the base state sensitivity, i.e., the eigenvalue drift for small changes in the base state variables, we determine the first variation of the Lagrangian, which is equal to zero according to Eqs. (31) and (32)

$$\frac{\partial \mathcal{L}}{\partial \xi}\delta\xi = 0 \tag{33}$$

For any base state parameter ξ of a compact element, the base state sensitivity follows from the variation of the corresponding scattering matrix:

$$\begin{aligned}\delta s = &-\bar{p}_d(\bar{c}_d + \bar{u}_d)f_d^{\dagger}\frac{\partial}{\partial \xi}(S_{21}g_d + S_{22}f_u)\delta\xi \\ &+\bar{p}_u(\bar{c}_u - \bar{u}_u)g_u^{\dagger}\frac{\partial}{\partial \xi}(S_{11}g_d + S_{12}f_u)\delta\xi\end{aligned} \tag{34}$$

For the base state variable R_{in}, which is the reflection coefficient at the inlet of the system, the eigenvalue drift results as

$$\begin{aligned}\delta s &= \frac{\partial}{\partial R_{\text{in}}}\left(\left[gg^{\dagger}\bar{p}(\bar{c} - \bar{u}) - ff^{\dagger}\bar{p}(\bar{c} + \bar{u})\right]_0^L\right)\delta R_{\text{in}} \\ &= \rho_0\left((\bar{c}_0 + \bar{u}_0)f_1^{\dagger}g_1 - \frac{1}{R_{\text{in}}^2}(\bar{c}_0 - \bar{u}_0)g_1^{\dagger}f_1\right)\delta R_{\text{in}}\end{aligned} \tag{35}$$

Once the direct and adjoint eigenfunctions have been calculated, the eigenvalue sensitivity can, thus, be determined at almost no expense.

Feedback Sensitivity

The effect of passive devices installed to stabilize thermoacoustic systems may be modeled in terms of their feedback from velocity and/or pressure into the conservation equations [2]. A feedback that is local in both space and time corresponds to a passive control device, whereas nonlocal feedback constitutes active control with a sensor and actuator. In this study, we determine the local feedback sensitivity by perturbing the primary equations, i.e., the perturbation terms in Eq. (2) are nonzero

$$\delta\dot{m} = \delta\dot{m}_u u' + \delta\dot{m}_p p' \tag{36}$$

$$\delta f = \delta f_u u' + \delta f_p p' \tag{37}$$

$$\delta\dot{q} = \delta\dot{q}_u u' + \delta\dot{q}_p p' \tag{38}$$

We assume that this structural perturbation does not affect the base state variables. Following Giannetti and Luchini [14], we assume that the small perturbation causes small perturbations in the acoustic variables and in the eigenvalue

$$\hat{s} = s' + \varepsilon s', \quad \hat{p} = p' + \varepsilon p' \tag{39}$$

$$\hat{u} = u' + \varepsilon u', \quad \hat{\rho} = \rho' + \varepsilon\rho' \tag{40}$$

After neglecting terms of order $\mathcal{O}(\varepsilon^2)$, we can find the eigenvalue drift resulting from the feedback perturbation. For example, perturbing the momentum equation at the position x_0 by a feedback of velocity $\delta f = f_u u'(x)\delta(x - x_0)$ gives

$$\delta s = p^{\dagger}(x_0)f_u u(x_0) \tag{41}$$

Note that the adjoint pressure eigenmode has been previously normalized using Eq. (32). The real part of the feedback sensitivity represents local feedback on the growth rate, thus a negative real part corresponds to a stabilizing effect of the feedback device. Applying this to general perturbations allows us to determine the optimal location for introduction of a feedback perturbation, in order to achieve the maximum reduction in growth rate.

Model Validation

For model validation, we consider a simple Rijke tube as investigated in Ref. [2]. The system is described by a duct of length $L = 1\,\text{m}$ with a heating gauze at the position $x = 0.25\,\text{m}$. The response of the heating gauze is given by the n–τ-model with a time delay of $\tau = 1.5 \times 10^{-3}\text{s}$ and an interaction index of $n = 0.161$. Figure 2 illustrates the structure of the network model.

We compare the results of the HA network model with those presented in Ref. [2] and those obtained by means of the DA approach.

Comparison to an Adjoint Helmholtz Solver

In the study of Juniper [2], the Rijke tube is investigated by means of an adjoint Helmholtz solver. In contrast to our model, Ref. [2] uses the discretized Helmholtz equation to model the system. This accounts for some small deviations as the heat source is not modeled as a discontinuity, but as a continuous function that differs from zero over a small axial range δx. The dominant eigenvalue, equal to $12.8 + 2\pi \times 187.6i\text{Hz}$, is still in good agreement with the eigenvalue in the original study ($9.7 + 2\pi \times 187.8i\text{Hz}$). In Fig. 3, we compare the direct and adjoint mode shapes resulting from TAX to those presented in Ref. [2]. Both the direct and the adjoint mode shapes show good agreement. This shows that the previous derivations presented are correct. The direct and

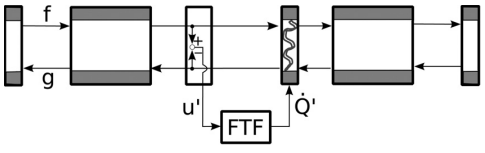

Fig. 2 Model of the Rijke tube, which is used for the validation of the HA model

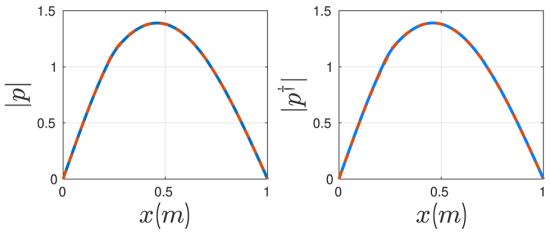

Fig. 3 Adjoint eigenmodes from HA network model versus adjoint Helmholtz solver. Solid line: Results obtained by Juniper [2], dashed line: Results obtained from the proposed HA model.

adjoint mode shapes can be interpreted in terms of the system observability and controllability: large values of the direct mode shape indicate that the system is observable, whereas large values of the adjoint mode shape indicate that the system is controllable [9]. In the next step, we validate our derivations for the feedback sensitivity by comparing our results with those in Ref. [2]. For this purpose, we compare the feedback sensitivity of the system for varying axial positions of the perturbation introduction. Figure 4 shows that the results are in good agreement with only slight deviations due to the difference in modeling the heating gauze.

The real component of the feedback sensitivity gives information about the in-phase feedback on the growth rate, whereas the imaginary component represents the influence on the frequency. Figure 4 shows that if mass injection is in phase with pressure and if momentum injection is in phase with velocity, the system will be destabilized [2]. The introduction of such a feedback perturbation is most influential where the amplitudes in Fig. 4 are largest.

Comparison Hybrid Adjoint and Discrete Adjoint

Another possibility to validate a model based on the continuous adjoint equations is by comparing the results with those obtained by the discrete adjoint. Adding a small perturbation δA to the system matrix A of the linear eigenvalue problem yields Eq. (42) which describes the DA eigenvalue shift

$$\delta s = \frac{\langle q^\dagger \delta A q \rangle}{\langle q^\dagger q \rangle} \tag{42}$$

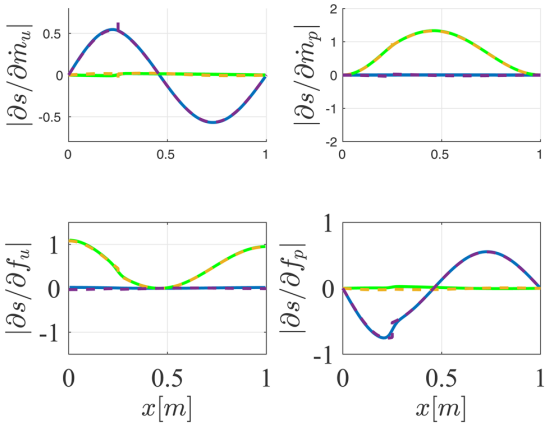

Fig. 4 Feedback sensitivities on frequency (dark) and growth rate (light) from perturbation of the mass and momentum equation. Solid line: Results obtained from the Helmholtz solver as introduced by Juniper [2], dashed line: Results from the proposed HA model.

This expression is valid for both base state and feedback perturbations. However, the determination of the perturbation matrix δA is nontrivial and time-consuming (*cf.* Ref. [9]). In addition, the calculation of the adjoint eigenfunction q from the complex transpose of the system matrix $A^\dagger = A^H$ often leads to nonphysical, high-frequency oscillations at the jump and boundary conditions (e.g., at the inlet and outlet, area or temperature jumps). These are referred to as spurious oscillations. Although this does not impact the computation of the sensitivity, it may impact the physical interpretation of the adjoint mode, as explained in Refs. [2] and [4]. For a simple system such as the Rijke tube considered here, the quality of the DA results is still sufficient to validate our results. Figure 5 shows the gain and phase of the adjoint eigenmodes obtained from the HA and DA modeling. Areas, where spurious oscillations are introduced by the DA approach, are marked with green boxes. With the exception of these oscillations at the inlet, outlet, and the heat source, the results show excellent agreement. However, as the system gets more complex, the oscillations at each jump condition dominate the eigenmode, rendering the DA results unusable. An example of such a system is introduced in the section Optimization of the Plenum, Burners, Chamber Analytical Tool to Analyze and Control Azimuthal Modes in Annular Chambers Combustor, where the system architecture requires a large number of jump conditions, thus resulting in numerous zones of spurious oscillations.

Optimal Tuning of Passive Damping Devices

In gas turbines, Helmholtz resonators are often installed to dampen thermoacoustic instabilities at a specific frequency and thus stabilize the system [15–17]. A resonator consists of a backing volume connected by a neck to the system that is to be damped. The Helmholtz resonator extracts energy from the system through viscous dissipation and vortex shedding at the ends of the small neck. The characteristic of an acoustic resonator is described in terms of its impedance Z in the frequency domain. The reflection coefficient in the wave-based network model is defined as

$$R(\omega) = \frac{g}{f} = \frac{z(\omega) - 1}{z(\omega) + 1} \tag{43}$$

where $z(\omega) = Z(\omega)/(\bar{\rho}\bar{c})$. The application of a Helmholtz resonator in an annular chamber will eliminate the rotational symmetry, resulting in a coupling of the circumferential modes [18]. Effects

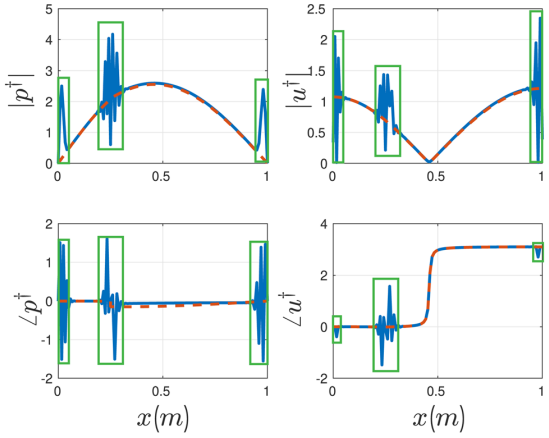

Fig. 5 Comparison of the adjoint eigenmodes obtained from the HA (dashed lines) and DA (solid lined) approach. Boxes mark areas of spurious oscillations introduced by the DA approach.

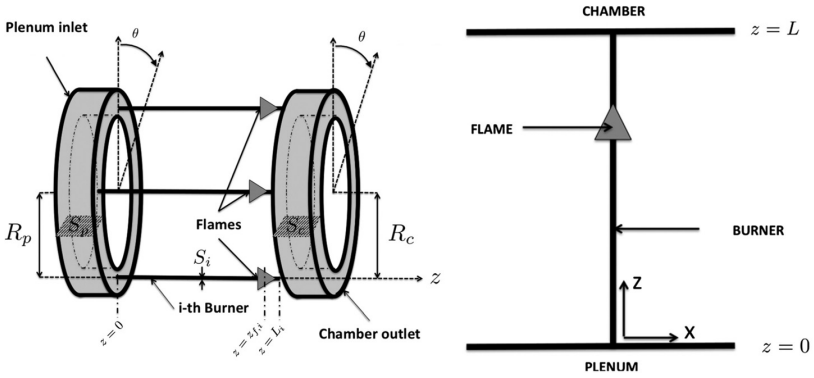

Fig. 6 Left: three dimensional illustration of the PBC combustor reprinted from [20] with permission from Elsevier. Right: representation of an individual burner in the quasi one-dimensional network model.

of the Helmholtz resonator in the mean flow are small and will be neglected [17]. In this study, we want to find the optimal parameters for a damping system consisting of two Helmholtz resonators, i.e., identify the setting at which we achieve the maximum damping of the unstable modes. The primary placement of the Helmholtz resonators follows from the analysis of the feedback sensitivity obtained via the proposed hybrid adjoint model. Subsequently, we gradually adjust the parameters of the resonators using a gradient-based optimization scheme, where the gradients are efficiently calculated using the adjoint formulation. A similar optimization approach based on gradient information obtained from the DA can be found in Ref. [19].

Optimization of the Plenum, Burners, Chamber Combustor

Analytical Tool to Analyze and Control Azimuthal Modes in Annular Chambers

We consider the plenum, burners, chamber (PBC) configuration investigated in Ref. [20], which is an extension of the PB combustor introduced in the study in Ref. [21]. In the PBC combustor, the burners are connected both upstream and downstream to the annular plenum and chamber, respectively. The configuration under investigation has four burners as illustrated in Fig. 6. The network model describes each burner as a duct with a flame, which is connected to the plenum and chamber (see Fig. 6 right). We have adopted the model parameters listed in Table 1 of Ref. [20], with a time delay at the flame of $\tau = 1.67 \times 10^{-3} s$. We further include the corrections proposed therein to capture three-dimensional effects in the quasi one-dimensional network model. The flame is positioned at $z = 0.88L$, where L is the length of the burners. The eigenvalues of our network model are in good agreement with Ref. [20] with a maximum deviation of 2% in frequency and small overestimations of the growth rates by approximately 35% for the considered setting. We consider the first two chamber modes C1 at $s = 94 \times 2\pi i + 15.9Hz$ and C2 at $s = 181.1 \times 2\pi i + 16Hz$. Both eigenvalues have positive growth rates for the selected configurations, i.e., they are unstable. Our goal is to find an optimal configuration of a system of passive devices, such that the two eigenmodes are stabilized. However, installing a single Helmholtz resonator has no damping effect, as the initially weakly coupled circumferential C1 modes become coupled resulting in a standing wave with a pressure node at the position of the resonator. Thus, at least two resonators must be used [18]. The direct and adjoint mode shapes of the selected C1 and C2 modes and the corresponding feedback sensitivities are shown in Figs. 7 and 8. Note that, although the direct and adjoint eigenmodes match perfectly within the chamber, the eigenmodes are not self-adjoint, as they

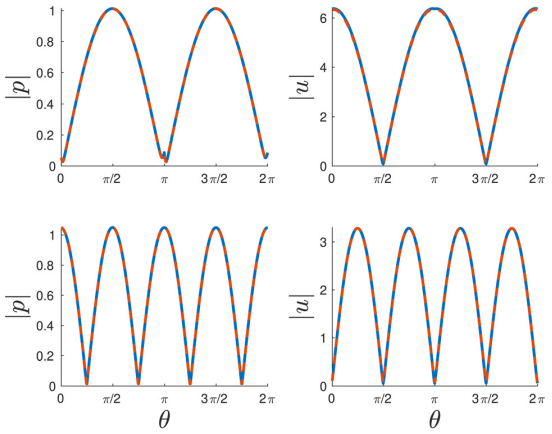

Fig. 7 Direct (solid line) and adjoint (dashed line) mode shaped of C1 (top) and C2 (bottom) chamber modes for the PBC4 configuration calculated via HA approach

deviate from each other outside of the chamber. We place the first resonator at $\theta = 0$, where the feedback sensitivity of the growth rate of the C2 mode is at a maximum, and a second resonator at $\theta = \pi/4$, which meets the positioning rule introduced in Ref. [18] to evenly distribute the resonators along half the wavelength of the degenerate eigenmode (in this case C1).

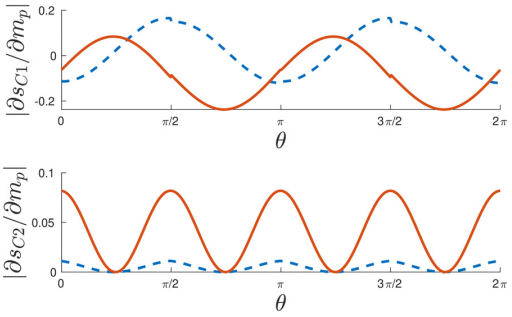

Fig. 8 Feedback sensitivity to an introduction of mass perturbations for the C1 (first row) and C2 (second row) eigenmodes. Solid: sensitivity of the frequency, dashed: Sensitivity of the growth rate.

Optimal Design of the Helmholtz Resonators

We model the Helmholtz resonators in terms of their impedance. The simplified model, originally proposed by Nicoud et al. [22], uses three impedance parameters ζ_0, ζ_1, and ζ_2 to express the impedance of the resonator

$$\frac{1}{Z} = \zeta_o \frac{i}{\omega} + \zeta_1 + \zeta_2 i\omega \tag{44}$$

This reduced impedance model has also been applied in Ref. [6]. In order to include the resonator impedance into the network model, we add the corresponding reflection coefficient to the system as given by Eq. (43). Subsequently, we use the sensitivity obtained from the adjoint system to determine the gradient of the eigenvalue with respect to the impedance parameters. We define the objective function as the larger growth rate of the two eigenvalues

$$\mathbf{J} = \max(\mathcal{R}(s_{C1}, s_{C2})) \tag{45}$$

This ensures that the optimization algorithm does not result in destabilizing the C_2 mode as C_1 is stabilized. Subsequently, the parameters of the two Helmholtz resonators are adjusted via a simple gradient decent algorithm

$$\zeta_{i,n+1} = \zeta_{i,n} - \gamma \nabla \mathbf{J} \tag{46}$$

where γ is a control parameter for the step size.

The gradient of the objective function with respect to the resonator parameters can be derived from the sensitivity with respect to the reflection coefficient R_j representing resonator j according to

$$\frac{\partial \mathbf{J}}{\partial \zeta_{j,i}} = \frac{\partial \mathbf{J}}{\partial R_j} \frac{\partial R_j}{\partial Z_j} \frac{\partial Z_j}{\partial \zeta_{j,i}}, \quad i = 0, 1, 2 \quad j = 1, 2 \tag{47}$$

where $\frac{\partial R_j}{\partial Z_j}$ and $\frac{\partial Z_j}{\partial \zeta_{j,i}}$ can be determined analytically from Eqs. (43) and (44). The derivative of the objective function $\frac{\partial \mathbf{J}}{\partial R_j}$ follows as the real part of the eigenvalue sensitivity to changes in the reflection coefficient $\mathcal{R}(\frac{\partial s^*}{\partial R_j})$, where s^* is the eigenvalue with the larger growth rate. Consequently, for two resonators, the adjoint method is not necessarily needed, as only two sensitivities need to be determined in each iteration. However, a comparison of run times shows that the more accurate and efficient determination of the adjoint gradient decreases the optimization run time by more than 60% compared to a finite difference approach. Furthermore, increasing the number of parameters, e.g., by adding more resonators to the system would not add any difficulty nor significantly increase the computational cost. Figure 9 shows the development of the growth rates of the two eigenvalues over the iterations of the solver. We see that the system growth rates decrease steadily as we adapt the parameters of our resonators and stabilize after 8 iterations. This means we have successfully optimized the resonator parameters.

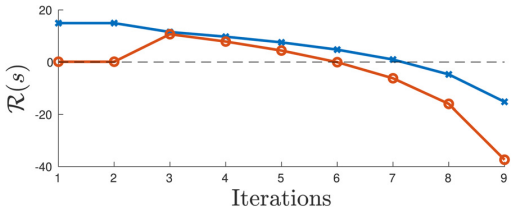

Fig. 9 Optimization of the annular combustor. Eigenvalue growth rates of C1 (cross markers) and C2 (circles) over the iterations of the solver.

Conclusion

We presented a hybrid approach to extend an existing thermoacoustic network model tool by the functionality of calculating the adjoint equivalent to any given network model. We eliminate the necessity to derive new jump and boundary conditions for each element of the original network model by transforming the original scattering matrices into the adjoint scattering matrices. The transformation scheme is derived from the boundary terms of the adjoint duct equations, which result from the partial integration of the direct equations. Subsequently, we showed how to derive the base state and feedback sensitivity of a generic network model, given the adjoint system. The adjoint variables and sensitivities give additional insight into the physics of the model. Moreover, the calculation of the eigenvalue sensitivity with respect to all variables allows the implementation of systematic optimization strategies with decreased computational effort and improved gradient accuracy compared to conventional procedures. We validated the proposed approach against the continuous adjoint Helmholtz solver and the discrete adjoint, both applied to a simple Rijke tube system. The mode shapes and feedback sensitivity are in excellent agreement, demonstrating that the presented approach delivers reliable results. Moreover, the comparison with the discrete adjoint illustrates some of the disadvantages of the discrete adjoint applied to an existing network model software, as spurious oscillations at the jump and boundary conditions aggravate the interpretation of the results. Finally, we applied the hybrid adjoint network model to a generic annular combustor test case, consisting of a plenum, four burners, and the chamber. We demonstrated how the information obtained from the adjoint system may be used to tune the parameters of passive damping devices. We conclude that the proposed method presents a favorable solution for the integration of adjoints into network model tools as it delivers satisfying results while requiring little effort in the derivation and implementation of the adjoint system.

Acknowledgment

The authors acknowledge the support of the Technical University of Munich—Institute for Advanced Study, funded by the German Excellence Initiative and the European Union Seventh Framework Programme undergrant agreement no. 291763. L.M. also acknowledges the Royal Academy of Engineering Research Fellow-ship Scheme.

Funding Data

- Royal Academy of Engineering (Funder ID: 10.13039/501100000287).
- Seventh Framework Programme (Grant No. 291763; Funder ID: 10.13039/501100004963).

Nomenclature

A = system matrix in tax
c = sound speed
CA = continuous adjoint
DA = discrete adjoint
f, g = characteristic amplitude of plane wave propagating in $\pm x$ direction
FTF = flame transfer function
h_i = FIR model coefficient
HA = hybrid adjoint
p = pressure
R_{in} = reflection coefficient at combustor inlet
s = Eigenvalue, Laplace variable
S = scattering matrix
u = flow velocity
γ = ratio of heat capacities
δf = feedback perturbation force

δm = feedback perturbation mass
$\delta \dot{q}$ = feedback perturbation heat release
ρ = fluid density
σ = modal growth rate
τ = time delay in the flame transfer function
ω = frequency
ς = normalized entropy wave
$()^{\dagger}$ = adjoint variable
$\overline{()}$ = time average of the variable
$()'$ = small fluctuation
$\dot{Q}$ = heat release at the flame

References

[1] Poinsot, T., and Veynante, D., 2005, *Theoretical and Numerical Combustion*, RT Edwards, Philadelphia, PA.
[2] Juniper, M. P., 2018, "Sensitivity Analysis of Thermoacoustic Instability With Adjoint Helmholtz Solvers," Phys. Rev. Fluids, **3**(11), p. 110509.
[3] Juniper, M. P., and Sujith, R. I., 2018, "Sensitivity and Nonlinearity of Thermoacoustic Oscillations," Annu. Rev. Fluid Mech., **50**(1), pp. 661–689.
[4] Magri, L., 2019, "Adjoint Methods as Design Tools in Thermoacoustics," ASME Appl. Mech. Rev., **71**(2), p. 020801.
[5] Magri, L., and Juniper, M. P., 2013, "Sensitivity Analysis of a Time-Delayed Thermo-Acoustic System Via an Adjoint-Based Approach," J. Fluid Mech., **719**, pp. 183–202.
[6] Mensah, G. A., and Moeck, J. P., 2017, "Acoustic Damper Placement and Tuning for Annular Combustors: An Adjoint-Based Optimization Study," ASME J. Eng. Gas Turbines Power, **139**(6), p. 061501.
[7] Silva, C., Runte, T., Polifke, W., and Magri, L., 2016, "Uncertainty Quantification of Growth Rates of Thermoacoustic Instability by an Adjoint Helmholtz Solver," ASME Paper No. GT2016-57659.
[8] Magri, L., Bauerheim, M., Nicoud, F., and Juniper, M. P., 2016, "Stability Analysis of Thermo-Acoustic Nonlinear Eigenproblems in Annular Combustors. Part II. Uncertainty Quantification," J. Comput. Phys., **325**, pp. 411–421.
[9] Aguilar, J. G., Magri, L., and Juniper, M. P., 2017, "Adjoint-Based Sensitivity Analysis of Low-Order Thermoacoustic Networks Using a Wave-Based Approach," J. Comput. Phys., **341**, pp. 163–181.
[10] Emmert, T., Meindl, M., Jaensch, S., and Polifke, W., 2016, "Linear State Space Interconnect Modeling of Acoustic Systems," Acta Acust. United Acust., **102**(5), pp. 824–833.
[11] Emmert, T., 2016, "State Space Modeling of Thermoacoustic Systems with Application to Intrinsic Feedback," Ph.D. thesis, TU München, München, Germany.
[12] Polifke, W., 2014, "Black-Box System Identification for Reduced Order Model Construction," Ann. Nucl. Energy, **67**, pp. 109–128.
[13] Polifke, W., 2020, "Modeling and Analysis of Premixed Flame Dynamics by Means of Distributed Time Delays," Prog. Energy Combust. Sci., **79**, p. 100845.
[14] Giannetti, F., and Luchini, P., 2007, "Structural Sensitivity of the First Instability of the Cylinder Wake," J. Fluid Mech., **581**, pp. 167–197.
[15] Bellucci, V., Flohr, P., Paschereit, C. O., and Magni, F., 2004, "On the Use of Helmholtz Resonators for Damping Acoustic Pulsations in Industrial Gas Turbines," ASME J. Eng. Gas Turbines Power, **126**(2), pp. 271–275.
[16] Bellucci, V., Schuermans, B., Nowak, D., Flohr, P., and Paschereit, C. O., 2005, "Thermoacoustic Modeling of a Gas Turbine Combustor Equipped With Acoustic Dampers," ASME J. Turbomach., **127**(2), pp. 372–379.
[17] Bothien, M. R., Noiray, N., and Schuermans, B., 2013, "A Novel Damping Device for Broadband Attenuation of Low-Frequency Combustion Pulsations in Gas Turbines," ASME J. Eng. Gas Turbines Power, **136**(4), p. 041504.
[18] Stow, S. R., and Dowling, A. P., 2003, "Modelling of Circumferential Modal Coupling Due to Helmholtz Resonators," ASME Paper No. GT2003-38168.
[19] Yang, D., Sogaro, F. M., Morgans, A. S., and Schmid, P. J., 2019, "Optimising the Acoustic Damping of Multiple Helmholtz Resonators Attached to a Thin Annular Duct," J. Sound Vib., **444**, pp. 69–84.
[20] Bauerheim, M., Parmentier, J.-F., Salas, P., Nicoud, F., and Poinsot, T., 2014, "An Analytical Model for Azimuthal Thermoacoustic Modes in an Annular Chamber Fed by an Annular Plenum," Combust. Flame, **161**(5), pp. 1374–1389.
[21] Parmentier, J.-F., Salas, P., Wolf, P., Staffelbach, G., Nicoud, F., and Poinsot, T., 2012, "A Simple Analytical Model to Study and Control Azimuthal Instabilities in Annular Combustion Chambers," Combust. Flame, **159**(7), pp. 2374–2387.
[22] Nicoud, F., Benoit, L., Sensiau, C., and Poinsot, T., 2007, "Acoustic Modes in Combustors With Complex Impedances and Multidimensional Active Flames," AIAA J., **45**(2), pp. 426–441.

The Impact of Exceptional Points on the Reliability of Thermoacoustic Stability Analysis

Felicitas Schaefer[1]
Department of Mechanical Engineering,
Technical University of Munich,
Garching 85748, Germany
e-mail: schaefer@tfd.mw.tum.de

Shuai Guo
Department of Mechanical Engineering,
Technical University of Munich,
Garching 85748, Germany

Wolfgang Polifke
Department of Mechanical Engineering,
Technical University of Munich,
Garching 85748, Germany

Exceptional points can be found for specific sets of parameters in thermoacoustic systems. At an exceptional point, two eigenvalues and their corresponding eigenfunctions coalesce. Given that the sensitivity of these eigenvalues to parameter changes becomes infinite at the exceptional point, their occurrence may greatly affect the outcome and reliability of numerical stability analysis. We propose a new method to identify exceptional points in thermoacoustic systems. By iteratively updating the system parameters, two initially selected eigenvalues are shifted toward each other, ultimately colliding and generating the exceptional point. Using this algorithm, we were able to identify for the first time a physically meaningful exceptional point with positive growth rate in a thermoacoustic model. Furthermore, our analysis goes beyond previous studies inasmuch as we employ a more realistic flame transfer function to model flame dynamics. Building on these results, we analyze the effect of exceptional points on the reliability of thermoacoustic stability analysis. In the context of uncertainty quantification, we show that surrogate modeling is not reliable in the vicinity of an exceptional point, even when large sets of training samples are provided. The impact of exceptional points on the propagation of input uncertainties is demonstrated via Monte Carlo computations. The increased sensitivity associated with the exceptional point results in large variances for eigenvalue predictions, which needs to be taken into account for reliable stability analysis.
[DOI: 10.1115/1.4049351]

Introduction

In response to strict emission regulations, lean, premixed combustion techniques have become prevalent in gas turbines. Unfortunately, engines operating at these conditions are more susceptible to thermoacoustic instabilities, a phenomenon manifesting itself as large-amplitude pressure oscillations. This may affect engine emissions, reduce the life-spans, or even cause structural damage to the engine [1]. In consequence, thermoacoustic instabilities are a major concern in the development of modern gas turbine combustors and need to be incorporated into the design process. This turns out to be particularly problematic as these systems are very sensitive to a large number of parameters [2]. In addition, these parameters are always subject to uncertainties, i.e., the operational conditions deviate from the nominal condition due to stochastic fluctuations. As a result, a system that has been predicted to be stable for nominal parameter settings may, in fact, become unstable as the parameters deviate from their nominal values. It is thus essential to include parameter uncertainties in the process of stability analysis.

Parameter sensitivities and the resulting prediction uncertainties may even be enhanced for specific parameter settings, due to the existence of so-called exceptional points (XPs). XPs are often referred to as "branch point singularities," as they originate from the coalescence of at least two eigenvalues and their corresponding eigenfunction [3]. In general, they can be found for parameter-dependent, non-Hermitian eigenvalue problems [4,5]. Their occurrence is associated with unusual physical behavior and has been studied in several scientific fields such as mechanics, electromagnetism and quantum physics [5]. Although they have only recently been identified in thermoacoustic systems [6], understanding their impact on thermoacoustic instability may be crucial to the design for thermoacoustic stability.

In the context of thermoacoustics, XPs are primarily attributed to the interplay between intrinsic thermoacoustic modes (ITA) and acoustic modes [6], i.e., thermoacoustic modes of different nature.[2] In this study, we employ a network model to identify XPs and analyze their impact on the propagation of input uncertainties. In contrast to prior studies [6,7], the flame transfer function (FTF) of our model is based on a finite impulse response (FIR), a formulation that is capable of describing realistic flame dynamics.

A characteristic feature of XPs is the infinite sensitivity to parameter changes that can be observed for the corresponding eigenvalues. As a result, eigenvalues approaching an XP are subject to sudden shifts in sensitivity, entailing strongly varying responses to parameter changes [7]. This may be critical to the analysis and control of stability, since changes to a parameter may first stabilize, but ultimately destabilize an eigenvalue. On the other hand, the unusual physical behavior at the exceptional point may be exploited to stabilize the system. For example, Bourquard and Noiray [8] experimentally and analytically studied a tunable damping system that features an XP for a specific setting of the purge mass flow, showing that stabilization is most effective at the exceptional point.

In a recent study, Orchini et al. [7] proposed a method to identify exceptional points based on the infinite parameter sensitivity. They chose a simple n-τ- model to represent the dynamics of the flame. One objective of this paper is to find a way to identify XPs for a more realistic flame model. Furthermore, we aim to find combustor configurations that feature one or more physically meaningful, *unstable* XP, a phenomenon that has not been

[1]Corresponding author.

Manuscript received September 3, 2020; final manuscript received September 15, 2020; published online January 18, 2021. Editor: Jerzy T. Sawicki.

[2]Note, however, that Orchini et al. showed that combustors may also feature acoustic-acoustic XPs. Exceptional points formed from two ITA modes have not been observed so far, but this possibility cannot be excluded.

observed so far. Identifying such XPs may be a crucial step for the stabilization of combustors, as the increased sensitivity near the XP may be exploited to change the system behavior by making only small, targeted adjustments to the combustor setting. However, as the parameter sensitivity increases, the variance of these eigenvalue predictions is expected to increase accordingly, possibly impairing the reliability of numerical stability analysis.

Thus, we further study the impact of XPs on uncertainty quantification. Given that thermoacoustic systems are highly complex and susceptible to modifications of a large variety of system parameters, the analysis of uncertainty propagation by means of Monte Carlo computation, which requires a large number of system evaluations, can become very expensive. In consequence, a number of tools have been proposed, to efficiently conduct uncertainty quantification. A common approach is to use surrogate models that replicate the system response over a range of input variables with significantly reduced computational effort. Techniques to identify these models are, for example, analytical derivations [9], adjoint analysis [10–12], regression techniques (in combination with Active Subspace) [13], or polynomial chaos expansion [14,15].

In a recent publication, Guo et al. [16] employed Gaussian process (GP) modeling, a machine learning technique designed to train highly accurate surrogate models, and was able to successfully predict probability density functions (PDFs) and extract risk factors for different eigenvalues. Based on the general framework set in that study, we elaborate the limits of surrogate modeling and analyze the probability distribution in the vicinity of exceptional points.

We stress that, although our considerations are restricted to a one-dimensional combustor model, the proposed methodology and general observations are generally valid and can be adapted without essential difficulty for more detailed modeling techniques, e.g., three-dimensional Helmholtz equation, linearized Navier Stokes Equations, etc.

The paper is structured as follows: In the section Thermoacoustic Framework, we introduce the investigated combustor configuration and the modeling of the flame dynamics. In section "Exceptional Points in Thermoacoustic Systems," we propose a method to identify exceptional points, which is based on finding a parameter setting, for which two selected eigenvalues coincide. In section "The Impact of Exceptional Points on Uncertainty Quantification," we first elaborate how the accuracy of surrogate models can be corrupted by the presence of an XP. Second, we analyze the propagation of input uncertainties at the exceptional point. The last section concludes the findings of this paper.

Thermoacoustic Framework

In this section, we introduce the model formulation and layout, including the modeling of the flame dynamics. A one-dimensional network model is employed to calculate the thermoacoustic modes. We consider a perfectly premixed methane–air mixture with an equivalence ratio of 0.77 and a thermal power of 30 kW.

Combustor Model. For this study, a premixed swirl combustor, commonly known as BRS Combustor [17], is considered. This configuration includes a plenum, a duct section with an axial swirler, and the combustion chamber. All calculations are conducted using the low-order network modeling tool *taX* [18] Software available at following weblink in the footnote.[3] An illustration of the network model representing the BRS burner test rig is given in Fig. 1. Geometrical and material parameters have been adopted from Guo et al. [9], with the exception of the lengths of the plenum, swirler tube and combustion chamber, which are set to $L_P = 0.8\,\text{m}$, $L_{ST} = 0.15\,\text{m}$, and $L_{CC} = 1.8\,\text{m}$, respectively. For the detection of the unstable XP, the Mach number in the burner tube is set to Ma = 0.1. The acoustic losses at the first and second area change are modeled via the loss coefficients $\zeta_1 = 0.8$ and $\zeta_2 = 1.7$, respectively (*cf.* Ref. [19]). The swirler is assumed to be acoustically transparent.

Flame Model. The flame dynamics are embedded in the system by means of a FTF. The flame response is thus described in terms of heat release rate Q' to an excitation by velocity fluctuations u'

$$F(\omega) = \frac{Q'/\bar{Q}}{u'/\bar{u}} \tag{1}$$

where Q' and u' are each normalized with their respective mean value ().

For linear, time-invariant systems, the transfer function is fully described by the unit impulse response h, which defines the response r of a system to any signal s as a convolution over previous inputs

$$r_l = \sum_{k=-\infty}^{+\infty} h_k s_{l-k} \tag{2}$$

Assuming a causal system behavior (i.e., the response does only depend on past and present values of the input signal, $h_k = 0$ for $k < 0$,) it suffices to consider impulse response coefficients h_k for $k \geq 0$. In principle, the unit impulse response requires an infinite number of coefficients. In practice the flame response $F(\omega)$ can be approximated as the z-transform of a FIR, which is equal to the FIR to the input signal $s_l = e^{i\omega\Delta t l}$ [20]

$$F(\omega) \approx \sum_{k=0}^{M} h_k e^{-i\omega\Delta t k} \tag{3}$$

where M is the number of FIR coefficients and Δt the sample time.

In this study, we employ a swirl flame FIR for the BRS combustor, which is based on the distributed time lag model derived by Komarek and Polifke [17]. The model comprises various Gaussian distributions of time lags to represent the respective effects of fluctuations in swirl number and axial velocity on the flame dynamics. The FIR coefficients are thus defined as a function of mean time lags τ and their standard deviations σ. The original considerations of Komarek and Polifke [17] were later corroborated by Oberleithner and Paschereit [21].

Following the adaption made by Guo et al. [16], we define the coefficients of the FIR as an explicit function of the convective time lag τ_c, which can be interpreted as the time needed for an inertial wave to propagate from the swirl generator to the flame base [22]. τ_c is directly related to the position of the swirler. As shown in Komarek and Polifke [17], changing the swirler position has no impact on the mean flame shape. τ_c can, therefore, be defined as a control parameter for system stability. Moreover, the model introduced by Guo et al. [16] allows the introduction of uncertainty to the flame parameters without disrupting the continuous shape of the flame FIR.

The resulting flame model is fully specified by the model parameters $\tau_c, \tau_u, \sigma_u, \tau_{s1}$, and τ_{s2}, where τ_u represents the time lag

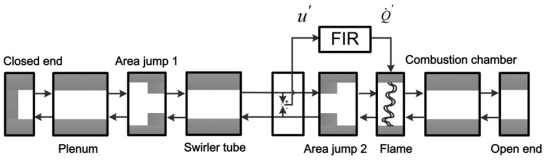

Fig. 1 Network model representation of the BRS combustor

[3] http://gitlab.lrz.de/tfd/tax

of the flame response to axial velocity perturbation with σ_u being its standard deviation, and τ_{s1} and τ_{s2} represent the time lags to swirl perturbations with positive and negative associated Gaussian functions, respectively. The standard deviations σ_{s1} and σ_{s2} of the swirl perturbation time lags can be expressed via the corresponding time lags.

The coefficients of the FIR are thus given by

$$h_k = \frac{\Delta t}{\sigma_u\sqrt{2\pi}} e^{-\frac{(k\Delta t-\tau_u)^2}{2\sigma_u^2}} + \frac{\Delta t}{\sigma_2\sqrt{2\pi}} e^{-\frac{(k\Delta t-\tau_2)^2}{2\sigma_2^2}} - \frac{\Delta t}{\sigma_3\sqrt{2\pi}} e^{-\frac{(k\Delta t-\tau_3)^2}{2\sigma_3^2}} \quad k \in [1,2,\ldots M] \tag{4}$$

where

$$\tau_2 = \tau_c + \tau_{s1}, \quad \tau_3 = \tau_c + \tau_{s2} \qquad \sigma_2 = \tau_{s1}/3, \quad \sigma_3 = \tau_{s2}/3 \tag{5}$$

Figure 2 shows the gain and phase of two exemplary FTFs for changing values of τ_c.

The network tool taX relies on a state space formalism, i.e., the system equations for each element in the network model relate the input u and the output y as

$$\dot{x} = \tilde{A}x + \tilde{B}u \tag{6}$$

$$y = \tilde{C}x + \tilde{D}u \tag{7}$$

where x is the state vector and $\tilde{A},\tilde{B},\tilde{C},\tilde{D}$ the element matrices. For the flame element, we obtain the discrete state space formalism directly from the FTF, and subsequently convert to a continuous system with a bilinear transform. The global system description follows from the global system matrices A,B,C,D, which are obtained by interconnecting the individual element matrices (a more detailed description is given in Ref. [18]). The resulting linear eigenvalue problem fully describes the system dynamics

$$(Is - A)q = 0 \tag{8}$$

where the Laplace variable s represents the eigenvalue and $q = \mathcal{L}\{x\}$ the associated eigenfunction.

Exceptional Points in Thermoacoustic Systems

This section introduces the mathematical background of XPs and the associated system properties. Subsequently, we propose a new method to identify XPs in thermoacoustic systems. We extend the study conducted by Orchini et al. [7], as the flame is no longer modeled by a simplistic n-τ-model, but is represented by a more realistic FIR, as introduced in the previous section. By applying our method to the BRS combustor, we show that unstable XPs can be found for realistic geometrical combustor settings and flame models.

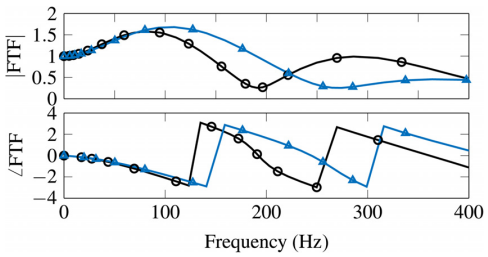

Fig. 2 Flame transfer functions for two different settings of the time lag $\tau_c = 3$ ms (triangle) and $\tau_c = 4$ ms (circle)

Eigenvalue Degeneracy. In order to analyze the stability of a thermoacoustic system, the governing equations are generally formulated as an eigenvalue problem (see, e.g., Ref. [23])

$$L\{s,p\}q = 0 \tag{9}$$

where L is a nonlinear operator matrix in the complex eigenvalue s, p is a vector containing the system parameters and q is the eigenfunction corresponding to s. The eigenvalue can be decomposed into a real and a complex part $s = 2\pi if + \sigma$, where f is the frequency and σ is the growth rate. A system is rendered linearly unstable, if it features eigenvalues with positive growth rate $\sigma > 0$.

If s is a multiple root solution of Eq. (9), it is referred to as degenerate eigenvalue. Different types of degeneracy can be categorized in terms of the algebraic and geometric multiplicity a and g of the eigenvalue. The algebraic multiplicity quantifies the eigenvalue multiplicity as a root of the characteristic polynomial, whereas the geometric multiplicity is the dimension of the eigenspace of s, i.e., the number of linearly independent eigenvectors associated with s. Eigenvalues where $a = g = 1$ are called nondegenerate or simple.

For semisimple eigenvalues, the algebraic multiplicity is equal to the geometric multiplicity $a = g$, with $a, g > 1$. In the context of thermoacoustic stability analysis, this type of degeneracy often occurs in rotationally (discrete) symmetric combustor geometries, such as annular and can-annular combustors.

Exceptional points differ from semisimple eigenvalues, as not only the eigenvalues but also their associated eigenfunctions coincide, , i.e., $a > g$. This type of eigenvalue is generally referred to as defective. In this study we consider an algebraic multiplicity of $a = 2$ and a geometric one of $g = 1$, i.e., two eigenvalues coalesce at the XP.

Self-Orthogonality and Sensitivity. For the following derivation of the adjoint formulations, we apply the Hermitian form of the inner product of two vectors v_1 and v_2:

$$\langle v_1|v_2\rangle = v_1^H v_2 \tag{10}$$

where v_1^H denotes the complex transpose of v_1. Using this definition, we premultiply Eq. (9) by a test function $q^\dagger$

$$\langle q^\dagger|L\{s,p\}q\rangle = 0 \tag{11}$$

If Eq. (11) is satisfied for arbitrary functions q, $q^\dagger$ is called the left, or adjoint, eigenfunction [23]. The direct and adjoint eigenfunctions form a bi-orthogonal basis [24,25]

$$\langle {q_i}^\dagger|q_j\rangle = 0, \quad \text{for } i \neq j \tag{12}$$

At the XP, two eigenvalues s_1^* and s_2^* and their corresponding eigenfunctions q_1^* and q_2^* coalesce. From Eq. (12), which must hold for both defective eigenvalues, it follows that:

$$\langle {q^*}^\dagger|q^*\rangle = 0 \tag{13}$$

This relation, known as self-orthogonality, is a characteristic property of the XP.

Following the mathematical procedure illustrated in Ref. [10] the sensitivity of an eigenvalue s_i with regard to changes in the parameter p_j can be determined by:

$$\frac{\partial s_i}{\partial p_j} = -\frac{\left\langle q_i^\dagger \middle| \frac{\partial L}{\partial p_j} q_i \right\rangle}{\left\langle q_i^\dagger \middle| \frac{\partial L}{\partial s_i} q_i \right\rangle} \tag{14}$$

At the XP the sensitivity with regard to parameter changes is infinitely large. This may be exploited for stabilization of thermoacoustic systems [6]. However, it may also increase the variance of eigenvalue predictions and needs to be taken into account accordingly for the stability analysis of thermoacoustic systems.

Identification of Exceptional Points. Exceptional points can be found for specific values of two real" design" parameters for non-Hermitian system operators [3,5]. Orchini et al. [7] derived a method to identify an XP and the corresponding parameter setting by exploiting the property of infinite sensitivity. Using Eq. (14), they solve a root problem by setting the inverse of the sensitivity to the FTF parameters n and τ to zero. This approach, while being straightforward, requires a well-informed initial guess and can be computationally costly. A second property that can be exploited in order to identify the exceptional point, is that multiple (in our case two) eigenvalues coalesce for specific values of the design parameters.

As design parameters, we select the time lag τ_c which determines the FIR and the reflection coefficient at the chamber exit R_{out}. In practice, τ_c can be modified by changing the position of the swirler [17], whereas damping devices or the turbine working condition directly affect the value of R_{out} [1].

Starting from a fixed parameter setting, we choose two initial eigenvalues $s_{A,0}$ and $s_{B,0}$. The objective is to find values for τ_c^* and R_{out}^*, for which we find the XP s^* formed from the eigenvalues $s_{A,0}$ and $s_{B,0}$. The initial eigenvalues can be selected at random, e.g., by solving for the closest two eigenvalues to an initially guessed XP. However, as some eigenvalues may not coalesce for any setting of the design parameters, it may be advantageous to select $s_{A,0}$, and $s_{B,0}$ based on prior investigations of the thermoacoustic system.

If there exists, in fact, an exceptional point, originating from the coalescence of the two eigenvalues, its value may be approximated as the arithmetic mean of $s_{A,0}$ and $s_{B,0}$. Even for strongly veered mode branches around the exceptional point, the resulting estimation approaches the actual value of the XP in at least one direction of the complex plane (i.e., frequency and growth rate). In addition, as s_A and s_B approach the actual XP, the estimation of *both* frequency and growth rate is improved in each iteration. This

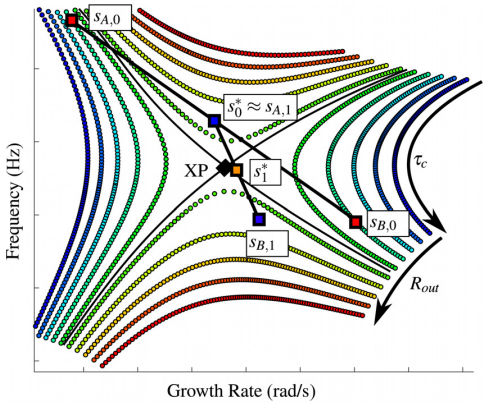

Fig. 3 Exemplary illustration of the first two iterations of our method: Initial eigenvalues ($s_{A,0}$ and $s_{B,0}$), eigenvalues of second iteration ($s_{A,1}$ and $s_{B,1}$) and the corresponding guessed location of the exceptional point (s_1^*)

is because the two eigenvalue branches are orthogonal to each other at the XP [7]; hence, both growth rate and frequency of the XP are found within the interval enclosed by the two eigenvalues, as stated by the intermediate value theorem (see Fig. 3).

We thus define the arithmetic mean of the two initial eigenvalues as our first approximation of the XP s_0^*. Subsequently, we have to determine the real-valued parameters $\tau_{c,0}^*$ and $R_{\text{out},0}^*$ corresponding to the eigenvalue s_0^*. However, this problem is generally ill-posed and cannot be solved by means of standard numerical methods.

We therefore define an objective function, representing the squared distance between a known eigenvalue and the expected XP s_0^*

$$J(\tau_c, R_{\text{out}}) = (s(\tau_c, R_{\text{out}}) - s_0^*)^2 \tag{15}$$

Starting from one of the initial eigenvalues $s_{A,0}$ or $s_{B,0}$, $s(\tau_c, R_{\text{out}})$ is gradually shifted toward s^* by adjusting the values of τ_c and R_{out}. As $s(\tau_c, R_{\text{out}})$ approaches s_0^*, J is minimized. The parameters τ_c and R_{out} are updated iteratively using a gradient-based algorithm, where the gradients are determined by the adjoint formulations

$$\frac{\partial J}{\partial \tau_c} = -2(s - s^*) \frac{\left\langle q^\dagger \middle| \frac{\partial L}{\partial \tau_c} q \right\rangle}{\left\langle q_i^\dagger \middle| \frac{\partial L}{\partial s} q \right\rangle} \tag{16}$$

$$\frac{\partial J}{\partial R_{\text{out}}} = -2(s - s^*) \frac{\left\langle q^\dagger \middle| \frac{\partial L}{\partial R_{\text{out}}} q \right\rangle}{\left\langle q_i^\dagger \middle| \frac{\partial L}{\partial s} q \right\rangle} \tag{17}$$

For the linear eigenvalue system that follows from the state space formalism used in taX, the operator L in Eq. (9) is defined as:

$$L_{\text{taX}}\{s, p\} = A(p) - \text{sI} \tag{18}$$

where $A(p)$ is the system matrix and I denotes the unity matrix. Consequently, the partial derivatives $\frac{\partial L}{\partial \tau_c}$ and $\frac{\partial L}{\partial R_{\text{out}}}$ are directly obtained from the system matrix A. In order to easily derive the gradient information for each iteration, we split A into three matrices

$$A(\tau_c, R_{\text{out}}) = A_0 + A_\tau + A_R \tag{19}$$

such that the operator shifts in Eqs. (16) and (17) can be generalized in terms of two functions f and g, respectively,

$$\frac{\partial L}{\partial \tau_c} = f(\tau_c) A_\tau \tag{20}$$

$$\frac{\partial L}{\partial R_{\text{out}}} = g(R_{\text{out}}) A_R \tag{21}$$

Once the objective function is minimized by optimal values of τ_c and R_{out}, we update the two eigenvalues $s_{A,1}$ and $s_{B,1}$ as the two closest eigenvalues to s_0^*. From these updated eigenvalues, we can get a new approximation of the exceptional point s_1^*, again by taking the arithmetic mean of $s_{A,1}$ and $s_{B,1}$. This procedure is repeated until $s_{A,j}$ and $s_{B,j}$ are sufficiently close to each other

$$|s_{A,j} - s_{B,j}| < \text{tol} \tag{22}$$

where tol defines the truncation tolerance. The value specified for tol determines the accuracy of the identified XP. We were able to detect an XP with an accuracy of $\mathcal{O}(10^{-5})$. A pictorial representation of the procedure is given in Fig. 3, for the first two iterations. It can be seen that the true value of the XP is approached swiftly.

For annular combustor geometries, the proposed method may converge to a semisimple eigenvalue. It is therefore advisable to perform additional checks to ensure that the solution found is in fact an XP. Since we already derived the necessary expressions for the eigenvalue sensitivity with regard to the design parameters, the residual of the root equation proposed by Orchini et al. [7] provides a practical measure

$$\lim_{\tau_c \to \tau_{c*}} r_\tau = \lim_{\tau_c \to \tau_{c*}} \left| \frac{\partial s}{\partial \tau_c} \right|^{-1} = 0 \tag{23}$$

$$\lim_{R_{\text{out}} \to R_{\text{out}*}} r_R = \lim_{R_{\text{out}} \to R_{\text{out}*}} \left| \frac{\partial s}{\partial R_{\text{out}}} \right|^{-1} = 0 \tag{24}$$

This expression exploits the infinite sensitivity at the XP, which is a unique feature of the XP. Equation (24) thus provides sufficient criteria for the defective nature of degeneracy of the converged eigenvalue.

It should be mentioned that both this method and the one proposed by Orchini et al. [7] require the solution of an eigenvalue problem for each iteration. However, the gradient information significantly reduces the number of iterations needed to find an exceptional point. This may greatly reduce the computational cost, especially for more complex models with numerous degrees-of-freedom.

Unstable Exceptional Points. To the authors' knowledge, the XPs identified in prior studies of thermoacoustic combustors were either exclusively stable or associated with unphysical parameter values (e.g., negative time lags). In this section, we use the proposed method to identify XPs for a combustor model where a realistic FTF is applied. We provide first evidence that XPs with positive growth rate exist for realistic parameter settings and can be detected efficiently using the above-introduced algorithm. Although not illustrated in this paper, we were also able to identify unstable, yet physically meaningful XPs using the $n-\tau$-model instead of the FIR, which proves that their occurrence is not associated or limited to our flame modeling approach.

The starting values for the design parameters are chosen as $R_{\text{out}} = -1$ and $\tau_c = 3\text{ms}$, which represents a realistic initial setting. We were able to identify acoustic-acoustic XPs, yet the associated values of the design parameters R^*_{out} and τ^*_c were not physical. We, therefore, select an unstable ITA mode and a stable acoustic mode as initial eigenvalues. Both eigenvalues and their respective mode shapes are depicted in Fig. 4.

For this setting, an XP is found at frequency $f = 132.9\text{Hz}$ and growth rate $\sigma = 19.8\text{rad/s}$. The corresponding parameters are a time lag $\tau_c \approx 5.56\text{ms}$ and reflection coefficient $R_{\text{out}} \approx -1$ (which corresponds to an open end at the combustion chamber exit). The search for the XP concludes after five iterations, and the final distance between the two eigenvalues closest to the XP is of order $\mathcal{O}(10^{-5})$. Moreover, the residuals of Eqs. (23) and (24) are of

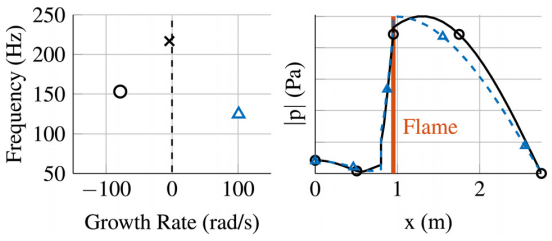

Fig. 4 Left: Eigenvalues found for initial configuration. The two starting values for the XP detection algorithm are marked (ITA mode: triangle, acoustic mode: circle) and one additional mode (cross). Right: The pressure mode shapes corresponding to the ITA mode (dashed line) and acoustic mode (solid line).

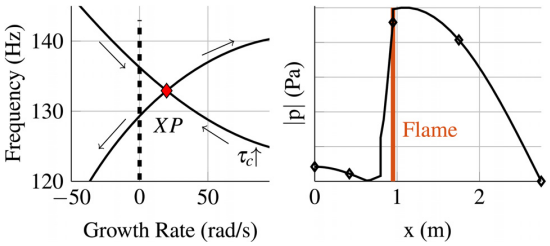

Fig. 5 Left: eigenvalue trajectories for R^*_{out} and varying τ_c in the vicinity of the XP. Right: eigenfunction corresponding to the XP.

order $\mathcal{O}(10^{-10})$ and $\mathcal{O}(10^{-12})$, thus confirming the defective degeneracy of the XP. To graphically illustrate the coalescence of the two eigenvalues and their corresponding eigenfunction, the eigenvalue trajectories and the pressure mode shape at the exceptional point are shown in Fig. 5. For the eigenvalue trajectories, the time lag τ_c is varied around the exceptional point, while R_{out} is kept constant at R^*_{out}. The two branches collide at the exceptional point as expected. As the eigenvalues of the ITA mode and the acoustic mode approach the XP, their eigenfunctions and corresponding mode shapes converge toward each other, forming the mode shape plotted in Fig. 5 right. These results are in line with previous studies on XPs [6,7].

The Impact of Exceptional Points on Uncertainty Quantification

In this section, we study the effect of XPs on the execution and results of uncertainty quantification. Since the parameter sensitivity at the XP is infinite, small variations from the nominal parameters may lead to a large shift in the eigenvalue that is found by the numerical solver. In consequence, we expect large eigenvalue variations from stochastic fluctuations in the input parameters in the vicinity of an XP.

Uncertain Parameters. Following the basic framework set by Guo et al. [16], we specify uncertain distributions for the time lags and standard variations in Eq. (4) to represent uncertainties in the flame dynamics. Acoustic uncertainties are represented by fluctuations in the outlet coefficient R_{out}. Adjusting our model to the one used in Guo et al. [16], we assume zero Mach number for the following analysis, thus acoustic losses are negligible. The resulting XP is found at frequency $f = 128.4\text{Hz}$ and growth rate $\sigma = 73\text{rad/s}$. The nominal values of the design parameters for the identification of the XP τ_c and R_{out} are set to the critical values at the XP. In addition, a reference eigenvalue sufficiently distant to the XP ($f = 122\,\text{Hz}$, $\sigma = 260\,\text{rad/s}$) is investigated corresponding to a reference nominal value $\tau_{c,\text{ref}}$. The nominal values of the remaining FIR parameters are adopted from Guo et al. [16].

Table 1 Uncertainty information of the investigated parameters

Parameters		Nominal	Range
Flame (units: ms)	τ_u	$\tau^0_u = 2.85$	$0.9\tau^0_u$–$1.1\tau^0_u$
	σ_u	$\sigma^0_u = 0.7$	$0.9\sigma^0_u$–$1.1\sigma^0_u$
	τ_{s1}	$\tau^0_{s1} = 1.8$	$0.9\tau^0_{s1}$–$1.1\tau^0_{s1}$
	τ_{s2}	$\tau^0_{s2} = 3.3$	$0.9\tau^0_{s2}$–$1.1\tau^0_{s2}$
	$\tau_{c,XP}$	$\tau^*_c = 5.78$	$\tau^*_c - 0.1\tau^0_{c,\text{ref}}$–$\tau^*_c + 0.1\tau^0_{c,\text{ref}}$
	$\tau_{c,\text{ref}}$	$\tau^0_{c,\text{ref}} = 3$	$0.9\tau^0_{c,\text{ref}}$–$1.1\tau^0_{c,\text{ref}}$
Acoustic boundary condition	R_{out}	$R^*_{\text{out}} = -1$	$0.9R^*_{\text{out}}$–$1.1R^*_{\text{out}}$

The uncertainty distribution of the input parameters is assumed to be independently uniform. This means that all parameter values within the specified interval are equally probable. We fix the interval of τ_c for both eigenvalues. The remaining parameters range from 90% to 110% of their nominal values. An overview of the assumed nominal values and their corresponding ranges is given in Table 1. We stress that the assumed uncertainty distributions may not accurately represent realistic fluctuations in flame dynamics. However, by comparing the results obtained at the XP to those obtained at the reference case, they still provide a valid framework to study the effect of XPs on the confidence of numerical predictions in stability analysis. Furthermore, considering the lack of information regarding the statistical behavior of input variations, a uniform distribution over the assumed interval satisfies the principle of maximum entropy [26] and is, therefore, best suited for the analysis.

Surrogate Modeling and Exceptional Points. Depending on the level of detail desired, the representation of thermoacoustic systems may require a large number of degrees-of-freedom. As a result, computational costs become excessively high, rendering classical Monte Carlo methods for uncertainty quantification economically nonviable (since they require numerous system evaluations to ensure convergence). To keep computational effort at a minimum, a number of tools have been developed that reduce the required calls of the original, high-fidelity system. Many of these methods rely on finding a computationally efficient *surrogate model* that captures the relevant system dynamics within the considered operational range.

We employ the machine learning method called GP to study the potential impact of XPs on the quality of surrogate models. Chattopadhyay et al. [27] showed that GP modeling can be successfully applied to predict combustor instability in thermoacoustic systems. Guo et al. [16] later trained a GP to accurately determine the probability functions and risk factors of thermoacoustic eigenvalues, while greatly reducing the number of evaluations needed compared to Monte Carlo simulation. The paper includes a detailed description of the mathematics on which GP modeling is founded.

Following that work, we apply GP to find surrogate models for eigenvalue predictions both for the reference setting and at the XP. The GP model is trained such that the entire parameter range given in Table 1 is covered. We use a Halton sequence [28] to draw samples from the parameter space (τ_u, σ_u, τ_{s1}, τ_{s2}, τ_c, R_{out}), which guarantees high quality space-filling. At the training sample locations $\boldsymbol{x}^i$, the predictions from the surrogate model $\hat{f}(x^i)$ are equal to the high-fidelity results $f(x^i)$ gained from the original system [16]

$$\hat{f}(\boldsymbol{x}^i) = f(\boldsymbol{x}^i) \tag{25}$$

To quantify the model accuracy, we estimate the generalization error ϵ by means of leave-one-out cross-validation [29]

$$\epsilon = \frac{1}{N}\sum_{i=1}^{N}\left(f_i - \hat{f}_i^{(-i)}\right)^2 \tag{26}$$

where N denotes the total number of training samples, f_i represents the high-fidelity function value at the training sample $\boldsymbol{x}^i$, and $\hat{f}_i^{(-i)}$ is the prediction at the same sample $\boldsymbol{x}^i$ using the GP model, which is built from all training samples except $(\boldsymbol{x}^i, f_i)$ [16]. For increased numbers of total training samples, the accuracy of the GP model should increase, resulting in decreased generalization errors. Above a certain number of samples, the error saturates at a value that can be attributed to the model assumptions, indicating that the quality of the GP model cannot be further improved by increasing the number of samples.

In order to study the quality of the GP models identified at the XP and at the reference eigenvalue, ϵ is evaluated for gradually increasing numbers of samples. Figure 6 compares the obtained profiles of the generalization error ϵ. For predictions of the simple eigenvalue, the generalization error is as low as 0.1% even for a number of only 20 training samples and saturates at 0.01% for sample numbers larger than 40. By contrast, the accuracy of the GP model in the vicinity of the exceptional point does not reach a satisfactory level, even for a number of training samples as high as 200.

To further illustrate the different characteristics of the two GP models, we select 50 additional samples and evaluate the model predictions from both the GP models and the network solver. To maintain comparability both are trained with 60 training samples. These predictions are compared in Fig. 7. The frequency is mapped in the left, the growth rate in the right two plots. For the simple eigenvalue (first row), the predictions match the reference data, i.e., all data points are located in close vicinity to the 45 deg line through the origin. In contrast, at the exceptional point (second row), the GP prediction of frequency (left) and growth rate (right) deviate significantly from their reference values. The failure of the GP model can be explained by the algebraic multiplicity of the XP, which entails two eigenvalues for each parameter setting close to the XP. The eigenvalues returned by the numeric solver can thus not be attributed to one single eigenvalue trajectory, but two. Not being able to distinguish between these two trajectories, the GP model fails to capture the system dynamics of the high-fidelity system.

We thus choose our training samples such that they only include the eigenvalues of one trajectory, and repeat training our GP model with these filtered data. The chosen trajectories are shown in Fig. 8. An updated evaluation of Eq. (26) and a new

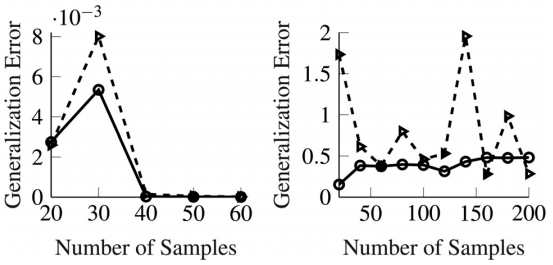

Fig. 6 Generalization error of frequency and growth rate over number of training samples for a simple eigenvalue (left) and at the XP (right)

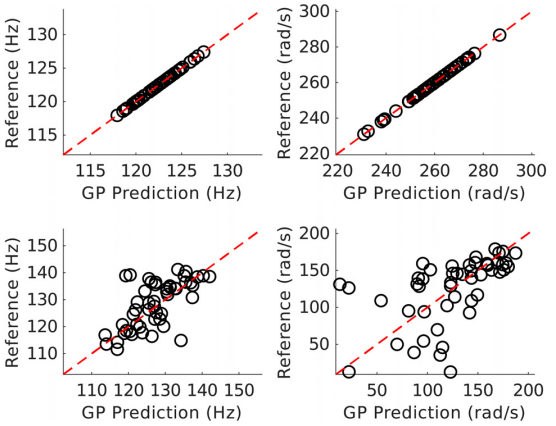

Fig. 7 Comparison of frequency (left) and growth rate (right) obtained by GP model versus reference values at nondefective eigenvalue (first row) and at the XP (second row)

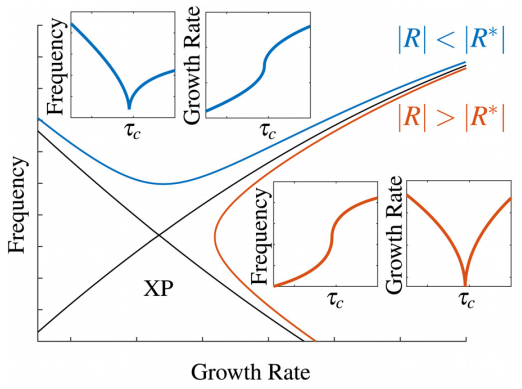

Fig. 8 Illustration of the profiles of frequency and growth rate as a function of τ_c along the marked eigenvalue trajectories

comparison of test data and model predictions in Fig. 9 show that the overall accuracy, in fact, increases significantly. However, the generalization error still reaches values up to 15% for a GP model trained with 200 samples, i.e., the GP model at the XP still performs considerably worse than the one identified at the simple eigenvalue.

To elucidate further effects, we evaluate the generalization error fixing all parameters except one (τ_c). We observe a strong deviation between the generalization errors for frequency and growth rate. The varying accuracy in frequency and growth rate predictions can be attributed to the function profiles $s(\tau_c)$ along the trajectories. For the trajectory $|R| \rightarrow |R^*|^+$ in Fig. 8 the frequency function $f(\tau_c)$, albeit being continuous, is not differentiable at $f(\tau_c^*)$. This function behavior cannot be modeled by the smooth ansatz function on which the GP model is based. Consequently, we observe low-accuracy frequency predictions in the vicinity of the second-order discontinuity, which globally increases the associated generalization error. For the second trajectory ($|R| \rightarrow |R^*|^-$), an equivalent dependency is observed for the growth rate, resulting in a generalization error which is four times as high as the one for frequency predictions. For the original parameter space, the errors due to the second-order discontinuities in either frequency or growth rate accumulate, thus significantly decreasing the model accuracy.

A third source of prediction errors can be attributed to the infinite sensitivity associated with the XP. Due to large eigenvalue drifts at the XP, the training (and testing) data contain few eigenvalues in the immediate vicinity of the XP. In addition, in these regions (marked by green circles in Fig. 9) a small deviation from the optimal model parameters leads to large deviations between the high fidelity output and GP model predictions.

We conclude that a GP model based on a holomorphic ansatz function is not suited to adequately predict eigenvalues in the vicinity of an exceptional point. This needs to be taken into account when performing uncertainty quantification of metastable eigenvalues that might be within close range of an exceptional point, as results obtained from surrogate models may not be reliable. On the other hand, if the generalization error does not diminish for increasing numbers of training samples, it may be due to the presence of an XP. In order to improve the accuracy of the surrogate model, its ansatz function must be able to represent second-order discontinuities, and the sampling method and training data have to be carefully selected, as to include enough information about the output behavior in the vicinity of the XP.

Uncertainty Propagation in the Vicinity of the Exceptional Point. As discussed in the previous section, methods based on holomorphic surrogate functions are not suited to make adequate predictions for frequencies and growth rates of a thermoacoustic system in the vicinity of an XP. In order to study the propagation of input uncertainties close to the XP, we, therefore, revert to Monte Carlo calculations directly based on taX. We use the uncertainty intervals and nominal values presented in Table 1 and randomly draw 20,000 samples to calculate the probability distributions for both frequency and growth rate at the XP and simple eigenvalue. This number was determined in a convergence study, where increasing the samples to 40,000 has shown no significant changes in the obtained PDF. The two eigenvalues we obtain for the nominal values are shown in the first plot of Fig. 10. The corresponding PDFs for frequency and growth rate, respectively, are shown in the right column of the figure.

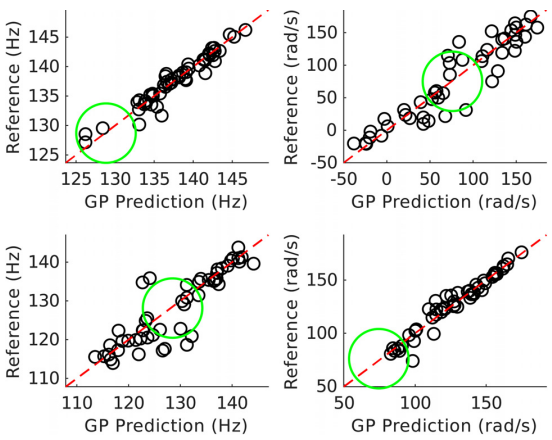

Fig. 9 Comparison of frequency (left) and growth rate (right) obtained by GP model versus reference values for trajectory $|R|>|R^*|$ (first row) and trajectory $|R|<|R^*|$ (second row). Larger circles mark the frequency and growth rate of the XP.

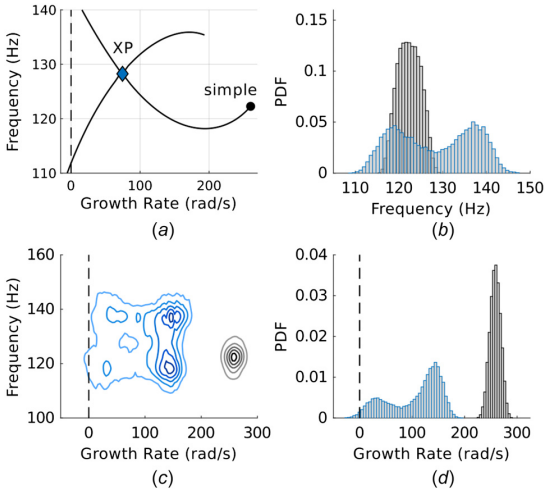

Fig. 10 Left: positions of the XP and of the simple eigenvalue, below the corresponding joint probability distribution of frequency and growth rate. Isolines range from 10% (light) to 90% (dark) of the maximum probability density. Right: probability distributions obtained from Monte Carlo computations at the two eigenvalues.

For the exceptional point, the two eigenvalues that can be found for each parameter setting are reflected in two peaks in the probability functions of frequency and growth rate. As a result, the total variance at the exceptional point is significantly larger than the variance at the simple eigenvalue. This becomes even clearer when looking at the joint distribution of frequency and growth rate (see Fig. 10(*c*)). The total area enclosed by the 10% PDF level contour (i.e., the outermost line) is significantly larger than for the simple eigenvalue.

Owing to the infinite sensitivity at the XP, both PDFs have a minimum at the values of frequency or growth rate corresponding to the XP.

Summary and Conclusion

We introduce a novel method to detect exceptional points in thermoacoustic systems. Our approach differs from previously established methods especially in the way the flame dynamics is modeled. Instead of employing the simplistic "n-τ"-model, we adopt a general expression for the finite impulse response, which we use to model the flame transfer function. By applying our method to a low-order network model of a premixed, swirl-stabilized combustor, we provide evidence of the existence of unstable, yet physically meaningful, exceptional points in the spectrum of a thermoacoustic combustor system.

Subsequently, we study the impact of exceptional points on the process and the results of uncertainty quantification. Since surrogate modeling is an important tool to efficiently analyze and quantify the propagation of input uncertainties, we first study the effect of exceptional points on the process of training a surrogate model. For this purpose, we track the relative error of the system, which we estimate by means of leave-one-out cross-validation, while increasing the total number of training samples. It is shown that the error does not reduce to satisfactory values, even for large numbers of training samples. Because two eigenvalues can be found for each parameter setting in the immediate proximity of the exceptional point, the training data are not restricted to one eigenvalue trajectory, but include data corresponding to two eigenvalue branches that coalesce at the exceptional point. In addition, the surrogate model ansatz function and the infinite sensitivity at the XP result in low model accuracy, even for preselected sets of training data.

Subsequently, we analyze the effect of exceptional points on the propagation of input uncertainties. For this purpose, the probability density functions of frequency and growth rate identified via Monte Carlo computations are compared for two parameter settings: one corresponding to the exceptional point identified in the previous section, and one corresponding to a simple eigenvalue with sufficient distance to the XP. Again the influence of the two eigenvalue branches at the exceptional point is clearly visible. The probability distributions at the XP exhibit two maxima. Since the sensitivity at the exceptional point itself becomes infinite, the probability exhibits a local minimum at the corresponding frequency and growth rate.

We conclude that models of combustion dynamics with realistic flame representations may feature metastable or unstable exceptional points, which are highly relevant to stability analysis. Exceptional points may interfere with classical methods of uncertainty quantification, as results obtained from surrogate models may be unreliable. This is especially critical because the effect of uncertainties is exacerbated in the vicinity of an exceptional point due to increased eigenvalue sensitivity.

Acknowledgment

F. Schaefer gratefully acknowledges the support of Matthias Haeringer, who has helped in many fruitful discussions. S. Guo is grateful for the financial support from doctoral scholarship of Chinese Scholarship Council (No. 201606830045).

Funding Data

- Chinese Scholarship Council (No. 201606830045; Funder ID: 10.13039/501100004543).

Nomenclature

A = system matrix in taX
f = thermoacoustic frequency
FIR = finite impulse response
FTF = flame transfer function
GP = Gaussian process
h_i = FIR model coefficient
ITA = intrinsic thermoacoustic mode
J = objective function
N = number of FIR model coefficients
P = parameter vector
PDF = probability density function
Q = eigenfunction
R_{out} = reflection coefficient at combustor outlet
s = eigenvalue
XP = exceptional point
ϵ = generalization error
σ = modal growth rate
σ_{s1}, σ_{s2} = standard deviations of distributed time lags of flame response for swirl fluctuation
σ_u = standard deviation of the distributed time lags of flame response for axial velocity perturbation
τ_c = mean convective time lag
τ_{s1}, τ_{s2} = means of distributed time lags of flame response for swirl fluctuation
τ_u = mean of distributed time lags of flame response for axial velocity perturbation

References

[1] Poinsot, T., 2017, "Prediction and Control of Combustion Instabilities in Real Engines," Proc. Combust. Inst., **36**(1), pp. 1–28.
[2] Juniper, M. P., and Sujith, R. I., 2018, "Sensitivity and Nonlinearity of Thermoacoustic Oscillations," Annu. Rev. Fluid Mech., **50**(1), pp. 661–689.
[3] Cartarius, H., Main, J., and Wunner, G., 2009, "Exceptional Points in the Spectra of Atoms in External Fields," Phys. Rev. A, **79**(5), p. 053408.
[4] Abdrabou, A., and Lu, Y. Y., 2018, "Exceptional Points of Resonant States on a Periodic Slab," Phys. Rev. A, **97**(6), p. 063822.
[5] Heiss, W. D., 2012, "The Physics of Exceptional Points," J. Phys. A: Math. Theor., **45**(44), p. 444016.
[6] Mensah, G. A., Magri, L., Silva, C. F., Buschmann, P. E., and Moeck, J. P., 2018, "Exceptional Points in the Thermoacoustic Spectrum," J. Sound Vib., **433**, pp. 124–128.
[7] Orchini, A., Silva, C. F., Mensah, G. A., and Moeck, J. P., 2020, "Thermoacoustic Modes of Intrinsic and Acoustic Origin and Their Interplay With Exceptional Points," Combust. Flame, **211**, pp. 83–95.
[8] Bourquard, C., and Noiray, N., 2019, "Stabilization of Acoustic Modes Using Helmholtz and Quarter-Wave Resonators Tuned at Exceptional Points," J. Sound Vib., **445**, pp. 288–307.
[9] Guo, S., Silva, C. F., Ghani, A., and Polifke, W., 2019, "Quantification and Propagation of Uncertainties in Identification of Flame Impulse Response for Thermoacoustic Stability Analysis," ASME J. Eng. Gas Turbines Power, **141**(2), p. 021032.
[10] Magri, L., Bauerheim, M., Nicoud, F., and Juniper, M. P., 2016, "Stability Analysis of Thermo-Acoustic Nonlinear Eigenproblems in Annular Combustors: Part II—Uncertainty Quantification," Comput. Phys., **325**, pp. 411–421.
[11] Mensah, G. A., Magri, L., and Moeck, J. P., 2018, "Methods for the Calculation of Thermoacoustic Stability Boundaries and Monte Carlo-Free Uncertainty Quantification," ASME J. Eng. Gas Turbines Power, **140**(6), p. 61501.
[12] Silva, C., Magri, L., Runte, T., and Polifke, W., 2017, "Uncertainty Quantification of Growth Rates of Thermoacoustic Instability by an Adjoint Helmholtz Solver," ASME J. Eng. Gas Turbines Power, **139**(1), p. 011901.
[13] Ndiaye, A., 2017, "Quantification Des Incertitudes Pour la Prédiction Des Instabilités Thermo-Acoustiques Dans Les Chambres de Combustion," Ph.D. thesis, Universite de Montpellier, Montpellier, France.
[14] Avdonin, A., Jaensch, S., Silva, C. F., Češnovar, M., and Polifke, W., 2018, "Uncertainty Quantification and Sensitivity Analysis of Thermoacoustic Stability With Non-Intrusive Polynomial Chaos Expansion," Combust. Flame, **189**, pp. 300–310.
[15] Avdonin, A., and Polifke, W., 2019, "Quantification of the Impact of Uncertainties in Operating Conditions on the Flame Transfer Function With Non-

Intrusive Polynomial Chaos Expansion," ASME J. Eng. Gas Turbines Power, **141**(1), p. 011020.
[16] Guo, S., Silva, C. F., and Polifke, W., 2019, "Efficient Robust Design for Thermoacoustic Instability Analysis: A Gaussian Process Approach," ASME J. Eng. Gas Turbines Power, **142**(3), p. 031026.
[17] Komarek, T., and Polifke, W., 2010, "Impact of Swirl Fluctuations on the Flame Response of a Perfectly Premixed Swirl Burner," ASME J. Eng. Gas Turbines Power, **132**(6), p. 61503.
[18] Emmert, T., Meindl, M., Jaensch, S., and Polifke, W., 2016, "Linear State Space Interconnect Modeling of Acoustic Systems," Acta Acust. United Acust., **102**(5), pp. 824–833.
[19] Silva, C. F., Merk, M., Komarek, T., and Polifke, W., 2017, "The Contribution of Intrinsic Thermoacoustic Feedback to Combustion Noise and Resonances of a Confined Turbulent Premixed Flame," Combust. Flame, **182**, pp. 269–278.
[20] Polifke, W., 2014, "Black-Box System Identification for Reduced Order Model Construction," Ann. Nucl. Energy, **67**, pp. 109–128.
[21] Oberleithner, K., and Paschereit, C. O., 2016, "Modeling Flame Describing Functions Based on Hydrodynamic Linear Stability Analysis," ASME Paper No. GT2016-57316.
[22] Albayrak, A., and Polifke, W., 2016, "Propagation Velocity of Inertial Waves in Cylindrical Swirling Flow," 23rd International Congress on Sound and Vibration (ICSV23), IIAV, Athens, Greece, July 10–14.
[23] Juniper, M. P., 2018, "Sensitivity Analysis of Thermoacoustic Instability With Adjoint Helmholtz Solvers," Phys. Rev. Fluids, **3**(11), p. 110509.
[24] Güttel, S., and Tisseur, F., 2017, "The Nonlinear Eigenvalue Problem," Acta Numer., **26**, pp. 1–94.
[25] Luchini, P., and Bottaro, A., 2014, "Adjoint Equations in Stability Analysis," Annu. Rev. Fluid Mech., **46**(1), pp. 493–517.
[26] Jaynes, E. T., 1957, "Information Theory and Statistical Mechanics," Phys. Rev., **106**(4)May, pp. 620–630.
[27] Chattopadhyay, P., Mondal, S., Bhattacharya, C., Mukhopadhyay, A., and Ray, A., 2017, "Dynamic Data-Driven Design of Lean Premixed Combustors for Thermoacoustically Stable Operations," ASME J. Mech. Des., **139**(11), p. 111419.
[28] Swiler, L., Slepoy, R., and Giunta, A., 2006, "Evaluation of Sampling Methods in Constructing Response Surface Approximations," AIAA Paper No. 2006-1827.
[29] Marelli, S., and Sudret, B., 2014, "UQLab: A Framework for Uncertainty Quantification in Matlab," ASCE, Liverpool, UK, pp. 2554–2563.

Guillaume J. J. Fournier[1]
TUM School of Engineering and Design,
Department of Engineering Physics and Computation,
Technical University of Munich,
Boltzmannstr. 15,
Garching 85748, Germany
e-mail: fournier@tfd.mw.tum.de

Felicitas Schaefer
TUM School of Engineering and Design,
Department of Engineering Physics and Computation,
Technical University of Munich,
Boltzmannstr. 15,
Garching 85748, Germany
e-mail: schaefer@tfd.mw.tum.de

Matthias Haeringer
TUM School of Engineering and Design,
Department of Engineering Physics and Computation,
Technical University of Munich,
Boltzmannstr. 15,
Garching 85748, Germany
e-mail: haeringer@tfd.mw.tum.de

Camilo F. Silva
TUM School of Engineering and Design,
Department of Engineering Physics and Computation,
Technical University of Munich,
Boltzmannstr. 15,
Garching 85748, Germany
e-mail: silva@tfd.mw.tum.de

Wolfgang Polifke
TUM School of Engineering and Design,
Department of Engineering Physics and Computation,
Technical University of Munich,
Boltzmannstr. 15,
Garching 85748, Germany
e-mail: polifke@tum.de

Interplay of Clusters of Acoustic and Intrinsic Thermoacoustic Modes in Can-Annular Combustors

Thermoacoustic systems can exhibit self-excited instabilities of two nature, namely cavity modes or intrinsic thermoacoustic (ITA) modes. In heavy-duty land-based gas turbines with can-annular combustors, the cross-talk between cans causes the cavity modes of various azimuthal order to create clusters, i.e., ensembles of modes with close frequencies. Similarly, in systems exhibiting rotational symmetry, ITA modes also have the peculiar behavior of forming clusters. In the present study, we investigate how such clusters interplay when they are located in the same frequency range. We first consider a simple Rijke tube configuration and derive a general analytical low-order network model using only dimensionless numbers. We investigate the trajectories of the eigenmodes when changing the downstream length and the flame position. In particular, we show that ITA and acoustic modes can switch nature and their trajectories are strongly influenced by the presence of exceptional points. We then study a generic can-annular combustor. We show that such configuration can be approximated by an equivalent Rijke tube. We demonstrate that, in the absence of mean flow, the eigenvalues of the system necessarily lie on specific trajectories imposed by the upstream conditions. [DOI: 10.1115/1.4055381]

1 Introduction and Motivation

Lean premixed combustion systems have been developed in order to reduce emissions and address environmental issues. Unfortunately, such technology is also more prone to combustion instabilities [1,2]. The coupling between the unsteady heat release of the flame and the acoustics of the system may result in a positive feedback loop leading to self-excited instabilities with growing pressure fluctuations. It is crucial to understand and mitigate such phenomenon as repeated exposure to high level of pressure can lead to catastrophic engine failure [3].

Since the Apollo program and the development of modern rocket engines, thermoacoustic instabilities have been interpreted as acoustic eigenmodes of the system driven by unsteady heat release [4,5]. However, Hoeijmakers et al. [6,7], experimentally and with a simple analytical model, showed evidence of thermoacoustic instabilities in an anechoic environment. This situation was paradoxical and constituted a significant deviation from the established interpretation. These observations were later confirmed with high-fidelity numerical simulations [8,9]. Bomberg et al. [10] formally identified the so-called intrinsic thermoacoustic (ITA) feedback loop, a flame-flow-acoustic interaction intrinsic to the flame and its immediate surrounding and not involving the acoustics of the system, which allowed Emmert et al. [11] to justify the physical nature of the previous observations. Emmert et al. [12] then demonstrated that the ITA feedback loop gives rise to a new set of thermoacoustic modes of different nature also for reflecting boundaries and identified such an ITA mode as the most unstable mode in a longitudinal test-rig. Yong et al. [13] showed that for a marginally stable ITA mode, the velocity fluctuations and the gradient of pressure fluctuations change sign across the flame, thus providing a simple identification criterion.

This new paradigm fundamentally changed the understanding of thermoacoustic instabilities and shed a new light on inexplicable phenomena reported in earlier studies, such as "the new set of modes" described by Dowling and Stow [14], the "bulk mode" highlighted by Eckstein and Sattelmayer [15,16], or the "convective scaling" of thermoacoustic eigenfrequencies [17].

[1]Corresponding author.

Manuscript received July 11, 2022; final manuscript received July 27, 2022; published online October 14, 2022. Editor: Jerzy T. Sawicki.

Numerous studies then investigated the role of both types of thermoacoustic instabilities. Hosseini et al. investigated the interplay between modes of ITA and acoustic origin and showed that, when they are far away from one another, they do not influence each other [18]. Mensah et al. [19] highlighted the presence of exceptional points in the spectrum due to the coalescence of modes of ITA and acoustic origin. Silva et al. [20] and Orchini et al. [21] further investigated the role of exceptional points in the interplay between ITA and acoustic modes and highlighted characteristic trajectories. Buschmann et al. [22,23] observed the existence of ITA modes in an annular combustor and showed that they appear in clusters, i.e., a collection of eigenmodes with close oscillation frequencies but different growth rates. Fournier et al. [24] used a low-order model to explain why the ITA clusters align around a "pure ITA frequency," i.e., the frequency of an ITA mode in an anechoic environment.

Annular and can-annular combustors exhibit discrete rotational symmetry and the azimuthal dimension leads to interesting new properties. Numerical simulations [25,26] and experiments [27] revealed that the full can-annular configuration gives rise to new eigenmodes, with mode shapes involving multiple cans, that do not exist in a single can approximation. Farisco et al. [28] numerically investigated the effect of the gap, demonstrated that the cross-talk between cans cannot be ignored and estimated a transmission coefficient. Ghirardo et al. [29] gave further proof using two-dimensional Helmholtz simulations and experimental results. They highlighted that modes of various azimuthal orders emerge due to the weak coupling between cans and form clusters of acoustic modes. Jegal et al. [30] and Moon et al. [31,32] used a test-rig with two and four cans, respectively, to explore the effect of can coupling on the stability of the burners. Because the eigenmodes are closely spaced in clusters, mixed states, with several distinct types of interaction patterns, were observed.

Recent studies tackled the problem at a more fundamental level using low-order network models. Fournier et al. [24] proposed the modeling of the gap as a thin annulus and the method was applied by Haeringer et al. [33] in a strategy to tune single-can test-rigs to mimic full engines. Von Saldern et al. [34] proposed to model the cross-talk between cans with the Rayleigh conductivity, which relates the acoustic flux through the aperture to the pressure gradient between cans. Both modeling approaches were compared by Fournier et al. [35] and an extension was given, using a flow parameter in terms of a characteristic length, giving quantitatively accurate results. Von Saldern et al. [36] derived an effective impedance model for non-compact connections and analyzed the role of liners in damping azimuthal thermoacoustic modes. Orchini [37] and Pedergnana and Noiray [38] explored the effect of mean flow and derived effective impedance models that show explicit dependence on the grazing flow Mach number. Orchini et al. [39] then showed that such an effect gives rise to new sets of clusters of modes of aeroacoustic origin due to the coupling with the response of the shear layer in the apertures.

Both phenomena of ITA clusters in annular configuration and acoustic clusters in can-annular configurations are fairly well understood taken individually. In the present study, we want to investigate the interplay between clusters of acoustic and ITA modes in a can-annular combustor when they are located in the same frequency range. The motivation of our study is illustrated by Fig. 1, which shows the spectrum of two generic can-annular combustors obtained with FEM Helmholtz computations using COMSOL MULTIPHYSICS. The geometrical and thermodynamic parameters are given in Table 1 and both configurations are investigated more in-depth in Sec. 4. For Configuration A, the ITA and acoustic clusters are distinct and identifiable. In Configuration B, the flame position differs by only 15% but the total length of the combustor is kept constant. In this scenario, the clusters cannot be distinguished from one another and seem to be entangled. The paper aims at explaining such drastic change in the spectrum and giving more insight on the ITA and acoustic trajectories in can-annular combustors.

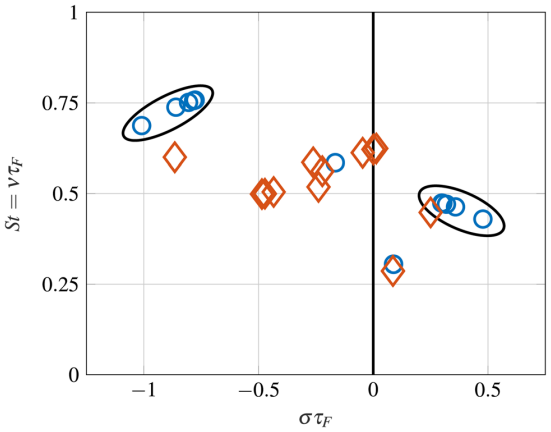

Fig. 1 Spectrum of two generic can-annular combustors obtained with FEM computations. Parameters are given in Table 1. For Configuration A (blue circles), the ITA and acoustic clusters are distinct and identifiable. Two modes are offset from their respective clusters, which is explained later in the paper. In Configuration B (orange diamonds), the flame position inside the combustor is changed but the total length is kept constant. The clusters become entangled and cannot be distinguished from one another.

Table 1 Geometrical and thermodynamic parameters of a generic can-annular combustor such as presented in Ref. [33]. The FTF parameters are adapted from Ref. [40].

	Configuration A	Configuration B
N	10	10
H (m)	0.15	0.15
L_g^*	0.25	0.25
n	1.2	1.2
τ_F (s)	3.5×10^{-3}	3.5×10^{-3}
L_u (m)	0.5	0.8
L_d (m)	1.5	1.2

Fournier et al. [24] and Haeringer et al. [33] showed that, under some assumptions discussed later in the paper, a can-annular combustor can be fairly well represented by an equivalent Rijke tube. The latter is one of the simplest thermoacoustic system and has been extensively studied for decades. This allows us to gain insight at a more fundamental level. Therefore, the paper structures as follows: in Sec. 2, we first consider a simple Rijke tube and analytically derive the dispersion relation. The problem remains generally applicable to configurations of arbitrary geometrical and thermodynamic parameters thanks to the use of Buckingham Π theorem and dimensionless numbers. In Sec. 3, we then investigate the influence of the length of the Rijke tube and the flame position inside it on both ITA and acoustic modes. In Sec. 4, the results are transposed to two generic can-annular combustors and allow us to explain the spectrum observed in Fig. 1. Finally, the modeling assumptions and the limits of validity are discussed.

2 Network Model of a Generic Rijke Tube Configuration

2.1 Case and Flow Description. The system considered is a generic Rijke tube, as depicted in Fig. 2. Ducts of length L_u and L_d are placed upstream and downstream of the flame, respectively. The acoustic boundaries are defined by the reflection coefficients R_i and R_o at the inlet and outlet, respectively. We assume zero

mean flow when modeling the thermoacoustic behavior of the system, in particular wave propagation in the ducts. The model is based on a network approach. Recall the definition of the characteristic wave amplitudes

$$f \equiv \frac{1}{2}\left(\frac{p'}{\bar{\rho}c} + u'\right), \quad g \equiv \frac{1}{2}\left(\frac{p'}{\bar{\rho}c} - u'\right) \tag{1}$$

In the ducts, we assume that only one-dimensional (1D) planar acoustic waves propagate. The f and g waves in the system relate as follows:

$$\begin{bmatrix} f_u \\ g_u \end{bmatrix} = \begin{bmatrix} e^{-s\tau_u} & 0 \\ 0 & e^{s\tau_u} \end{bmatrix} \begin{bmatrix} f_i \\ g_i \end{bmatrix}, \quad \begin{bmatrix} f_o \\ g_o \end{bmatrix} = \begin{bmatrix} e^{-s\tau_d} & 0 \\ 0 & e^{s\tau_d} \end{bmatrix} \begin{bmatrix} f_d \\ g_d \end{bmatrix} \tag{2}$$

The term $e^{\pm s\tau}$ represents the phase change resulting from the acoustic propagation of the wave and τ is the time it takes to travel. $\tau_u = L_u/c_u$ and $\tau_d = L_d/c_d$ are the propagation times upstream and downstream the flame respectively, c_u and c_d are the speed of sound in the respective regions, and $s = \sigma + i\omega$ is the Laplace variable, with σ the growth rate and ω the angular frequency.

The acoustic boundary conditions of the system are defined using reflection coefficients. The latter write as follows:

$$R_i = \frac{f_i}{g_i}, \quad R_o = \frac{g_o}{f_o} \tag{3}$$

2.2 Flame and Unsteady Heat Release Model. The acoustic flame model is derived using the linearized Rankine Hugoniot jump equations for a compact heat source at rest with unsteady heat release fluctuations [11,41]

$$\begin{cases} \dfrac{p'_d}{\bar{\rho}_d c_d} = \xi \dfrac{p'_u}{\bar{\rho}_u c_u} \\ u'_d = u'_u + \theta \dot{q}' \end{cases} \tag{4}$$

where $\xi = \bar{\rho}_u c_u / \bar{\rho}_d c_d$ is the ratio of specific impedances, $\theta = (T_d - T_u)/T_u$ the normalized temperature ratio and $\dot{q}' = \dot{Q}'\bar{u}_u/\dot{Q}$ the normalized global heat release fluctuations of the flame.

A flame transfer function (FTF) is used to relate the unsteady heat release fluctuations $\dot{q}'$ to the acoustic velocity fluctuations upstream the flame u'_u. For this study, the famous $n-\tau$ model from Crocco is used [42]

$$\frac{\dot{q}'}{u'_u} = \mathcal{F}(s) = n e^{-s\tau_F} \tag{5}$$

with n and τ_F the gain and time delay of the flame respectively. Such a simple model captures the essential aspects of a generic flame and is convenient to use in the context of low-order models as it allows to derive analytical solutions.

Writing Eq. (4) with the characteristic wave amplitudes f and g and inserting Eq. (5) leads to the flame transfer matrix:

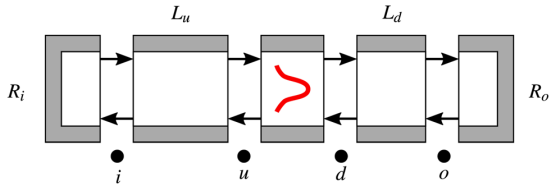

Fig. 2 Schematic of a generic Rijke tube of length L_u upstream the flame, L_d downstream the flame. The acoustic boundaries are defined by the reflection coefficients R_i and R_o at the inlet and outlet respectively.

$$\begin{bmatrix} f_d \\ g_d \end{bmatrix} = \begin{bmatrix} \mathcal{T}_a(s) & \mathcal{T}_b(s) \\ \mathcal{T}_b(s) & \mathcal{T}_a(s) \end{bmatrix} \begin{bmatrix} f_u \\ g_u \end{bmatrix} \tag{6}$$

The matrix is symmetric, with $\mathcal{T}_a(s) = \frac{1}{2}(\xi + 1 + n\theta e^{-s\tau_F})$ and $\mathcal{T}_b(s) = \frac{1}{2}(\xi - 1 - n\theta e^{-s\tau_F})$.

2.3 Dimensionless Nonlinear Eigenvalue Problem. Combining Eqs. (2), (3), and (6), the governing equations of the system can be cast in the matrix form:

$$\begin{bmatrix} 1 & -R_i & 0 & 0 \\ 0 & 0 & -R_o & 1 \\ \mathcal{T}_a(s)e^{-s(\tau_u+\tau_d)} & \mathcal{T}_b(s)e^{s(\tau_u-\tau_d)} & -1 & 0 \\ \mathcal{T}_b(s)e^{-s(\tau_u-\tau_d)} & \mathcal{T}_a(s)e^{s(\tau_u+\tau_d)} & 0 & -1 \end{bmatrix} \begin{bmatrix} f_i \\ g_i \\ f_o \\ g_o \end{bmatrix} = \begin{bmatrix} 0 \\ 0 \\ 0 \\ 0 \end{bmatrix} \tag{7}$$

The four governing equations describing the system involve the following parameters: the Laplace variable s, the propagation times τ_u and τ_d, the ratio of specific impedances ξ, the temperature ratio θ, the reflection coefficients R_i and R_o, the time delay of the flame τ_F and its gain n. Among these nine parameters, five are already dimensionless: n, ξ, θ, R_i and R_o. The remaining four parameters admit a basis of one fundamental dimension, time. Applying Buckingham Π theorem [43,44], we define the following dimensionless numbers:

$$s^* = s\tau_F, \quad \tau_u^* = \frac{\tau_u}{\tau_F}, \quad \tau_d^* = \frac{\tau_d}{\tau_F} \tag{8}$$

The system is therefore fully described using eight independent dimensionless numbers. The nondimensionalization of the problem allows us to generalize the results to configurations of arbitrary geometrical and thermodynamic parameters, and therefore allows us to draw general conclusions. This approach has successfully been applied in thermoacoustics [29,35,44].

Mathematically, Eq. (7) has nontrivial solutions if the determinant of the matrix is null. Solving for the determinant and using the dimensionless numbers defined in Eq. (8) leads to the dispersion relation:

$$\begin{aligned} \mathcal{D}(s^*) = &\left(\xi + 1 + n\theta e^{-s^*}\right)\left(1 - R_i R_o e^{-2s^*\left(\tau_u^* + \tau_d^*\right)}\right) \\ &+ \left(\xi - 1 - n\theta e^{-s^*}\right)\left(R_i e^{-2s^*\tau_u^*} - R_o e^{-2s^*\tau_d^*}\right) = 0 \end{aligned} \tag{9}$$

Equation (9) is nonlinear in s^* and can generally not be solved analytically. Instead, we solve it numerically using taX,[2] the open-source MATLAB package developed by the TFD group to build and solve low-order thermoacoustic network models [45]. taX transforms Eq. (9) into a linear eigenvalue problem, thus facilitating the use of direct solvers to easily find all eigenmodes, in particular ITA modes, which remain difficult to find with iterative methods due to their small basin of attraction [22,46].

2.4 Interesting Special Cases. Although Eq. (9) is nonlinear in s^*, in some cases, it can be solved analytically. We discuss here three interesting limit cases. In the following, we assume the reflection coefficients R_i and R_o to be real-valued and independent of frequency.

- For the case of a very weak flame (i.e., $n \approx 0$), the dispersion relation reduces to $1 - R_i R_o e^{-2s^*\left(\tau_u^* + \tau_d^*\right)} = 0$ and we recover the classical solution for an acoustic mode in a duct [7,47]:

[2] https://gitlab.lrz.de/tfd/tax

$$\begin{cases} \mathrm{St} = \nu\tau_F = \dfrac{j}{4(\tau_u^* + \tau_d^*)} \\ \sigma\tau_F = \dfrac{1}{2(\tau_u^* + \tau_d^*)} \ln\left(R_i R_o (-1)^j\right) \end{cases}, \quad j \in \mathbb{N} \tag{10}$$

where the Strouhal number St is the dimensionless frequency.

- In the case of anechoic boundaries $R_i = R_o = 0$, Eq. (9) becomes $\xi + 1 + n\theta e^{-s^*} = 0$. The acoustic modes disappear and only the pure ITA modes remain, i.e., ITA modes in an anechoic environment. This was extensively discussed in previous studies [7,11] and the eigenfrequencies are given by:

$$\begin{cases} \mathrm{St} = \nu\tau_F = \dfrac{(2j+1)}{2} \\ \sigma\tau_F = \ln\left(\dfrac{n\theta}{1+\xi}\right) \end{cases}, \quad j \in \mathbb{N} \tag{11}$$

- A third remarkable case arises when the boundaries are identical $R_i = R_o$, and when the flame is placed in the Rijke tube specifically such as the propagation times in the upstream and downstream ducts are identical $\tau_u^* = \tau_d^*$. In this configuration, the dispersion relation becomes:

$$\left(\xi + 1 + n\theta e^{-s^*}\right)\left(1 - R_i R_o e^{-2s^*\left(\tau_u^* + \tau_d^*\right)}\right) = 0 \tag{12}$$

The dispersion relation is factored in two terms. The first term corresponds to the dispersion relation in an anechoic environment, leading to pure ITA modes, and the second term is the dispersion relation for a pure acoustic system. Although a flame is present and the acoustic boundaries are not anechoic, the eigenvalues of the thermoacoustic system correspond exactly to the pure ITA and acoustic modes defined by Eqs. (10) and (11). Such a result can be explained using phasor analysis, which has already been used in thermoacoustics [13,16,17,24,48–50]. For example, if we consider the case of fully reflecting boundaries $R_i = R_o = \pm 1$, the acoustic mode is marginally stable, thus simplifying the phasor analysis with arrows of fixed length. At the inlet and the outlet, to satisfy the boundary conditions, the phasor f and g have opposite directions (case Open–Open) or the same direction (case Closed –Closed) respectively. Traveling from the boundaries to the flame, from both upstream and downstream sides, the phasors rotate by an identical angle $\omega\tau_u = \omega\tau_d = \pi/2$. The flame is located at a velocity node or a pressure node, respectively. The eigenmodes are simply the half-wave modes for a simple acoustic system with a temperature jump.

3 Interplay of Intrinsic Thermoacoustic and Acoustic Eigenmodes

In this section, we investigate the impact on the eigenmodes of the length of the Rijke tube and the position of the flame inside it. We consider here only the case Open–Open $R_i = R_o = -1$. The FTF parameters n and τ_F are kept constant, as well as the flame thermodynamic parameters θ, ξ.

3.1 Short Upstream Length. In this case, we consider a short upstream length, the dimensionless upstream propagation time is small $\tau_u^* = 0.1$. We change the downstream length, i.e., we vary the downstream dimensionless propagation time τ_d^* from 0 to 2, all other parameters being held constant. We consider only the fundamental acoustic and ITA thermoacoustic modes and disregard all the higher-order modes.

Figure 3 depicts the trajectories in the complex plane of both eigenmodes. When increasing the downstream length, the frequency of the acoustic mode decreases, as expected. For the ITA mode, when τ_d^* is small, the acoustic mode is far away and the two modes do not interplay. Therefore, its growth rate changes but the frequency remains constant and equal to the pure ITA frequency $\mathrm{St} = \nu\tau_F = 1/2$ [20,21,51]. When increasing τ_d^*, the ITA mode eventually converges to a special point, indicated by the cross in Fig. 3. The point can clearly be identified: the system behaves exactly as if, just after the flame, the duct L_d and the outlet boundary are replaced by a non-reflecting boundary, i.e., $R = 0$, while the upstream condition remains unchanged ($R_i = -1$). The flame is placed in an effective semi-anechoic environment. This can be explained by the fact that $R_d = g_d/f_d = R_o e^{-2s^*\tau_d^*}$, and for positive growth rate, when τ_d^* increases, $\lim_{\tau_d \to \infty} |R_d| = |R_o| e^{-\sigma\tau_d} \approx 0$. In other words, the longer the downstream duct, the weaker the effective reflection coefficient for an unstable mode. The system downstream of the flame is equivalent to a non-reflecting boundary.

The red circles mark the setup where $\tau_d^* = \tau_u^*$. For this specific scenario, the two modes are decoupled as shown by Eq. (12). Here, the acoustic mode is outside of the frequency range of interest and therefore not shown in Fig. 3. However, the ITA mode is indeed present and verifies the analytical expression Eq. (11).

Figure 4 shows similar results for a different upstream configuration. In this case, the upstream length is such that $\tau_u^* = 0.2$, and all other parameters are kept constant and identical to the previous case. We vary the downstream length, i.e., τ_d^* increases from 0 to 2. Similarly to the previous case, when τ_d^* remains small, the ITA and acoustic modes are far away from each other and do not interplay: the ITA mode has a constant pure ITA frequency $\mathrm{St} = 1/2$, and its growth rate changes. However, for larger downstream lengths, the ITA mode does not converge to the semi-anechoic mode, but passes around it and keeps decreasing in frequency: it turns into the acoustic mode. Conversely, the mode initially classified as acoustic, when τ_d^* is small, first decreases in frequency but then converges to the semi-anechoic eigenmode. It is highlighted that the two modes can switch nature, as previously reported [18,34,47]. However, we will not discuss how the eigenmodes can be classified as ITA and acoustic and when precisely the modes switch nature as this question is out of the scope of this study and already discussed by Yong et al. [50].

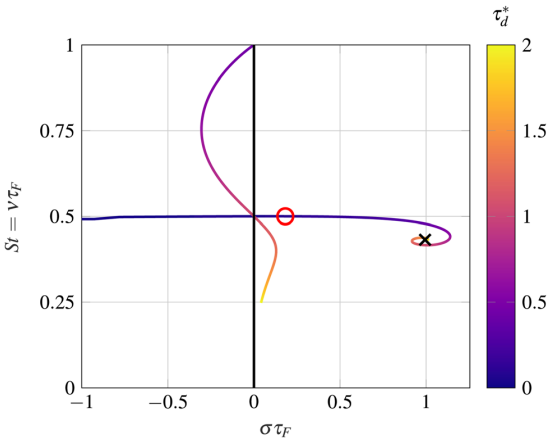

Fig. 3 Trajectories of the eigenmodes in the complex plane for a short upstream, $\tau_u^* = 0.1$ fixed. When increasing τ_d^*, i.e., increasing the downstream length, as expected, the frequency of the acoustic mode decreases. On the other hand, the ITA is around its pure ITA frequency $\mathrm{St} = 1/2$ but its growth rate changes. Eventually, the ITA mode converges to the semi-anechoic configuration identified by the cross. The circle indicates when $\tau_d^* = \tau_u^*$, i.e., when the modes are fully decoupled according to Eq. (12). However, note that the acoustic mode is outside of the frequency range of interest and therefore not visible.

3.2 Long Upstream Length: The Impact of an Exceptional Point on the Acoustic and Intrinsic Thermoacoustic Trajectories. We now investigate the trajectories when the dimensionless upstream propagation time is large $\tau_u^* = 0.45$. All other parameters are kept constant and equal to the case described in Sec. 3.1. The downstream length is again varied such that τ_d^* increases from 0 to 2. Figure 5 shows the trajectories of the eigenmodes in the complex plane. When increasing τ_d^*, the two eigenmodes first converge toward each other before changing directions, which suggests the presence of an exceptional point (XP) in the vicinity of the parameter space. The circles indicate when the propagation times are identical $\tau_d^* = \tau_u^*$: the eigenmodes satisfy the pure ITA and acoustic modes defined by Eqs. (10) and (11).

Exceptional points are found in various disciplines, including thermoacoustics [19,20]. At an exceptional point, at least two eigenvalues and their respective eigenfunctions coalesce, and the eigenvalue sensitivity with respect to changes in parameters becomes infinite. Recall that the eigenvalues are the solution of the dispersion relation:

$$\mathcal{D}(s^*; \tau_d^*, n) = 0 \tag{13}$$

Eigenvalues can be classified according to their algebraic and geometric multiplicity, *am* and *gm* respectively. The algebraic multiplicity quantifies the multiplicity of the eigenvalue as a root of the dispersion relation Eq. (13). The geometric multiplicity is the dimension of the associated eigenspace, i.e., the number of linearly independent eigenvectors. Eigenvalues can be simple ($am = gm = 1$), semi-simple ($am = gm > 1$) or defective ($am > gm$). Defective eigenvalues that are branch-point singularities are called exceptional points (XPs). In the context of thermoacoustics, XPs are primarily attributed to the interplay between intrinsic thermoacoustic modes (ITA) and acoustic modes, i.e., thermoacoustic modes of different natures [19]. Previous studies have investigated XPs associated with the parameters (n, τ_F) [19,44], or (τ_c, R_o), where τ_c is the time-delay of a realistic flame impulse response [52]. Indeed, for the modes to coalesce, they need to have the same frequency, mainly driven by τ_F or τ_c for an ITA mode, and the same growth rate, mainly driven by the gain (strength of the flame n) or losses ($R_o \neq \pm 1$).

In the present study, the approach is different because the time-delay of the flame τ_F is fixed, which in turn settles the value of the pure ITA frequency (solution of Eq. (11)). By changing τ_d^*, we allow the acoustic mode to move in the complex plane and be in the same frequency range as the ITA mode. For the modes to coalesce, their growth rates must also be equal, which is obtained by changing the strength of the flame n. According to Mensah et al. [19], for an ITA and acoustic mode to coalesce, the following relations need to be satisfied:

$$\begin{cases} \dfrac{\partial \mathcal{D}(s^*; \tau_d^*, n)}{\partial s^*} = 0 & (14) \\ \dfrac{\partial^2 \mathcal{D}(s^*; \tau_d^*, n)}{\partial s^{*2}} \neq 0 & (15) \end{cases}$$

The solution of the complex-valued Eqs. (13) and (14) is the set of parameters $(\tau_{d,XP}^*, n_{XP})$ and the defective eigenvalue s_{XP}^*. We highlight here one special configuration where an easy analytical solution is found. For the special case where $\tau_d^* = \tau_u^* = 1/2$, following Eqs. (10) and (11), the ITA and the acoustic mode share the same frequency $\mathrm{St} = 1/2$. For the modes to coalesce, they need also to have the same growth rate. The acoustic mode is marginally stable. For the ITA mode to also be marginally stable, the gain of the flame response must be $n_{XP} = (1 + \xi)/\theta$. It is straight forward to demonstrate that the eigenvalue $s_{XP}^* = i\pi$ and the set of parameters $(\tau_{d,XP}^* = 1/2, n_{XP})$ satisfy Eqs. (13) and (14).

However, in general, the *XP* cannot be found analytically, and even finding it numerically remains challenging. For the configuration $\tau_u^* = 0.45$ depicted in Fig. 5, the method introduced by Schaefer et al. [52] is applied to identify the exceptional point. Results are shown in Fig. 6. Colors indicate isolines of flame strength n, along which the downstream propagation time τ_d^* varies. We observe strong mode veering, a manifestation of avoided crossing of two eigenvalues [20,21,44,53]. The presence of the XP induces the eigenvalues to strongly veer, resulting in the characteristic trajectories observed in Fig. 5. This also explains why modes can switch nature, i.e., the mode of acoustic nature when τ_d^* is small becomes ITA for large values of τ_d^*, and vice versa.

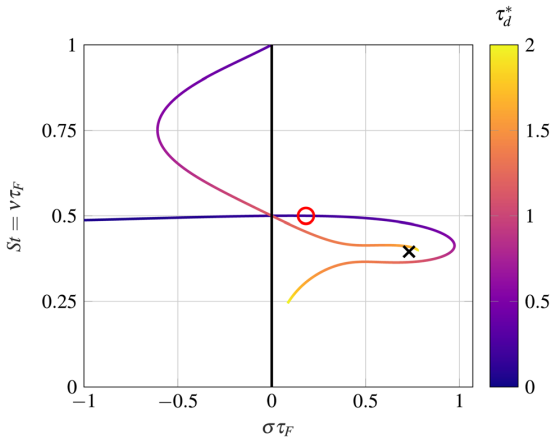

Fig. 4 Trajectories of the eigenmodes in the complex plane for a longer upstream length $\tau_u^* = 0.2$ fixed. For small values of τ_d^*, the ITA mode has once more its frequency near the pure ITA frequency St = 1/2, and its growth rate increases with τ_d^*. However, the ITA mode does not converge to the semi-anechoic point, identified by the cross, but passes around it while its frequency keeps decreasing. Conversely, the acoustic mode first decreases in frequency but then converges to the semi-anechoic eigenmode. The two eigenmodes switch nature. The circle indicates when $\tau_d^* = \tau_u^*$ and the ITA mode is a solution of Eq. (11).

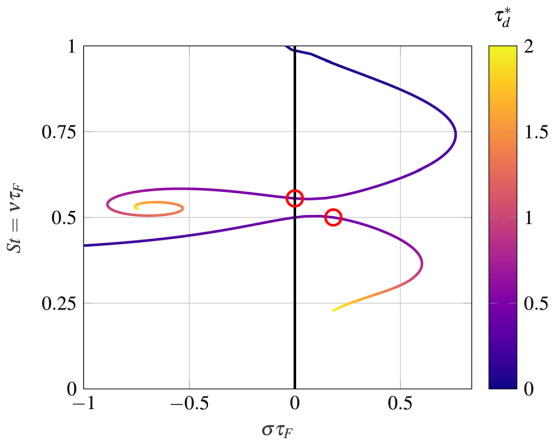

Fig. 5 Trajectories of the eigenmodes for the upstream configuration $\tau_u^* = 0.45$. When increasing τ_d^*, the modes first converge toward each other before changing direction, suggesting the presence of an exceptional point. The circles indicate when $\tau_d^* = \tau_u^*$, the acoustic and ITA modes are effectively decoupled and are solutions of Eqs. (10) and (11). Similarly to the results shown in Fig. 4, the eigenmodes also switch nature.

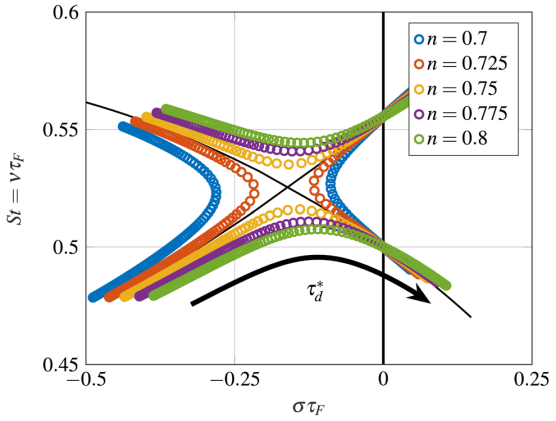

Fig. 6 Identification of an exceptional point for the upstream case $\tau_u^* = 0.45$. Colors indicate isolines of flame strength n. When varying the dimensionless downstream propagation time τ_d^* from 0.42 to 0.48, the *XP* causes the eigenmodes to strongly veer, leading to the characteristic trajectories observed in Fig. 5.

4 Application to Can-Annular Combustors

In this section, we want to extend the model to can-annular configurations. We first describe a typical can-annular combustor. We then show how such a system can be reduced to a simple Rijke tube, thus allowing us to transpose the methods and results of Secs. 2 and 3. Finally, we discuss the assumptions and limitations of our modeling approach.

4.1 Case Description and Low-Order Modeling. The generic combustor consists of N identical cans placed in an annular arrangement. Upstream the cans, we neglect the impact of the plenum, as it often shows little influence [33]. The cans are acoustically decoupled and the inlet reflection coefficient is set to $R_i = -1$. At the outlet of the cans, a turbine is placed to extract energy from the fluid. The acoustic response of the turbine stage is modeled by a reflection coefficient with a fixed gain and a zero phase response [54], we choose $R_o = 1$ as losses have little quantitative impact [55]. The Mach number is low, typically below 0.2 [27,29]. Consequently, we assume zero mean flow when modeling the thermoacoustic behavior of the cans. Finally, entropy waves are assumed to have a negligible effect and are not taken into account [29,56].

Figure 7 depicts a unit-cell of the investigated can-annular combustor. Following previous studies [29,35], we consider cans of width H and a gap of size L_g, leading to the coupling strength between cans $L_g^* = L_g/H$. The flame is placed inside the can at a distance L_u and L_d from the inlet and outlet, respectively. Two cases are investigated: Configuration A has a shorter upstream

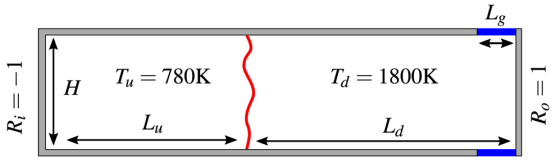

Fig. 7 Unit-cell of a generic can-annular combustor. The flame is placed at a distance L_u and L_d from the inlet and the outlet, respectively. The can is decoupled from the plenum at the inlet and closed at the outlet. However, acoustic communication with the neighboring cans is possible through the gap L_g. Parameters are given in Table 1.

duct than Configuration B, however, the total length of the combustor $L_u + L_d$ is kept constant. The modeling of the flame is identical to Sec. 2.2. For the sake of simplicity, we consider a simple $n - \tau$ model adapted from Ref. [40], but results could be easily extended to realistic flames, since distributed time delay models are nothing more but a collection of individual $n - \tau$ models [48]. The geometrical and thermodynamic parameters, inspired from a realistic combustor such as presented in Ref. [33], are given in Table 1.

4.2 Bloch Theory. As the cans are geometrically identical, the system exhibits discrete rotational symmetry. Applying Bloch theory [57], which is now well established in thermoacoustics [24,29,33–35,58,59], the acoustic pressure in the frequency domain can be written as

$$\hat{p}(\boldsymbol{x}) = \psi(\boldsymbol{x}) e^{im\varphi},\ m = \begin{cases} -\dfrac{N}{2}+1, \ldots, \dfrac{N}{2} & N \text{ even} \\ -\dfrac{N-1}{2}, \ldots, \dfrac{N-1}{2} & N \text{ odd} \end{cases} \tag{16}$$

where φ is the azimuthal coordinate around the axis of rotational symmetry, m is the Bloch wave number, identical to the azimuthal order [29] and $\psi(\boldsymbol{x})$ a function identical in all unit-cells and $2\pi/N$ periodic in φ.

The eigenmodes are classified into three groups: axial or push-push ($m = 0$), push-pull ($m = N/2$), and azimuthal modes (all other values of m). We additionally assume reflection symmetry along the planes $\varphi = \text{const.}$ that pass through the center of the cell (no mean flow in the azimuthal direction): the azimuthal modes come in degenerate pairs which differ only by their spinning direction. From the study of a single unit-cell, the behavior of the full system is preserved by considering all azimuthal mode orders m. We reduce the can-annular system to a single unit-cell and apply Bloch boundaries in the gap region.

4.3 Equivalent Rijke Tube Model. Previous studies [24,33–35] showed the possibility of transforming a can-annular configuration into an equivalent longitudinal combustor, where all the two-dimensional effects of can-to-can communication in the cross-talk area are lumped into an equivalent outlet reflection coefficient $\mathcal{R}_m$. Using the characteristic length model introduced by Fournier et al. [35], the equivalent reflection coefficient writes

$$\mathcal{R}_m = 1 - \frac{2\sin^2\left(\dfrac{\pi m}{N}\right)}{iSt\dfrac{\pi L_{char,m}^* \tau_c^*}{L_g^*} + \sin^2\left(\dfrac{\pi m}{N}\right)} \tag{17}$$

with $L_g^* = L_g/H$ the coupling strength between the cans due to the size of the gap, $L_{\text{char},m}^* = L_{\text{char},m}/H$ the dimensionless characteristic length that models the inertia of the volume of fluid, and $\tau_c^* = H/(c_d\tau_F)$ the dimensionless propagation time in the azimuthal direction. The axial mode is a special case because the equivalent reflection coefficient is simply $\mathcal{R}_{m=0} = 1$: the push-push mode is not affected by the acoustic communication with neighboring cans, i.e., the eigenmode is exactly the same as in the single can system. For all the other azimuthal mode orders, the gain of the equivalent reflection coefficient $\mathcal{R}_m$ is unity, however, its phase response is not trivial, as shown in Fig. 8. Starting from π, the phase monotonically decreases and converges toward zero as the frequency increases. The characteristic length model shows perfect agreement with the FEM Helmholtz reference obtained with COMSOL MULTIPHYSICS. For low frequencies $\text{St} < 1$, the phase response of the gap can be approximated by the tangent at the origin, indicated by the dashed lines in Fig. 8. Since the phase depends linearly on the frequency St, following the approach of Fournier et al. [24], the equivalent reflection coefficient $\mathcal{R}_m$ can therefore be replaced by a duct of length $\mathcal{L}_m$ terminated by a fully

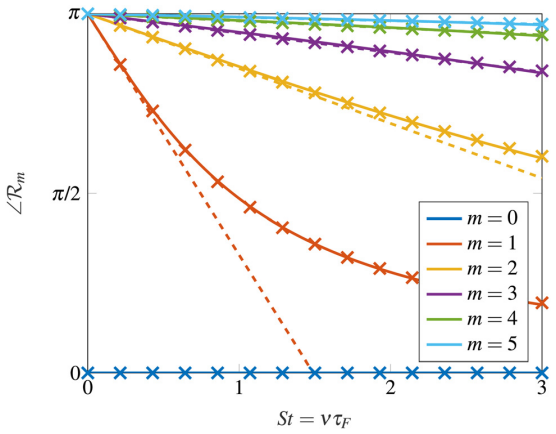

Fig. 8 For the considered generic can-annular configuration, the phase response of the gap obtained with FEM Helmholtz computations (full lines) is shown as a function of the dimensionless frequency St. The 1D model based on a characteristic length (crosses) shows perfect agreement with the reference. The phase response of the gap for the axial mode is trivially null. For all other azimuthal orders, starting from π, the phase monotonically decreases toward zero. For low frequencies St < 1, the phase response of the gap can be approximated by the tangent at the origin (dashed line). The higher the azimuthal order *m*, the wider the frequency range over which this approximation holds.

reflecting open end as shown in Fig. 9. This equivalent duct of length $\mathcal{L}_m$ induces an additional propagation time $\tau_m^* = \mathcal{L}_m/(c_d\tau_F)$ downstream of the cans that writes:

$$\mathcal{L}_m = \frac{L^*_{\text{char},m}H}{2L_g^*\sin^2\left(\frac{\pi m}{N}\right)}, \quad \tau_m^* = \frac{L^*_{\text{char},m}\tau_c^*}{2L_g^*\sin^2\left(\frac{\pi m}{N}\right)} \tag{18}$$

For a given geometry, the higher the azimuthal order, the shorter the equivalent duct. The full configuration is, therefore, reduced to a simple Rijke tube, whose downstream length varies with the azimuthal order m, representing the fact that the acoustic response of the gap is mode order dependent. In consequence, the methodology and analysis introduced in Secs. 2 and 3 can be used to understand the spectrum of the can-annular configurations. Note however that this does not apply to the axial mode, which is simply obtained by solving the single can combustor.

4.4 Clusters of Eigenmodes and Their Trajectories. Figures 10 and 11 show the spectrum of the can-annular combustor of Configurations A and B, respectively. Following the methodology introduced in Sec. 3, since the upstream condition is, in both cases, fixed, the trajectories when varying the downstream length are obtained. The circles indicate the eigenvalues computed with the reference FEM Helmholtz simulations, while the crosses are the results from the equivalent Rijke tube model described in Sec.

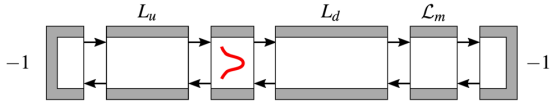

Fig. 9 Equivalent Rijke tube with fully reflecting boundaries. The equivalent length $\mathcal{L}_m$ varies with the azimuthal order of the mode considered and models the behavior of the acoustic communication through the gap. The larger the azimuthal order, the shorter $\mathcal{L}_m$.

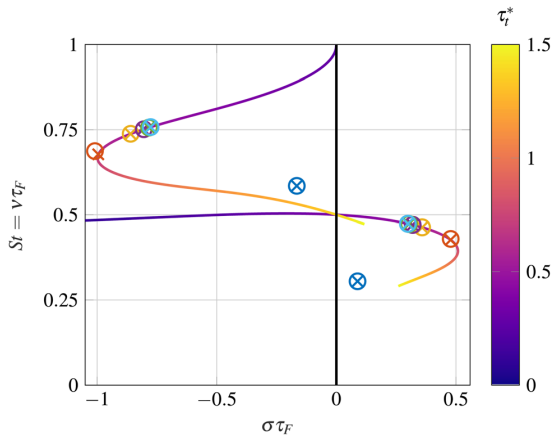

Fig. 10 Eigenvalues of the can-annular Configuration A as predicted by FEM Helmholtz simulations (circles) compared to the equivalent Rijke tube model (crosses). The latter shows excellent agreement with the reference. Colors indicate the azimuthal order as defined in Fig. 8. Except for the axial mode, all the eigenvalues are located on the trajectories obtained when varying τ_d^*. Their position on the trajectory depends on the mode order through the additional equivalent length $\mathcal{L}_m$. Note that modes $m = 4$ and $m = 5$ almost coincide. The ITA and acoustic clusters are distinct.

4.3. The latter shows excellent agreement with the reference. A small discrepancy is observed for the first azimuthal order $m = 1$. This is explained by the fact that the approximation of a linear phase response of the gap is valid only for low frequencies, as shown in Fig. 8, and the low azimuthal orders are the first to deviate from this approximation.

For Configuration A, $\tau_u^* = 0.251$ and the trajectories obtained resemble those shown in Fig. 4. For Configuration B, $\tau_u^* = 0.402$ and the trajectories are similar to Fig. 5. In particular, an

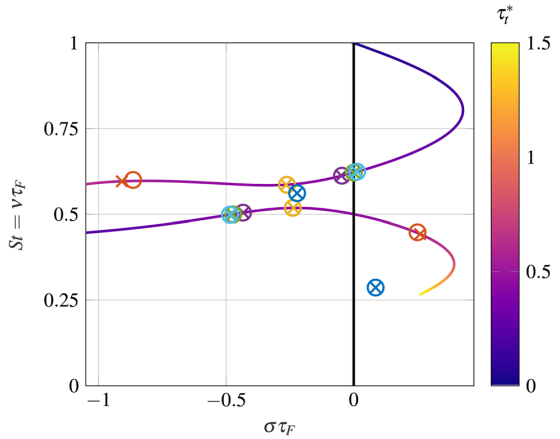

Fig. 11 Eigenvalues of the can-annular Configuration B as predicted by FEM Helmholtz simulations (circles) compared to the equivalent Rijke tube model (crosses). The latter shows excellent agreement with the reference. Colors indicate the azimuthal order as defined in Fig. 8. All azimuthal eigenmodes are located on the trajectories obtained when varying τ_d^* and their exact position on it depends on the mode order through the additional equivalent length $\mathcal{L}_m$. Note that modes $m = 4$ and $m = 5$ almost coincide. For this configuration, the presence of an XP makes the eigenmodes strongly veer.

exceptional point forces the trajectories to veer in order to avoid crossing. It is highlighted that, for both configurations, all the other eigenvalues are located on the trajectories (except for the special case of the axial mode $m=0$, which behaves differently from the rest of the cluster due to its different boundary conditions). Indeed, for all the azimuthal orders, the Rijke tube models are identical, in particular, they share the same flame response and upstream conditions. However, they differ by their total downstream propagation times, which is $\tau_t^* = \tau_d^* + \tau_m^*$, where τ_d^* is here a constant fixed by the can length L_d, whereas τ_m^*, due to the effective length $\mathcal{L}_m$ added to model the behavior of the gap, shows an explicit dependence on the azimuthal mode order. This fully explains the presence of all the eigenmodes on these trajectories. Their exact position is, however, determined by the total downstream propagation time τ_t^*. Following Eq. (18), low azimuthal order modes are associated to large values of τ_m^*, leading to a larger total downstream propagation time τ_t^* as observed in Figs. 10 and 11. In summary, the upstream conditions impose the eigenmodes to follow specific trajectories, while their exact position is fixed by the downstream conditions. This helps us to better understand the spectrum observed initially in Fig. 1. For Configuration A, the clusters are well separated, they do not interplay and can easily be identified. For Configuration B, the presence of an exceptional point plays a decisive role in shaping the trajectories (with a characteristic veer where the modes seem to repel each other), and, consequently, the spectrum of the considered system. Although the clusters seem entangled, we can now easily understand the trajectories the eigenmodes will follow when changing parameters.

This new insight could be exploited for early stage designs of new can-annular engines. Assuming that the design of the burners is fixed and that the flame response is known for a given amount of operating conditions, it may be possible to investigate the role of the upstream and downstream geometry on the thermoacoustic spectrum. The choice of the upstream can length L_u will impose the trajectories in the complex plane on which the eigenmodes are necessarily located. Finally, choosing the downstream length and the gap parameters will then govern their exact position on these trajectories. Note that changing the downstream parameters affects the system and the modes location in different ways. For example, changing the downstream length L_d induces a change in the total downstream length that is identical for all mode orders: all the modes are translated along the trajectories. Conversely, the impact of a modification in the geometry of the cross-talk area (width of the can or coupling strength) is different for each azimuthal order, since τ_m^* shows an explicit dependence to the mode order as shown in Eq. (18). Note also that changing the size of the gap or the width of the can have antagonist effects. Indeed, the larger the gap, ceteris paribus, the smaller the equivalent length, and the closer the eigenvalues along the trajectories. Modes of higher azimuthal order are closest within a cluster. Conversely, increasing the width of the can increases the effective length $\mathcal{L}_m$, leading to a wider spread of the clusters.

This could be used to develop strategies to stabilize an engine. Note that when we refer here to variations of L_u and L_d, we do not necessarily mean a drastic change of geometry, which is out of the question for later stages in the design. Instead, we refer to L_u and L_d as parameters indicating the effect of acoustic transport times upstream and downstream of the flame, which may be emulated by tuning the flow circuits belonging to the combustion chamber. For example, in the Configuration A shown in Fig. 10, the modes of azimuthal order $m = 1, 2, 3, 4$, and 5 on the lower branch are unstable. Changing the cross-talk area, by either changing the can width or gap size, will have a marginal effect on stabilizing the cluster: $\mathcal{L}_m$ is already very short for the highest azimuthal order and, no matter the cross-talk design, τ_t^* cannot be smaller than $\tau_t^* = \tau_d^* = 0.49$, which would still be unstable. However, reducing the downstream length of the can L_d would translate all eigenmodes along the trajectory (in the direction of smaller τ_t^*) and have a stabilizing effect on the entire cluster. Note, however, that a change in L_d will also have an impact on the axial modes $m=0$ and their trajectories should also be considered for a robust design. Similarly, for Configuration B, as shown in Fig. 11, the eigenmodes associated to the azimuthal order $m=1$ on the lower branch and $m=4$ and $m=5$ on the upper branch are unstable. Increasing the can length L_d would translate all the eigenvalues along the trajectories in the direction of higher τ_t^*, thus stabilizing the two unstable modes of the upper branch. However, it will further destabilize the azimuthal mode $m=1$ and will impact the stability of the axial modes $m=0$ as well. Conversely, reducing the coupling strength of the gap L_g^* would tend to increase τ_m^*, which would also have a stabilizing effect on the two unstable modes of the upper branch (τ_m^* small for high azimuthal order). Note, however, the axial modes $m=0$ would remain unaffected since the cross-talk area with the neighboring cans has no impact on them. The above analysis is an example of what the present work offers, which could be of help to develop new strategies for designing stable can-annular combustors during early stage studies. For a complete robust design, clusters of harmonics should also be considered as they may be the most unstable modes.

4.5 Modeling Assumptions and Limits of Validity. In this section, we want to put our results in perspective and briefly discuss the main modeling assumptions and the limits of validity of our models. In Sec. 4.3, we showed the possibility to replace the complex-valued reflection coefficient $\mathcal{R}_m$ by an effective duct length $\mathcal{L}_m$. The main advantage of this approach is to model a complex system—a cross-talk area in can-annular combustor—with a very simple element, i.e., a duct, which gives good insight and helps the fundamental understanding of the underlying physics. As shown in Fig. 8, for higher azimuthal order m, this modeling assumption is valid over a large frequency range, even for frequencies $\mathrm{St} > 3$. On the other hand, for lower azimuthal order, in particular for $m=1$, the range of validity is much narrower, up to $\mathrm{St} < 1$ in our case. However, since we assumed a purely reactive coupling, the error made only affects the phase response of the gap. Consequently, as shown in Figs. 10 and 11, the eigenmodes obtained with the equivalent Rijke tube models are indeed located on the trajectories, but their exact positions are mispredicted. In conclusion, for understanding or when considering only the clusters associated with the fundamental modes, the equivalent Rijke tube model can be used. However, when considering clusters of harmonics or to ensure quantitatively accurate results, the characteristic length model of Fournier et al. [35] should be preferred.

In Sec. 4.4, we showed that all the eigenmodes (except the special case $m=0$) necessarily lie on the same trajectory. This result comes from two main assumptions. First of all, the plenum was considered perfectly decoupled. However, if the plenum is taken into account and modeled as a thin annulus [24,60], it will also introduce an equivalent length $\mathcal{L}_m$ at the inlet that changes with the azimuthal order. Consequently, for each azimuthal order, the upstream condition will be different and each eigenmode will follow its own trajectory. The second reason is the fact that the cross-talk area, modeled with a characteristic length model, is purely reactive. For each azimuthal order, the gap introduces a different phase shift, but there is no amplification or damping. However, recent studies by Pedergnana and Noiray [38] and Orchini et al. [39] showed that, when accounting for mean flow effects, the effective coupling impedance exhibit resistive effects. In particular, as shown in Fig. 5 in [39], the magnitude of the equivalent reflection coefficient is mode order dependent, i.e., depending on the azimuthal order considered, the gap will introduce different amplification or damping. This effect causes the mode to follow distinct trajectories. Finally, and more generally, the 1D low-order modeling approach is inherently limited by two factors: the gap needs to be acoustically compact (or its finite extension modeled as in Ref. [36]) and only plane waves propagate in the cans, all other modes being cut-off. These two factors

were already discussed by Fournier et al. [35] and will also limit the number of clusters that can be properly captured with a 1D approach.

5 Summary and Conclusion

Starting from the observation that two similar can-annular configurations can lead to drastically different spectra, we investigated the interplay of acoustic and ITA clusters when they are in the same frequency range. To simplify the problem, we first considered a Rijke tube, which is one of the simplest thermoacoustic system and a fair approximation of can-annular combustors [24,33], and we derived an analytical low-order network model. Buckingham Π theorem allowed us to define dimensionless numbers so that the problem remains generally applicable to configuration of arbitrary parameters. We then investigated the interplay between the acoustic and ITA modes. In particular, for a given flame response, the impact on the eigenmodes of the downstream duct length and the flame position inside the system was analyzed.

For short upstream configurations, when increasing the downstream length, the frequency of the acoustic mode decreases whereas the ITA mode converges to a point identified as the eigenvalue of the semi-anechoic system. Conversely, for longer upstream configurations, the eigenmodes follow more peculiar trajectories and can, for example, switch nature, which confirmed previous observations [18,34,47]. In particular, the role of exceptional points in the complex plane was highlighted since it causes the eigenvalues to strongly veer, leading to characteristic trajectories.

We then considered two generic can-annular configurations. Using Bloch theory, we exploited the discrete rotational symmetry to reduce the study to a single unit-cell while preserving the dynamics of the full system. We confirmed the possibility to approximate the systems by a simple Rijke tube where the behavior of the gap was simply lumped into an additional effective length. Such modeling allowed us to explain the spectra of both systems. In particular, we showed that, in the absence of mean flow, the eigenmodes necessarily follow specific trajectories, imposed by the upstream conditions, and their exact position along the latter is determined by the gap and downstream parameters. We highlighted that, when ITA and acoustic clusters do not interplay, they are well distinct and identifiable, as exemplified in Configuration A (see Fig. 10). However, the presence of an exceptional point in the complex plane strongly influences the trajectories, as already reported by Silva et al. [44] and Mensah et al. [19]. ITA and acoustic clusters can also be entangled, as illustrated in Fig. 11 with Configuration B. New insight is gained when considering the trajectories the modes follow. In that sense, we confirmed the conclusion of Orchini et al. [21] who showed that the interaction between acoustic modes, ITA modes and exceptional points is essential to predict the stability in (can-)annular combustors.

The proposed framework may be of great utility for the design of can-annular combustors. This is exemplified by the two cases under investigation at the end of Sec. 4.4. The assumptions made by the proposed modeling strategy, as well as the limits of validity, are explicitly discussed in Sec. 4.5.

In this study, we considered a perfectly symmetric can-annular configuration. Symmetry breaking, due to, for example, geometrical imperfections, flow asymmetry, or nonlinear response of the flames, plays a major role in annular cavities because the degenerate pairs of azimuthal eigenmodes split into two distinct modes [61]. In can-annular configurations, it would double the number of modes in the acoustic and ITA clusters and could potentially affect their trajectories or lead to peculiar behaviors such as mode localization. This effect should be investigated in future studies.

Acknowledgment

This project has received funding from the European Union's Horizon 2020 research and innovation programme under Grant Agreement No 765998 *Annular Instabilities and Transient Phenomena in Gas Turbine Combustors* (ANNULIGhT) and from the Research Association for Combustion Engines (Forschungsvereinigung Verbrennungskraftmaschinen e.V. FVV, project number 6012700). The authors would also like to thank Max Meindl for valuable discussions and his help with FEM COMSOL MULTIPHYSICS simulations.

Funding Data

- European Commission (Grant No. 765998; Funder ID: 10.13039/501100000780).
- Forschungsvereinigung Verbrennungskraftmaschinen (Grant No. 6012700; Funder ID: 10.13039/501100003162).

Nomenclature

Roman

c_u, c_d = speed of sound upstream/downstream (m s^{-1})
$\mathcal{F}$ = flame transfer function
f, g = characteristic wave amplitudes (m s^{-1})
H = width of a can (m)
L_g = size of the gap (m)
$\mathcal{L}_m$ = equivalent length (m)
L_u, L_d = length of the upstream/downstream duct (m)
L_g^* = coupling strength, $L_g^* = L_g/H$
m = Bloch wave number
n = interaction index of the flame
N = number of cans
p' = acoustic pressure (Pa)
$\dot{q}'$ = normalized heat release fluctuations
R_i, R_o = reflection coefficient at the inlet/outlet
$\mathcal{R}_m$ = equivalent reflection coefficient
s = Laplace variable, $s = \sigma + i\omega$ (rad s^1)
s^* = dimensionless Laplace variable, $s^* = s\tau_F$
St = Strouhal number, St = $\nu\tau_F$
T_u, T_d = upstream/downstream temperature (K)
u' = acoustic velocity (m s^{-1})

Greek Symbols

θ = normalized temperature ratio, $\theta = T_d/T_u - 1$
ν = frequency (Hz)
ξ = ratio of specific impedances, $\xi = \bar{\rho}_u c_u/\bar{\rho}_d c_d$
$\bar{\rho}_u$, $\bar{\rho}_d$ = upstream/downstream mean density (kg m^{-3})
σ = growth rate (s^{-1})
τ_F = time delay of the flame (s)
τ_u, τ_d = upstream/downstream propagation time, $\tau_i = L_i/c_i$ (s)
τ_m^* = dimensionless equivalent propagation time
τ_t^* = total dimensionless propagation time, $\tau_t^* = \tau_d^* + \tau_m^*$
τ_u^*, τ_d^* = dimensionless upstream/downstream propagation time, $\tau_i^* = \tau_i/\tau_F$
ω = angular frequency, $\omega = 2\pi\nu$ (rad s^{-1})

Abbreviations

FTF = flame transfer function
XP = exceptional point

References

[1] Lieuwen, T., and McManus, K., 2003, "Combustion Dynamics in Lean-Premixed Prevaporized (LPP) Gas Turbines," J. Propul. Power, **19**(5), pp. 721–721.
[2] Poinsot, T., 2017, "Prediction and Control of Combustion Instabilities in Real Engines," Proc. Combust. Inst., **36**(1), pp. 1–28.
[3] Lieuwen, T., and Yang, V., eds., 2005, "Combustion Instabilities in Gas Turbine Engines: Operational Experience, Fundamental Mechanisms and Modeling," AIAA Paper No. v. 210.
[4] Culick, F., 1988, "Combustion Instabilities in Liquid-Fuelled Propulsion Systems - An Overview," *Combustion Instabilities in Liquid-Fuelled Propulsion Systems*, Vol. 450, Agard/NATO, Neuilly-sur-Seine, France.

[5] Lieuwen, T. C., 2012, *Unsteady Combustor Physics*, Cambridge University Press, New York.
[6] Hoeijmakers, M., Lopez Arteaga, I., Kornilov, V., Nijmeijer, H., and de Goey, P., 2013, "Experimental Investigation of Intrinsic Flame Stability," European Combustion Meeting, ECM2013, Scandinavian-Nordic Section of the Combustion Institute, Lund, Sweden, June 25–28.
[7] Hoeijmakers, M., Kornilov, V., Lopez Arteaga, I., de Goey, P., and Nijmeijer, H., 2014, "Intrinsic Instability of Flame-Acoustic Coupling," Combust. Flame, **161**(11), pp. 2860–2867.
[8] Silva, C. F., Emmert, T., Jaensch, S., and Polifke, W., 2015, "Numerical Study on Intrinsic Thermoacoustic Instability of a Laminar Premixed Flame," Combust. Flame, **162**(9), pp. 3370–3378.
[9] Courtine, E., Selle, L., and Poinsot, T., 2015, "DNS of Intrinsic Thermoacoustic Modes in Laminar Premixed Flames," Combust. Flame, **162**(11), pp. 4331–4341.
[10] Bomberg, S., Emmert, T., and Polifke, W., 2015, "Thermal Versus Acoustic Response of Velocity Sensitive Premixed Flames," Proc. Combust. Inst., **35**(3), pp. 3185–3192.
[11] Emmert, T., Bomberg, S., and Polifke, W., 2015, "Intrinsic Thermoacoustic Instability of Premixed Flames," Combust. Flame, **162**(1), pp. 75–85.
[12] Emmert, T., Bomberg, S., Jaensch, S., and Polifke, W., 2017, "Acoustic and Intrinsic Thermoacoustic Modes of a Premixed Combustor," Proc. Combust. Inst., **36**(3), pp. 3835–3842.
[13] Yong, K. J., Silva, C. F., and Polifke, W., 2021, "A Categorization of Marginally Stable Thermoacoustic Modes Based on Phasor Diagrams," Combust. Flame, **228**, pp. 236–249.
[14] Dowling, A. P., and Stow, S. R., 2003, "Acoustic Analysis of Gas Turbine Combustors," J. Propul. Power, **19**(5), pp. 751–764.
[15] Eckstein, J., and Sattelmayer, T., 2006, "Low-Order Modeling of Low-Frequency Combustion Instabilities in Aeroengines," J. Propul. Power, **22**(2), pp. 425–432.
[16] Ghani, A., Steinbacher, T., Albayrak, A., and Polifke, W., 2019, "Intrinsic Thermoacoustic Feedback Loop in Turbulent Spray Flames," Combust. Flame, **205**(7), pp. 22–32.
[17] Albayrak, A., Steinbacher, T., Komarek, T., and Polifke, W., 2018, "Convective Scaling of Intrinsic Thermo-Acoustic Eigenfrequencies of a Premixed Swirl Combustor," ASME J. Eng. Gas Turbines Power, **140**(4), p. 041510.
[18] Hosseini, N., Kornilov, V., Lopez Arteaga, I., Polifke, W., Teerling, O., and de Goey, L., 2018, "Intrinsic Thermoacoustic Modes and Their Interplay With Acoustic Modes in a Rijke Burner," Int. J. Spray Combust. Dyn., **10**(4), pp. 315–325.
[19] Mensah, G. A., Magri, L., Silva, C. F., Buschmann, P. E., and Moeck, J. P., 2018, "Exceptional Points in the Thermoacoustic Spectrum," J. Sound Vib., **433**, pp. 124–128.
[20] Silva, C., Yong, K. J., and Magri, L., 2019, "Thermoacoustic Modes of Quasi-One-Dimensional Combustors in the Region of Marginal Stability," ASME J. Eng. Gas Turbines Power, **141**(2), p. 021022.
[21] Orchini, A., Silva, C. F., Mensah, G. A., and Moeck, J. P., 2020, "Thermoacoustic Modes of Intrinsic and Acoustic Origin and Their Interplay With Exceptional Points," Combust. Flame, **211**, pp. 83–95.
[22] Buschmann, P. E., Mensah, G. A., Nicoud, F., and Moeck, J. P., 2020, "Solution of Thermoacoustic Eigenvalue Problems With a Noniterative Method," ASME J. Eng. Gas Turbines Power, **142**(3), p. 031022.
[23] Buschmann, P. E., Mensah, G. A., and Moeck, J. P., 2020, "Intrinsic Thermoacoustic Modes in an Annular Combustion Chamber," Combust. Flame, **214**, pp. 251–262.
[24] Fournier, G. J. J., Haeringer, M., Silva, C. F., and Polifke, W., 2021, "Low-Order Modeling to Investigate Clusters of Intrinsic Thermoacoustic Modes in Annular Combustors," ASME J. Eng. Gas Turbines Power, **143**(4), p. 041025.
[25] Bethke, S., Krebs, W., Flohr, P., and Prade, B., 2002, "Thermoacoustic Properties of Can Annular Combustors," AIAA Paper No. 2002-2570.
[26] Kaufmann, P., Krebs, W., Valdes, R., and Wever, U., 2008, "3D Thermoacoustic Properties of Single Can and Multi Can Combustor Configurations," ASME Paper No. GT2008-50755.
[27] Panek, L., Farisco, F., and Huth, M., 2017, "Thermo-Acoustic Characterization of Can-Can Interaction of a Can-Annular Combustion System Based on Unsteady CFD LES Simulation," Proceedings of First Global Power and Propulsion Forum, GPPS, Zurich, Switzerland, Jan. 16–18, Paper No. GPPF-2017-81.
[28] Farisco, F., Panek, L., and Kok, J. B., 2017, "Thermo-Acoustic Cross-Talk Between Cans in a Can-Annular Combustor," Int. J. Spray Combust. Dyn., **9**(4), pp. 452–469.
[29] Ghirardo, G., Di Giovine, C., Moeck, J. P., and Bothien, M. R., 2019, "Thermoacoustics of Can-Annular Combustors," ASME J. Eng. Gas Turbines Power, **141**(1), p. 011007.
[30] Jegal, H., Moon, K., Gu, J., Li, L. K., and Kim, K. T., 2019, "Mutual Synchronization of Two Lean-Premixed Gas Turbine Combustors: Phase Locking and Amplitude Death," Combust. Flame, **206**, pp. 424–437.
[31] Moon, K., Jegal, H., Gu, J., and Kim, K. T., 2019, "Combustion-Acoustic Interactions Through Cross-Talk Area Between Adjacent Model Gas Turbine Combustors," Combust. Flame, **202**, pp. 405–416.
[32] Moon, K., Jegal, H., Yoon, C., and Kim, K. T., 2020, "Cross-Talk-Interaction-Induced Combustion Instabilities in a Can-Annular Lean-Premixed Combustor Configuration," Combust. Flame, **220**, pp. 178–188.
[33] Haeringer, M., Fournier, G. J. J., Meindl, M., and Polifke, W., 2021, "A Strategy to Tune Acoustic Terminations of Single-Can Test-Rigs to Mimic Thermoacoustic Behavior of a Full Engine," ASME J. Eng. Gas Turbines Power, **143**(7), p. 071029.
[34] von Saldern, J., Orchini, A., and Moeck, J., 2021, "Analysis of Thermoacoustic Modes in Can-Annular Combustors Using Effective Bloch-Type Boundary Conditions," ASME J. Eng. Gas Turbines Power, **143**(7), p. 071019.
[35] Fournier, G. J. J., Meindl, M., Silva, C. F., Ghirardo, G., Bothien, M. R., and Polifke, W., 2021, "Low-Order Modeling of Can-Annular Combustors," ASME J. Eng. Gas Turbines Power, **143**(12), p. 121004.
[36] von Saldern, J. G. R., Orchini, A., and Moeck, J. P., 2021, "A Non-Compact Effective Impedance Model for Can-to-Can Acoustic Communication: Analysis and Optimization of Damping Mechanisms," ASME J. Eng. Gas Turbines Power, **143**(12), p. 121024.
[37] Orchini, A., 2022, "An Effective Impedance for Modelling the Aeroacoustic Coupling of Ducts Connected Via Apertures," J. Sound Vib., **520**, p. 116622.
[38] Pedergnana, T., and Noiray, N., 2022, "Coupling-Induced Instability in a Ring of Thermoacoustic Oscillators," Proc. R. Soc. A Math., Phys. Eng. Sci., **478**(2259), p. 20210851.
[39] Orchini, A., Pedergnana, T., Buschmann, P. E., Moeck, J. P., and Noiray, N., 2022, "Reduced-Order Modelling of Thermoacoustic Instabilities in Can-Annular Combustors," J. Sound Vib., **526**, p. 116808.
[40] Tay-Wo-Chong, L., Bomberg, S., Ulhaq, A., Komarek, T., and Polifke, W., 2012, "Comparative Validation Study on Identification of Premixed Flame Transfer Function," ASME J. Eng. Gas Turbines Power, **134**(2), p. 021502.
[41] Chu, B.-T., 1953, "On the Generation of Pressure Waves at a Plane Flame Front," Symp. (Int.) Combust., **4**(1), pp. 603–612.
[42] Crocco, L., 1951, "Aspects of Combustion Stability in Liquid Propellant Rocket Motors Part1: Fundamentals. Low Frequency Instability With Monopropellants," J. Am. Rocket Soc., **21**(6), pp. 163–178.
[43] Barenblatt, G. I., 2003, *Scaling. Cambridge Texts in Applied Mathematics*, Cambridge University Press, Cambridge, UK.
[44] Silva, C. F., and Polifke, W., 2019, "Non-Dimensional Groups for Similarity Analysis of Thermoacoustic Instabilities," Proc. Combust. Inst., **37**(4), pp. 5289–5297.
[45] Emmert, T., Meindl, M., Jaensch, S., and Polifke, W., 2016, "Linear State Space Interconnect Modeling of Acoustic Systems," Acta Acust. United Acust., **102**(5), pp. 824–833.
[46] Mensah, G. A., 2019, "Efficient Computation of Thermoacoustic Modes," Ph.D. thesis, TU Berlin, Fak. V, Verkehrs- und Maschinensysteme, Berlin, Germany.
[47] Sogaro, F. M., Schmid, P. J., and Morgans, A. S., 2019, "Thermoacoustic Interplay Between Intrinsic Thermoacoustic and Acoustic Modes: Non-Normality and High Sensitivities," J. Fluid Mech., **878**, pp. 190–220.
[48] Polifke, W., 2020, "Modeling and Analysis of premixed flame Dynamics by Means of Distributed Time Delays," Prog. Energy Combust. Sci., **79**, p. 100845.
[49] Æsøy, E., Nygård, H. T., Worth, N. A., and Dawson, J. R., 2022, "Tailoring the Gain and Phase of the Flame Transfer Function Through Targeted Convective-Acoustic Interference," Combust. Flame, **236**, p. 111813.
[50] Yong, K. J., Silva, C. F., Fournier, G. J. J., and Polifke, W., 2021, "Categorization of Thermoacoustic Modes in an Ideal Resonator With Phasor Diagrams," Combust. Flame, epub.
[51] Mukherjee, N. K., and Shrira, V., 2017, "Intrinsic Flame Instabilities in Combustors: Analytic Description of a 1-D Resonator Model," Combust. Flame, **185**, pp. 188–209.
[52] Schaefer, F., Guo, S., and Polifke, W., 2021, "The Impact of Exceptional Points on the Reliability of Thermoacoustic Stability Analysis," ASME J. Eng. Gas Turbines Power, **143**(2), p. 021010.
[53] Sogaro, F., Schmid, P., and Morgans, A. S., 2017, "Sensitivity Analysis of Thermoacoustic Instabilities," 24th International Congress on Sound and Vibration (ICSV 24), IIAV, London, UK, July 23–27.
[54] Marble, F. E., and Candel, S. M., 1977, "Acoustic Disturbance From Gas Non-Uniformities Convected Through a Nozzle," J. Sound Vib., **55**(2), pp. 225–243.
[55] Bauerheim, M., Duran, I., Livebardon, T., Wang, G., Moreau, S., and Poinsot, T., 2016, "Transmission and Reflection of Acoustic and Entropy Waves Through a Stator–Rotor Stage," J. Sound Vib., **374**, pp. 260–278.
[56] Morgans, A. S., and Duran, I., 2016, "Entropy Noise: A Review of Theory, Progress and Challenges," Int. J. Spray Combust. Dyn., **8**(4), pp. 285–298.
[57] Bloch, F., 1929, "Über Die Quantenmechanik Der Elektronen in Kristallgittern," Z. Phys., **52**(7–8), pp. 555–600.
[58] Mensah, G. A., Campa, G., and Moeck, J. P., 2016, "Efficient Computation of Thermoacoustic Modes in Industrial Annular Combustion Chambers Based on Bloch-Wave Theory," ASME J. Eng. Gas Turbines Power, **138**(8), p. 081502.
[59] Ghirardo, G., Moeck, J. P., and Bothien, M. R., 2020, "Effect of Noise and Nonlinearities on Thermoacoustics of Can-Annular Combustors," ASME J. Eng. Gas Turbines Power, **142**(4), p. 041005.
[60] Bauerheim, M., Parmentier, J.-F., Salas, P., Nicoud, F., and Poinsot, T., 2014, "An Analytical Model for Azimuthal Thermoacoustic Modes in an Annular Chamber Fed by an Annular Plenum," Combust. Flame, **161**(5), pp. 1374–1389.
[61] Bauerheim, M., Salas, P., Nicoud, F., and Poinsot, T., 2014, "Symmetry Breaking of Azimuthal Thermo-Acoustic Modes in Annular Cavities: A Theoretical Study," J. Fluid Mech., **760**, pp. 431–465.